

**Investigations of the Local
Hydration Structure of
Alkanethiol Self-Assembled
Monolayers by FM-AFM**

Akito Fujita

2019

Contents

1	Introduction	1
1.1	Background	1
1.2	Purpose of Thesis	3
1.3	Structure of Thesis	4
2	Solid-Liquid Interface Studies by AFM Measurements	7
2.1	Solid-Liquid Interface	7
2.1.1	Electrical Double Layer	7
2.1.2	Hydration Structures	10
2.2	Operation Principle of AFM	12
2.2.1	Contact Mode AFM	12
2.2.2	Oscillation Properties of a Cantilever	13
2.2.3	Outline of the Amplitude-Modulation AFM	14
2.2.4	Operation Principle of Frequency-Modulation AFM	16
2.2.4.1	Relationship Between the Force Gradient and Frequency Shift	18
2.2.4.2	Conversion of Experimental Frequency Shift Curves to Force Curves	18
2.3	Forces Acting on the Tip in Liquid Conditions	19
2.3.1	Pauli Repulsion and van der Waals Forces	22
2.3.2	EDL Forces	23
2.3.3	Hydration Forces (Solvation Forces)	24
2.4	Scanning Modes of AFM Measurements	25
2.5	Summary	27

CONTENTS

3	Hydration Structures of Hydrophilic and Hydrophobic SAMs	28
3.1	Introduction	28
3.2	Alkanethiol Self-Assembled Monolayers	30
3.3	Experimental	31
3.3.1	Materials	31
3.3.2	Fabrication of an Atomically Flat Au(111) Plane	32
3.3.3	Fabrication of Alkanethiol SAMs	32
3.4	Topography of the Au(111) plane	33
3.5	Influence of the Functional Group on Alkanethiol SAMs	33
3.5.1	Wide View Topographic Images of Alkanethiol SAMs	33
3.5.2	Influence of the Functional Group on the Molecular Structure	35
3.5.3	Hydration Structure Measurements	38
3.5.4	Effect of Hydrocarbon Contamination on Hydrophobic Surfaces	42
3.6	Measurements of Binary Phase Separated SAMs	46
3.6.1	Single Phased SAMs	46
3.6.2	Binary Phased Separated SAMs	49
3.6.3	Effect of Contamination on the Hydration Structure of Phase Separated SAMs	52
3.7	Summary	54
4	Hydration Structure Measurements on Different Surface Molecular Arrangements of Hydroxy Terminated SAMs	55
4.1	Introduction	55
4.2	Molecular Structures of the Alkanethiol SAM	57
4.2.1	Origin of the different structures in alkanethiol SAMs	58
4.3	Sample Preparation and Experimental Procedures	59
4.4	Topography of the C11OH SAM	61
4.4.1	Molecular Structure of C11OH SAMs	61
4.4.2	Influence of Temperature on C11OH SAMs	61
4.4.2.1	Fluctuation of the Molecular Structure in the C6OH SAM	63
4.5	Hydration Structure of the alkanethiol SAM	65

4.5.1	Frequency Shift Maps of the C11OH SAM	65
4.5.2	Details of Calculating the Local Water Molecule Distribution from Force Versus Distance Curves	69
4.5.3	Benefits of the Local Water Molecule Distribution Calculation	74
4.6	Hydration Structure Measurements at the Vicinity of an Etch Pit on C16OH SAMs	75
4.7	Summary	79
5	Development of Electrochemical AFM Applied to Hydration Structure Measurements	80
5.1	Introduction	80
5.2	Instrumentation of the EC-AFM	81
5.2.1	Sample Holder	83
5.2.2	Cantilever Holder	86
5.2.3	Operation Procedure of the EC-AFM	87
5.3	Operation Tests of the EC-AFM	88
5.3.1	AFM Imaging	88
5.3.2	Cyclic Voltammetry	88
5.4	Hydration Structure Measurements Applying the Developed EC-AFM	91
5.4.1	Physical Property of Graphene	91
5.4.2	Force Mapping Measurements on HOPG	91
5.5	Summary	98
6	Conclusions and Future Work	100
6.1	Conclusions	100
6.2	Future Work	102
A	Synthesis of Gold Nanoparticles by a Vacuum Evaporation Method	103
A.1	Introduction	103
A.2	Experimental	105
A.3	Results and Discussion	107
A.4	Summary	122

CONTENTS

References	123
------------	-----

1

Introduction

1.1 Background

The idea of nanotechnology was first proposed from Richard Feynman at a famous lecture called *"There's Plenty of Room at the Bottom"* in the annual meeting of the American Physical Society in 1959.¹⁾ He emphasized the advantages of downsizing where he gave an example of recording all of the volumes of the encyclopedia on a single pinhead. Downsizing is equivalent to densification and is still the major approach in today's nanotechnology. The most famous example can be found in the semiconductor industry; engineers and scientists have worked hard to satisfy Moore's law, which is a prediction that the number of transistors on an LSI integrated circuit will be doubled in every 18 months.²⁾ Densification or downsizing is cost effective and in most cases enhances the performance of each single device. Therefore, downsizing the whole system has been the main goal of nanotechnology for a long time.

When the size length becomes under a hundred nanometers, downsizing does not just enhance the performance of devices or materials. In these size scales, quantum mechanical effects become evident and the physical properties of the materials or devices derive from their mesoscopic length properties. This is a problem in the semiconductor industry and now intensive work is performed to circumvent problems such as tunneling and short-channel effects.³⁾ On the other hand, the appearance of quantum mechanical effects is also a chance to utilize materials into new applications. A good example are gold nanoparticles where

1. INTRODUCTION

new physical properties appear when they are under 100 nm such as surface plasmon resonance (SPR),⁴⁾ catalytic effects⁵⁾ and even magnetism.⁶⁾ The physical properties completely differ from their bulk states and the measurement of nanomaterials is a crucial issue.

Although there are numerous methods to characterize the physical or chemical properties of the material, the most fundamental measurement is to observe the material itself. Since the interest is on nanomaterials within the size of several nanometers, the ability to image in atomic-resolution is essential. So far, this has been achieved mainly by transmission electron microscope (TEM)^{7,8)} and by scanning probe microscopes (SPMs).⁹⁻¹²⁾ SPMs are a surface sensitive method and can even achieve atomic-resolution images of the surface, which is impossible in TEM.

The history of SPM starts with the invention of the scanning tunneling microscope (STM) by Binnig in 1981.¹³⁾ The STM measures the tunneling current between the metallic tip and the surface, and controls the tip-sample distance to be constant to measure the topographic image of the surface. Numerous atomic-resolution images have been reported from STM and is now a powerful tool to characterize samples.¹⁴⁾ However, STM has some disadvantages. The biggest problem is that it can't measure insulating samples due to the operation mechanism. This problem was also solved by Binnig in 1986, where he invented the atomic force microscope (AFM). The AFM measures the interaction force acting between the tip and sample and in principle, there are no limitations to the application of AFM. Many techniques have derived from the AFM, making them capable of measuring physical properties simultaneously as the topography is measured. Some examples are kelvin probe force microscope,¹⁵⁾ magnetic force microscope,¹⁶⁾ scanning impedance microscope¹⁷⁾ and many more.

A huge advantage of SPM is that it's a surface sensitive technique and is capable of achieving atomic-resolution images of the surface in real space. Other surface sensitive techniques mostly depend on the diffraction phenomenon, such as X-ray and electron diffraction (ED)^{18,19)} and hence, the information obtained are in reciprocal lattice space. Examining the surface with complex structures is sometimes puzzling when diffraction measurements are only available. A rep-

representative example of this is the puzzling Si(111)-(7×7) structure which was solved by real space imaging with the STM by Binnig in 1983.²⁰⁾

In the last decade, frequency-modulation AFM (FM-AFM) has been proved to be capable of atomic/molecular-scale imaging in liquid conditions.^{21,22)} Recently, a technique which visualizes the two-dimensional (2D) and three-dimensional (3D) local hydration structures with a sub-nanometer scale resolution was developed based on the force mapping technique by FM-AFM.^{23,24)} The interface structure of the solid-liquid interface plays a crucial role in many applications which contain solution such as batteries,^{25,26)} catalysis²⁷⁾ and biosensors.²⁸⁾ When water is the liquid medium, it's widely known that the water molecule density oscillates with a period of about 0.3 nm, which matches with the size of a single water molecule. This structure is called an hydration structure and is now known to effect numerous phenomena, such as the chemical reaction at an electrode,²⁹⁾ the stabilization and functional expression of biomolecules^{30,31)} and the growth process of crystals and nanoparticles.^{32,33)} Many measurement methods have been applied to measure the hydration structure so far, such as X-ray/neutron reflectivity,³⁴⁻³⁶⁾ sum frequency generation (SFG),³⁷⁻⁴⁰⁾ and surface force apparatus (SFA).^{41,42)} These techniques measure the water molecule density or force in the direction perpendicular to the surface, and lack information about the in-plane local water molecule distribution. On the other hand, the force mapping technique can measure the in-plane hydration structure in addition to the out-of-plane hydration structures on any surface areas of concern. The hydration structures measured with the force mapping technique have been reported for a wide variety of samples, such as minerals,^{24,43-45)} alkali halides,⁴⁶⁾ lipid membranes^{47,48)} and biomolecules.^{49,50)} From these studies, it is now understood that the in-plane water molecule distribution aren't homogeneous and water molecules are localized at the surface.

1.2 Purpose of Thesis

Although the force mapping technique has proved the existence of the in-plane hydration structure, it's hard to discover the factors that these structures depend on. Numerous factors are suspected to influence the in-plane hydration

1. INTRODUCTION

structure, such as the hydrophilicity/hydrophobicity of the surface, topography, surface charge, etc. Most of these factors vary between two different samples, and it is usually impossible to deduce the factors that alter the hydration structures between two samples. To circumvent this problem, the alkanethiol self-assembled monolayer (SAM) was chosen as the model system. Forming alkanethiol SAMs on a substrate is a famous method to modify the surface and is possible to change the surface property or structure. This is an ideal sample as a model system, since it's possible to alter only one factor between two samples and emphasize the impact of the factor on the hydration structure.

In this thesis, the hydration structure of alkanethiol SAMs were measured with an FM-AFM based on the 2D force mapping technique. The influence of hydrophilicity/hydrophobicity and atomic corrugation of the sample were investigated by changing the terminal functional group and surface structure of the alkanethiol SAM. Also, an electrochemical AFM (EC-AFM) was developed and combined with the force mapping technique to measure the influence of surface potential on the in-plane hydration structure. The ultimate goal of this thesis is to deduce the factors that alter the in-plane hydration structure and demonstrate that FM-AFM is a powerful tool to investigate the local structure at the solid-liquid interface.

1.3 Structure of Thesis

This thesis is composed of 6 chapters. Fig. 1.1 illustrates the structure of this thesis.

In chapter 1, the background and purpose of this thesis was described. The history of the development of nanotechnology, SPM and an overview about the solid-liquid interface was summarized.

In chapter 2, a review of the solid-liquid interface and AFM measurements were presented.

In chapter 3, the influence of hydrophobicity to the hydration structure was investigated by comparing the hydration structures of hydrophilic and hydrophobic alkanethiol SAMs. Throughout the investigation, it was found that hydrophobic SAMs showed peculiar frequency shift versus distance curves and the possibility

of hydrocarbon contamination gathering to the vicinity of the hydrophobic SAM was discussed. Also, the tip effect was neglected by measuring the hydration structure over a binary phase separated SAM which was composed of hydrophilic and hydrophobic alkanethiol molecules.

In chapter 4, the hydration structure of SAMs with different molecular arrangements were compared to understand the impact of atomic-corrugation on the local hydration structure. Two molecular structures, namely, the $(\sqrt{3} \times \sqrt{3})R30^\circ$ structure and the $c(4 \times 2)$ superlattice structure are known to form on alkanethiol SAMs which have a height difference under 50 pm. The hydration structure of the $(\sqrt{3} \times \sqrt{3})R30^\circ$ structure and the $c(4 \times 2)$ superlattice structure were measured and the influence of atomic corrugation was investigated. Also, the experimentally obtained frequency shift versus distance curves were converted to water molecule distributions, which matched with results achieved from molecular dynamic (MD) simulations.

In chapter 5, a EC-AFM cell was developed and applied to hydration structure measurements. An EC setup was introduced to the AFM by insetting electrodes to the EC cell, which was achieved by redesigning the cantilever holder and sample holder. The operation of the apparatus was confirmed by imaging mica substrates in atomic resolution and by measuring the cyclic voltammetry of potassium ferrocyanide. Finally, the influence of surface potential on the hydration structure of highly oriented pyrolytic graphene (HOPG) was investigated.

In chapter 6, the thesis is summarized and the conclusion is presented. Some proposals for future work are also presented.

1. INTRODUCTION

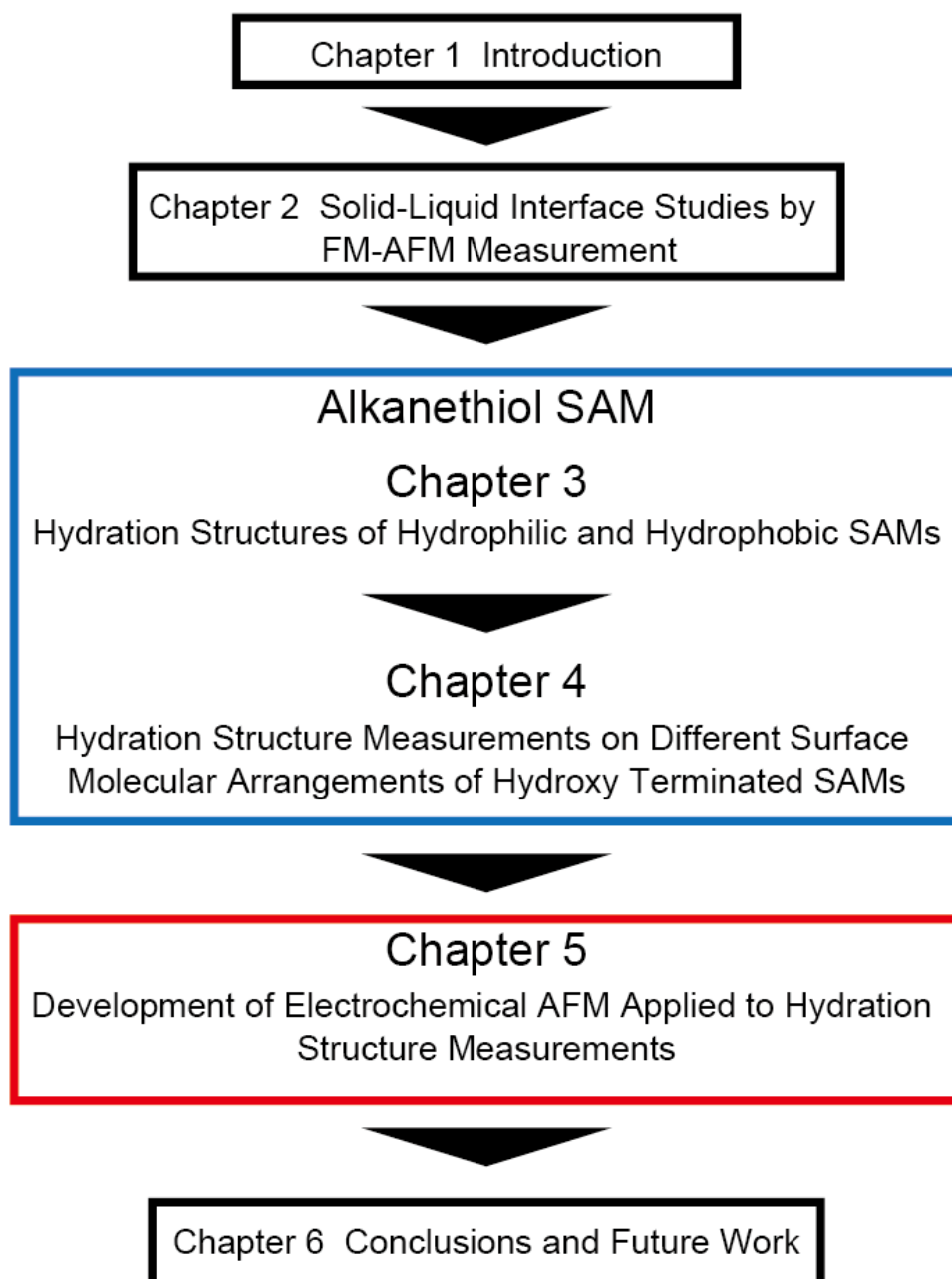


Figure 1.1: Schematic illustration of the structure of this thesis.

2

Solid-Liquid Interface Studies by AFM Measurements

2.1 Solid-Liquid Interface

2.1.1 Electrical Double Layer

In most cases, a solid surface gets charged when it's immersed into solution. This is due to the protonation or deprotonation of functional groups on the surface, adsorption of ions from the solution or charge transfer between other surfaces.⁵¹⁾ The ions with the opposite charge, which are called counterions, gather to the vicinity of the surface and shield the surface charge and form an EDL. Fig. 2.1 shows a schematic illustration of the EDL formed at solid-liquid interfaces. Although several models have been proposed, the most popular structure of the EDL is called the Guoy-Chapman-Stern (GCS) model. This model assumes that the EDL is composed from the Stern layer and the diffusion layer. The counterions that construct the Stern layer (also called the Helmholtz layer) are strongly adsorbed to the surface while the counterions in the diffusion layer follow a Boltzmann distribution. Take notice that rigorously, the Stern layer is defined between the solid surface and the center of the adsorbing ions, and no ions exist "inside" the Stern layer. The Stern layer can be regarded as a flat plane capacitor and the potential linearly decreases inside the Stern layer.

2. SOLID-LIQUID INTERFACE STUDIES BY AFM MEASUREMENTS

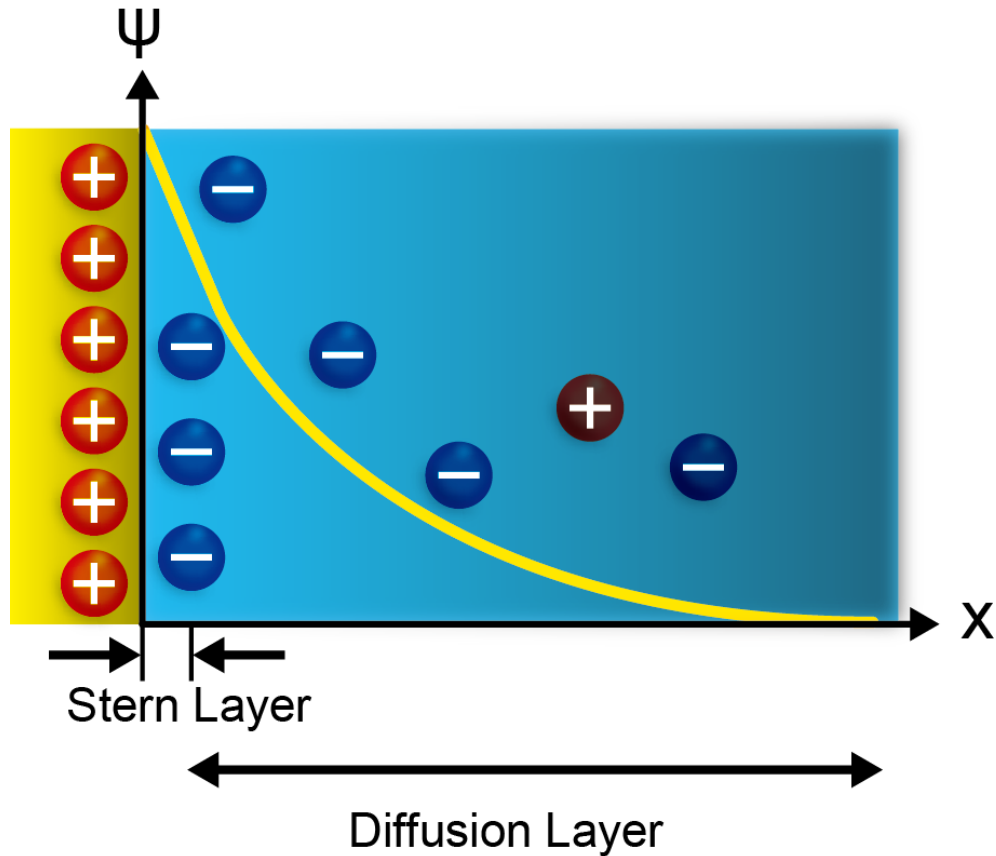


Figure 2.1: Schematic illustration of the GCS model of the EDL formed at the solid-liquid interface. The EDL is composed by the Stern layer and the diffusion layer.

To start with, the relationship between the counterions and the potential of the solution in the diffusion layer of the EDL will be discussed. Assume that two electrodes with the same negative surface potential are inserted in a solution containing 1:1 electrolytes. The electrodes are separated with a distance D . The center position between the two electrodes is defined $x = 0$ and the positions of the two electrodes are defined $x = \pm D/2$. For simplicity, the argument will be conducted in one dimension. At point x , the counterions are assumed to follow the Boltzmann distribution

$$\rho(x) = \rho_0 \exp\left(-\frac{ze\psi(x)}{\varepsilon_0\varepsilon}\right) \quad (2.1)$$

2.1 Solid-Liquid Interface

where $\rho(x)$ is the number density of the counterions at position x , z is the valence of the counterion, e is the elementary charge, $\psi(x)$ is the potential at position x , ϵ_0 and ϵ are the dielectric constant of vacuum and the solution, respectively. Assume that the two electrodes are separated enough so that $\rho(0) = \rho_0$ and ρ_0 is equal to the number density in bulk conditions. The surface charge due to the potential is equal to the sum of the charge of the counterions and the system can be stated by the Poisson equation.

$$\frac{d^2\psi(x)}{dx^2} = -\frac{ze\rho(x)}{\epsilon_0\epsilon} \quad (2.2)$$

Hence, when the two equations are combined, the famous Poisson-Boltzmann (PB) equation is obtained.

$$\frac{d^2\psi(x)}{dx^2} = -\frac{ze\rho_0}{\epsilon_0\epsilon} \exp\left(-\frac{ze\psi(x)}{k_B T}\right) \quad (2.3)$$

where k_B is the Boltzmann constant and T is the temperature of the system. This is the fundamental equation when the EDL is analyzed and gives the potential $\psi(x)$, electric field $E = -d\psi(x)/dx$ and number density of the counterions $\rho(x)$ when the equation is solved. Assuming charge neutrality between the surface charge of the electrode and the net charge of the counterions constructing the EDL, the Grahame equation can be deduced which connects the charge density σ_0 and surface potential ψ_0 .

$$\sigma_0 = \sqrt{\epsilon_0\epsilon k_B T \rho_0} \sinh\left(\frac{e\psi_0}{2k_B T}\right) \quad (2.4)$$

A famous solution was presented by Derjaguin, Landau, Verwey and Overbeek, and their theory is called the DLVO theory. According to the DLVO theory, when the EDL of two flat surfaces with an equal surface potential overlap, it causes a repulsive force and can be expressed by the following form.

$$F(r) = \frac{32\epsilon_0\epsilon(k_B T \kappa)^2}{e^2} \tanh^2\left(\frac{ze\psi_0}{4k_B T}\right) \exp(-\kappa x) \quad (2.5)$$

Where ψ_0 is the surface potential. κ can be expressed by the following formula.

$$\kappa = \sqrt{\frac{\rho_\infty e^2 z^2}{\epsilon_0\epsilon k_B T}} \quad (2.6)$$

2. SOLID-LIQUID INTERFACE STUDIES BY AFM MEASUREMENTS

Where ρ_∞ is the concentration of the electrolyte in bulk conditions. Since the attenuation length of eq. 2.5 is $1/\kappa$, $1/\kappa$ is called the Debye length and characterizes the length of the EDL. The DLVO theory gives a solution to the PB equation, but eq. 2.5 can only be applied when the surface potential of the two objects are the same. This is not the case in most AFM experiments and the solution will be shown in section 2.3.2.

2.1.2 Hydration Structures

Although numerous studies have been explained by the DLVO theory, it's not complete in every condition. Experimentally measured force versus distance curves (from now mentioned as only force curves) deviate from the DLVO theory in short ranges such as several nanometers. This deviation was considered to be due to non-DLVO forces and one of the most popular interaction is the hydration force.

Hydration forces derive from the overlap of hydration structures. Fig. 2.2 illustrates the formation mechanism of the hydration structure at the solid-liquid interface. Hydration structures are a specific structure of water molecules formed on the solid-liquid interface and are due to intermolecular repulsion forces. To explain the formation mechanism of hydration structures, think about a solid surface which is introduced into water. The diameter of the water molecules is R . In this case, the water molecules in the vicinity of the surface are restricted at the interface. When the solid surface is rigid, the repulsion force from the solid surface increase and the water molecules at the vicinity of the solid are more restrained. This causes a peak in the water molecule distribution at a distance $R/2$ from the surface and forms the first hydration layer. The center of the second layer of water molecules have to be R away from the surface due to hard-ball repulsion of the water molecules. Therefore, a valley in the water molecule distribution occurs at a distance R from the surface and a peak at a distance $3R/2$. The peak at the second hydration layer decreases since the second hydration layer is next to the first hydration layer, which is less rigid than the solid surface. This continues layer by layer and hence, causes a oscillation in the water molecule distribution.

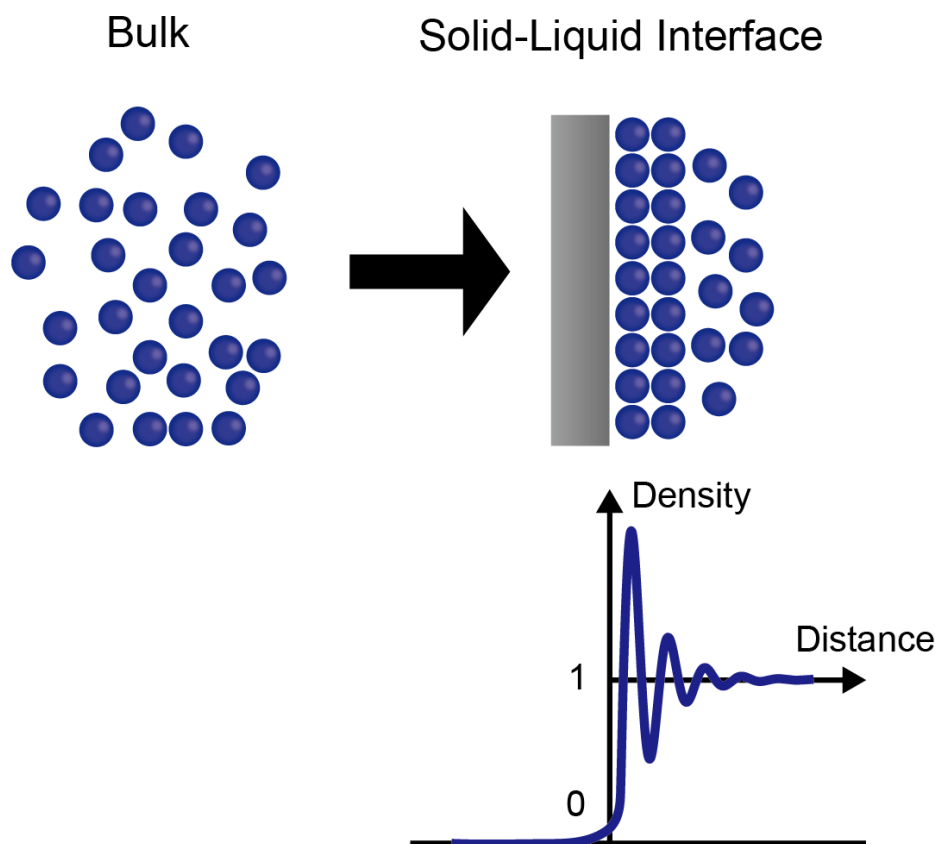


Figure 2.2: Schematic illustration of the formation mechanism of an hydration structure at the solid-liquid interface.

The structures of the water molecules are different from their structure in a bulk state, and are also different from ice.

The mechanism introduced above explains why the water molecule density oscillates in the direction normal to the surface. This has been confirmed by X-ray/neutron reflectivity measurements and SFA by many studies. It should be emphasized that although hydration structures strongly depend on the surface property (such as hydrophilicity and hydrophobicity), the oscillation in the water molecule density will appear by just assuming a rigid solid surface. As mentioned earlier, hydration structures are due to short-range intermolecular repulsion forces, and more geometric aspects such as the size and shape of the water molecules (or solvent molecules) are more important. The surface properties actually alters the in-plane distribution of the water molecules which will be

2. SOLID-LIQUID INTERFACE STUDIES BY AFM MEASUREMENTS

investigated throughout this thesis. Hence, AFM is an ideal tool which is capable of measuring hydration structures in real-space, which is a unique advantage. The operation principles of the AFM will be stated in section 2.2.

2.2 Operation Principle of AFM

The invention of the STM by Binnig in 1981¹³⁾, opened up a completely new research field in surface science and is the basis of all SPM methodologies developed afterwards. The STM detects the tunneling current between the tip and surface and because the tunneling current rapidly decays when the tip-sample distance increases, atomic scale images were achieved soon after invention, represented by the imaging of the Si(111)- 7×7 surface.²⁰⁾ STM is still used as a powerful method to obtain high resolution images, but has a drawback that it can't be operated on insulating materials due to the operation mechanism. This was solved by the invention of the AFM, which was also developed by Binnig and coworkers in 1986.⁵²⁾ The AFM measures the interaction force acting between the tip and sample, which means there are no restrictions to the sample in principle. Several operation modes have been developed in AFM and will be explained in the following section.

2.2.1 Contact Mode AFM

The contact mode AFM is also called the DC mode or static mode. In the contact mode, the deflection of the cantilever is detected and kept constant to obtain a topographic image. Due to the operation principle, the spring constant needs to be much smaller than the force constant of the interatomic bonds, which is about 10-100 N/m for solids and about 0.1 N/m for biomolecules.¹¹⁾ Therefore the typical spring constants of the cantilevers used in contact mode are around 0.01-5 N/m. Although atomic resolution have been achieved using contact mode AFMs,^{53,54)} the cantilever is perpetually dragged on the surface which damages the surface and tip, suppressing the resolution of the images. To avoid this problem, dynamic mode AFMs were invented which vibrates the cantilever during

imaging. This decreases the contact time of the tip and sample and the damage induced by the contact.

2.2.2 Oscillation Properties of a Cantilever

To understand dynamic mode AFMs, the oscillation properties of a cantilever are first considered. The equation of motion of the oscillation of a cantilever can be written by the following equation⁵⁵⁾

$$m \frac{d^2 z}{dt^2} + \gamma \frac{dz}{dt} + k_z z = F_{ts} + A_o \cos \omega t \quad (2.7)$$

where z is the position of the tip, m and k_z are the effective mass and spring constant of the cantilever, respectively, γ is the damping factor, A_o is the amplitude of the oscillation, F_{ts} is the tip-sample interaction and ω is the angular frequency of the oscillation. $A_o \cos \omega t$ presents the external force applied to oscillate the cantilever. When the tip-sample interaction is zero ($F_{ts} = 0$) and the oscillation is in a steady state, the following ansatz can be made.

$$z = A \cos(\omega t + \phi) \quad (2.8)$$

By substituting eq. 2.8 to eq. 2.7, the amplitude A and phase ϕ of the oscillation of the cantilever can be obtained by the following formula.

$$A = \frac{Q A_o}{k_z \sqrt{Q^2 (1 - \omega^2/\omega_0^2)^2 + \omega^2/\omega_0^2}} \quad (2.9)$$

$$\phi = \tan^{-1} \frac{-\omega \omega_0}{Q(\omega_0^2 - \omega^2)} \quad (2.10)$$

Where ω_0 is the angular resonance frequency. The relationships $\omega_0 = \sqrt{k_z/m}$ and $\gamma = m\omega_0/Q$ were used to deduce eq. 2.9 and eq. 2.10. Fig. 2.3 depicts the frequency characteristics of the oscillating cantilever. The parameters were $\omega_0 = 2\pi \times 140$ kHz, $Q = 10$ and $k_z = 26$ N/m. These parameters are typical conditions when conducting AFM measurements in liquid environments.

2. SOLID-LIQUID INTERFACE STUDIES BY AFM MEASUREMENTS

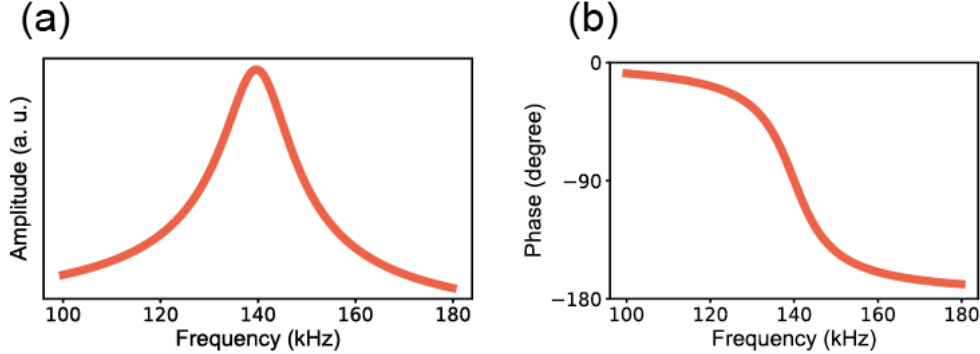


Figure 2.3: The frequency dependency of (a) amplitude and (b) phase of an oscillating cantilever. The curves were obtained by solving eq. 2.9 and eq. 2.10, respectively.

2.2.3 Outline of the Amplitude-Modulation AFM

In 1987, Martin et al.⁵⁶⁾ developed the amplitude-modulation AFM (AM-AFM) which was the first application where the cantilever was oscillated during the measurement. This suppressed the damage induced by the cantilever in static mode AFMs. AM-AFM is operated by measuring the change of the amplitude. Fig. 2.4 illustrates the scheme of the AM-AFM detection and the frequency modulation AFM (FM-AFM) detection mentioned afterwards.. The cantilever is enforced to oscillate near the resonance frequency. When some kind of interaction acts on the cantilever, the resonance frequency shifts and in turn alternates the amplitude of the oscillation. Practically, the excitation frequency is set slightly off-resonance, in order to make the change of the amplitude directly correspond to the frequency shift.

The minimum detectable force gradient of AM-AFM is given by the following formula.⁵⁶⁾

$$\delta F_{min} = \frac{1}{A} \sqrt{\frac{2k_z k_B T B}{\omega_0 Q}} \quad (2.11)$$

Where k_B is the Boltzmann constant, T is the temperature of the system and B is the measurement bandwidth. From eq. 2.11, a simple solution to increase the quality of AM-AFM images is to use a high Q cantilever. However, the time constant of the cantilever in AM-AFM is expressed as $\tau = 2Q/\omega_0$, where τ is the

time constant of the cantilever. This means that a high Q cantilever decreases the bandwidth of the system. For example, in UHV conditions, the Q factor can exceed 50,000 which corresponds to a bandwidth under 1 Hz, which is too slow for application.⁵⁵⁾ On the other hand, AM-AFM have advantages in low Q environments, such as in liquid. In FM-AFM, the bandwidth of the system is restricted to the bandwidth of the frequency shift detector unit, which is typically about 1 kHz. In AM-AFM, there are no limitation beside the time constant of the cantilever and high-speed AFM have been developed and have already observed the movements of biomolecules *in-situ*, such as the conformation change in bacteriorhodopsin due to photoactivation,⁵⁷⁾ the "walking" like translocation of myosin V⁵⁸⁾ and the dynamic rotation of the center ring in annexin V membranes.⁵⁹⁾

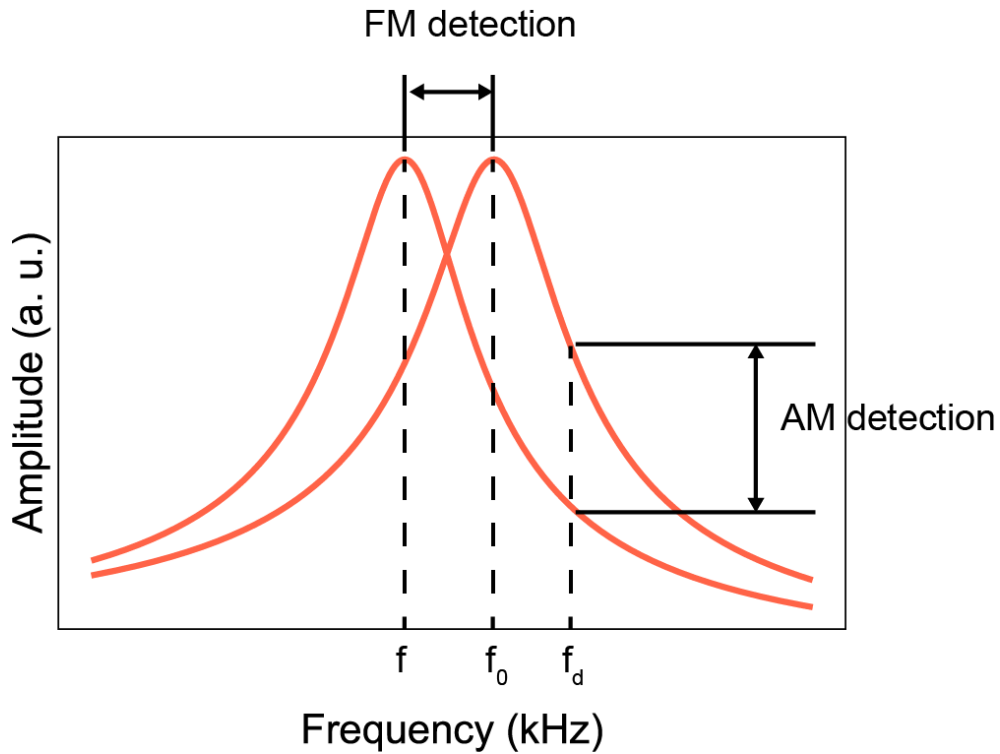


Figure 2.4: Illustration of the AM and FM detection system. The resonance frequency with no tip-sample interaction is depicted as f_0 , the excitation oscillation in AM-AFM is depicted as f_d and the shifted resonance frequency due to tip-sample interaction is depicted as f . In FM detection, the frequency shift from f_0 to f is detected.

2. SOLID-LIQUID INTERFACE STUDIES BY AFM MEASUREMENTS

2.2.4 Operation Principle of Frequency-Modulation AFM

The FM-AFM was developed by Albrecht et al.⁵⁵⁾ in 1991 to allow the usage of high Q cantilevers. In FM-AFM the time constant of the cantilever can be given by $\tau = 1/f_0$ and therefore can conduct AFM imaging in high Q conditions such as UHV. The AFM apparatus operated in this study was developed from a commercial AFM (SPM-9600, Shimadzu). The electronics were lab made and the controller was written in LabVIEW (National Instruments).²⁴⁾ As shown in Fig. 2.4, in FM-AFM, the frequency shift is detected to measure the force acting on the tip. Fig. 2.5 illustrates the block diagram of the FM-AFM utilized in this study. The cantilever was excited by the photothermal excitation method,^{60,61)} where the intensity-modulated laser beam radiated on the beam induces mechanical vibration to the sample. The oscillation of the cantilever was detected by the optical beam deflection method⁶²⁾ and was converted to electrical signals by the position sensitive photo diode (PSPD). The wavelength of laser diodes for the photothermal excitation and optical beam deflection method were set to 670 nm and 405 nm, respectively to prevent cross-talk of the two lasers. The deflection signal was transferred to the phase locked loop (PLL) which detects the frequency shift and converts to a DC voltage. The DC signal was transferred to the feedback controller which controls the piezo scanner. This feedback circuit tracked down the resonance frequency and adjusted the tip-sample distance in order to maintain the same resonance frequency throughout imaging. As mentioned before, rapid operation of FM-AFM is restricted due to the bandwidth of the PLL, which is typically about 1 kHz. The deflection signal was also sent to the phase shifter and automatic gain controller (AGC) circuit which maintains the amplitude of the oscillation. The phase shifter shifts the deflection signal -90° to compensate the phase shift caused in the cantilever oscillation as can be seen in eq. 2.10. This is called a self-excitation loop and is a popular excitation method in FM-AFM. In AFM, interaction forces acting on the tip can be classified into conservative and non-conservative forces. FM-AFM measure conservative forces as the frequency shift as mentioned before. On the other hand, by recording the driving force of the AGC, the non-conservative dissipative force can also be recorded during FM-AFM imaging.

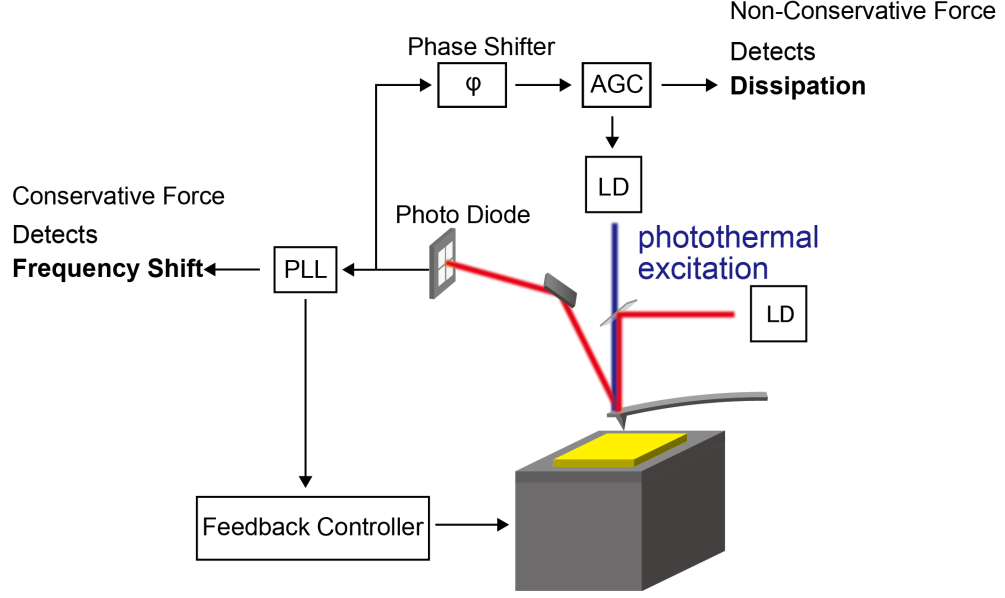


Figure 2.5: A schematic image of the FM-AFM apparatus used in this study. The cantilever was oscillated by the photothermal excitation method and detected by the optical beam deflection method. The deflection signals were transferred to the feedback circuit and self-excitation loop.

The minimum force gradient detected in FM-AFM can be expressed in the following formula.⁵⁵⁾

$$\delta F_{min} = \frac{1}{A} \sqrt{\frac{4k_z k_B T B}{\omega_0 Q}} \quad (2.12)$$

It is clear that the expression is nearly the same for the minimum detectable force gradient in AM-AFM. (eq. 2.11) However, as mentioned before, since the use of high Q cantilevers are restricted in AM-AFM, the minimum detectable force gradient is much lower in FM-AFM and results in high resolution images, especially in UHV. The application of FM-AFM in UHV is one of the hottest topics in the AFM research field. Leo Gross reported the chemical structure of pentacene using a tip functionalized with a CO molecule⁶³⁾ and now many groups have reported beautiful chemical structure images.⁶⁴⁻⁶⁷⁾

2. SOLID-LIQUID INTERFACE STUDIES BY AFM MEASUREMENTS

2.2.4.1 Relationship Between the Force Gradient and Frequency Shift

When a weak tip-sample interaction exists ($F_{ts} \neq 0$) and slightly perturbs the system, it's difficult to rigorously solve the equation. Giessibl derived the relationship between the frequency shift and the tip-sample interaction by applying the Hamilton-Jacobi approach⁶⁸⁾

$$\begin{aligned}\Delta f(z) &= -\frac{f_0}{k_z A_0^2 T_0} \int_0^{T_0} F_{ts}(d + A_0(a + \cos \omega_0 t)) \times A_0 \cos \omega_0 t \, dt \\ &= -\frac{f_0}{\pi k_z A_0} \int_{-1}^1 F_{ts}(z + A_0(1 + u)) \frac{u}{\sqrt{1 - u^2}} \, du\end{aligned}\quad (2.13)$$

where d is the tip-sample distance when the tip is closest to the surface. When the amplitude is small and the force gradient of F_{ts} is constant, eq. 2.13 can be simplified to the following relationship.

$$\Delta f(z) = -\frac{f_0}{2k_z} \frac{dF}{dz}\quad (2.14)$$

dF/dz denotes the force gradient of the tip-sample interaction. This means that when the amplitude is smaller than the characteristic length of the tip-sample interaction, the frequency shift is proportional to the force gradient.

On the other hand, the conversion from frequency shifts to forces is difficult and only a few papers have been published.^{69,70)} One simple solution is to use an analytical deconvolution method introduced from J. E. Sader⁷⁰⁾

$$F(z) = \int_z^\infty \left(1 + \frac{A^{1/2}}{8\sqrt{\pi(t-z)}}\right) \Omega(t) - \frac{A^{3/2}}{\sqrt{2(t-z)}} \frac{d\Omega(t)}{dt} dt\quad (2.15)$$

where $\Omega(t) = \Delta\omega(z)/\omega_0$.

2.2.4.2 Conversion of Experimental Frequency Shift Curves to Force Curves

Practically, the frequency shift versus distance curves are recorded in discrete data points. In order to deconvolute the frequency shift versus distance curves to force versus distance curves, one has to integrate the values of the data points

2.3 Forces Acting on the Tip in Liquid Conditions

using the trapezoidal rule, for example to calculate the force acting on the tip F_j at point j .⁷¹⁾

$$F_j = \frac{2k_z}{f_0} \left\{ C(j) + \sum_{i=j+1}^{N-2} (z_{i+1} - z_i) \frac{g_{i+1} + g_i}{2} \right\} \quad (2.16)$$

Where f_0 is the resonance frequency. $C(j)$ is a correction term and can be calculated by the following formula.

$$C(j) = \Delta f_j (z_{j+1} - z_j) + 2 \frac{\sqrt{A}}{8\sqrt{\pi}} \Delta f_j \sqrt{z_{j+1} - z_j} - 2 \frac{A^{3/2}}{\sqrt{2}} \frac{\Delta f_{j+1} - f_j}{z_{j+1} - z_j} \sqrt{z_{j+1} - z_j} \quad (2.17)$$

Thus, g_k can be calculated by the following formula.

$$g_k = \left(1 + \frac{\sqrt{A}}{8\sqrt{\pi}(z_k - z_j)} \right) \Delta f_k - \frac{A^{3/2}}{\sqrt{2}(z_k - z_j)} \frac{\Delta f_{k+1} - \Delta f_k}{z_{k+1} - z_k} \quad (2.18)$$

Applying eq. 2.16 to 2.18, the experimental frequency shift curves were converted to force curves. The process was conducted by lab-made programs, written in LabVIEW (National Instruments) or Python.

2.3 Forces Acting on the Tip in Liquid Conditions

In an AFM, the cantilever detects the interaction force acting between the probe tip and sample. To elucidate the interactions that should be considered in liquid conditions, the interactions that appear in ultra high vacuum (UHV) conditions will be first introduced.

The simplest case is the interaction between two individual molecules or atoms. The interaction potential between two atoms can be expressed by the Lennard-Jones potential.

$$U_{LJ}(r) = 4\epsilon \left[\left(\frac{\sigma}{r} \right)^{12} - \left(\frac{\sigma}{r} \right)^6 \right] \quad (2.19)$$

Where ϵ is the cohesive energy, σ is the equilibrium interatomic distance and r is the distance between the two atoms. The positive first term stands for Pauli

2. SOLID-LIQUID INTERFACE STUDIES BY AFM MEASUREMENTS

repulsion and the attractive second term represents van der Waals attraction. Both interaction forces will be reviewed in the following section. In UHV, chemical bonding forces also act as attractive forces, but are often included in the van der Waals force term. When the interaction force is integrated over a semi-infinite plane, the interaction potential between an atom and a solid surface $U_{atom-sur}(r)$ can be obtained by the following expression.

$$\begin{aligned} U_{atom-sur}(r) &= 4\epsilon n_0 \int_0^\infty 2\pi x dx \int_0^\infty dx' \left[\left(\frac{\sigma}{\sqrt{r^2 + x'^2}} \right)^{12} - \left(\frac{\sigma}{\sqrt{r^2 + x'^2}} \right)^6 \right] \\ &= 4\pi\epsilon n_0 \sigma^3 \left[\frac{1}{45} \left(\frac{\sigma}{r} \right)^9 - \frac{1}{6} \left(\frac{\sigma}{r} \right)^3 \right] \end{aligned} \quad (2.20)$$

Where n_0 is the number density of the atoms on the surface. To obtain the tip sample interaction, $U_{atom-sur}(r)$ has to be integrated over a paraboloidal tip. The projection of the paraboloidal tip with a curvature radius of R_0 can be expressed as $z = (1/2R_0)x^2$. Thus, the total interaction potential between the tip and sample can be expressed as below.

$$\begin{aligned} U_{ts}(r) &= 4\pi\epsilon n_0^2 \sigma^3 \int_r^\infty 2\pi x \times x \left[\frac{1}{45} \left(\frac{\sigma}{z} \right)^9 - \frac{1}{6} \left(\frac{\sigma}{z} \right)^3 \right] dz \\ &= \frac{2}{3} \pi^2 R_0 \epsilon n_0^2 \sigma^5 \left[\frac{1}{210} \left(\frac{\sigma}{r} \right)^7 - \left(\frac{\sigma}{r} \right) \right] \end{aligned} \quad (2.21)$$

Notice that r in eq. 2.21 denotes the distance between the tip apex and the sample. The force acting on the tip can be calculated by differentiating eq. 2.21.

$$\begin{aligned} F_{ts}(r) &= - \frac{dU_{ts}(r)}{dr} \\ &= \frac{2}{3} \pi^2 R_0 \epsilon n_0^2 \sigma^4 \left[\frac{1}{30} \left(\frac{\sigma}{r} \right)^8 - \left(\frac{\sigma}{r} \right)^2 \right] \end{aligned} \quad (2.22)$$

Fig. 2.6(a) presents the tip-sample interaction force derived from the Lennard Jones potential. The tip sample interaction in UHV is often modeled by eq. 2.22. The operation region of the tip-sample distance differ in AM-AFM and FM-AFM. In AM-AFM, the force is detected by the decrement of the amplitude due to the contact between the tip and sample. On the other hand, FM-AFM is highly sensitive to the frequency shift and is able to operate in the attractive regime mainly caused by van der Waals forces. Thus, FM-AFM is a non-contact

2.3 Forces Acting on the Tip in Liquid Conditions

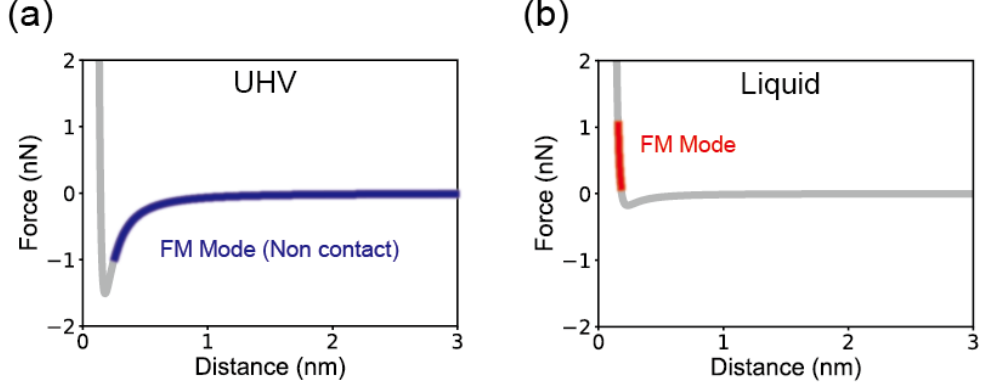


Figure 2.6: The interaction potential between the tip and sample in (a) UHV conditions and (b) liquid conditions, respectively.

method in UHV and is also called non-contact AFM. The operation regimes of FM-AFM is depicted in Fig. 2.6(a). However, in liquid conditions electrostatic forces are screened due to EDL formation. Since van der Waals forces derive from dipolar-dipolar interactions, they are also electrostatic interactions and are screened by the electrolytes in the solution. Hence, it's difficult to detect attractive forces in liquid conditions and instead, the frequency shift in the repulsive regime is utilized. The tip-sample interaction in liquid conditions can be modeled by multiplying the attractive force with a correction factor α in eq. 2.22.

$$F_{ts-liquid}(r) = \frac{2}{3}\pi^2 R_0 \epsilon n_0^2 \sigma^4 \left[\frac{1}{30} \left(\frac{\sigma}{r}\right)^8 - \alpha \left(\frac{\sigma}{r}\right)^2 \right] \quad (2.23)$$

Fig. 2.22(b) displays the tip-sample interaction potential in liquid conditions expressed by eq. 2.23, where $\alpha = 0.2$ was chosen. The red line depicts the typical region where FM detection is operated. In liquid conditions, other interaction forces that aren't expressed in the Lennard Jones potential also act on the tip such as EDL and hydration forces. These interactions may appear as repulsive forces and hence, it's ambiguous whether the tip makes contact with the sample surface. This is a typical problem in FM-AFM imaging in liquid conditions and causes the interpretation of the results very complicated. In this thesis, the threshold in the force mapping technique (the details will be stated in section 2.4) was set higher than many other publications, and thus it was concluded that the tip retracted after it reached the sample surface.

2. SOLID-LIQUID INTERFACE STUDIES BY AFM MEASUREMENTS

2.3.1 Pauli Repulsion and van der Waals Forces

When two atoms get extremely close, a strong repulsion force appears which derives from the overlap of the electron cloud of the atoms. There are several expressions for this repulsion force, such as Pauli repulsion, hard ball repulsion or exchange repulsion. Though the force is a quantum mechanical effect, there are no theoretical formula which express the relationship between the force and distance, and an empirical expression is utilized such as the first term of the Lennard Jones potential. From the steep increment in short range, a simple model is to assume atoms and molecules as hard ball spheres, like billiard balls. The size of atoms and molecules in this thesis follow this assumption. For example, water molecules are assumed as hard ball spheres with a diameter of 0.28 nm. Pauli repulsion is a short range force and plays an important role in hydration structure formation as mentioned in section 2.1.2.

Van der Waals forces are composed of three interactions as presented below.

- Keesom interaction : The dipole-dipole interaction between two polar molecules.
- Debye interaction : The dipole-induced dipole interaction between a polar molecule and a nonpolar molecule.
- London dispersion force : The interaction between instantaneous dipole moments of nonpolar molecules.

Between two atoms or small molecules, all of these forces follow the r^{-6} power law and are grouped together and called van der Waals forces. The van der Waals force between a tip and plane can be expressed by the following equation.

$$F_{vdW}(r) = -\frac{AR_0}{6r^2} \quad (2.24)$$

Where A is the Hamaker constant. The Hamaker constant is a specific value which depends on the material of the tip and sample, and the medium. The decrement of the van der Waals forces in aqueous conditions can be seen by the decrease in the Hamaker constant, where typical values of decrease by about a magnitude.⁷²⁾ The range of van der Waals forces are long and appear in distances from 10 nm to several angstroms.⁵¹⁾ This long range feature makes van der Waals

2.3 Forces Acting on the Tip in Liquid Conditions

forces act as a background in AFM imaging, reducing the resolution. Therefore, imaging in solutions containing electrolytes with high concentration is effective to improve the resolution.²³⁾

2.3.2 EDL Forces

Achieving the mathematical solution of the EDL force acting between two surfaces with different potentials is very complicated. From the charge neutrality condition, eq. 2.3 can be rewritten in the following expression.

$$\frac{d^2\psi}{dx^2} = \frac{2ze\rho_0}{\varepsilon_0\varepsilon} \sinh\left(\frac{ze\psi}{k_B T}\right) \quad (2.25)$$

When $ze\psi/k_B T \ll 1$ stands, eq. 2.25 can be expressed in the following form.

$$\frac{d^2\psi}{dx^2} = \frac{2(ze)^2\rho_0}{\varepsilon_0\varepsilon k_B T} \psi(x) \quad (2.26)$$

Practically, eq. 2.26 is used when $ze\psi/k_B T < 1$ is fulfilled. For example, when $T = 298K$, eq. 2.26 stands when the surface potential is under 25 mV.

Although a solution to the PB equation was derived in eq. 2.5, this expression is accurate only when the distance between the two plates is larger than the Debye length. When the distance gets closer than the Debye length, which is exactly the situation in hydration structure measurements, the PB equation needs to be numerically solved. In this case, the actual expression falls between two limits; the constant potential approximation and the constant charge approximation. Hogg et al., solved the formula against two spheres with the constant potential approximation and found that the interaction potential V can be expressed in the following formula.

$$V = \frac{\pi R_1 R_2}{R_1 + R_2} \left[(\psi_1^2 + \psi_2^2) \ln(1 - e^{-2\kappa H_0}) + 2\psi_1 \psi_2 \ln\left(\frac{1 + e^{-\kappa H_0}}{1 - e^{-\kappa H_0}}\right) \right] \quad (2.27)$$

Where R_1 and R_2 are the radius of the two spheres, ψ_1 and ψ_2 are the surface potential of the two spheres and H_0 is the distance between the two spheres. When $ze\psi/k_B T \ll 1$ stands, Grahame's equation can be simplified to $\sigma_0 = \varepsilon_0\varepsilon\kappa\psi_0$ and eq. 2.27 can be rewritten to the following expression.

$$V = \frac{R_1 R_2}{\pi(\varepsilon_0\varepsilon\kappa)^2(R_1 + R_2)} \left[(\sigma_1^2 + \sigma_2^2) \ln(1 - e^{-2\kappa H_0}) + 2\sigma_1\sigma_2 \ln\left(\frac{1 + e^{-\kappa H_0}}{1 - e^{-\kappa H_0}}\right) \right] \quad (2.28)$$

2. SOLID-LIQUID INTERFACE STUDIES BY AFM MEASUREMENTS

Where σ_1 and σ_2 are the charge density of two spheres and r is the distance between the tip and sample. By differentiating eq. 2.28, the force derived from EDL forces can be deduced. In AFM, the tip is often modeled as a sphere with a radius, R_0 . Using the Derjaguin approximation,⁷³⁾ the tip-sample interaction force due to EDL forces can be expressed as followed.

$$F_{EDL}(r) = \frac{2\pi R_0}{\epsilon\epsilon_0\kappa} \left((\sigma_t^2 + \sigma_s^2) e^{-2\kappa r} + 2\sigma_t\sigma_s \right) \frac{1}{1 - e^{-2\kappa r}} \quad (2.29)$$

Where σ_t and σ_s are the charge density of the tip and sample, respectively. Notice that the EDL force is composed of two forces, osmotic pressure and electrostatic forces. The osmotic pressure is due to the high concentration of electrolytes where the EDLs overlap, which is an entropy loss and always causes a repulsive force. The osmotic pressure is depicted by the $\sigma_t^2 + \sigma_s^2$ in eq. 2.29. On the other hand, the electrostatic force is due to the electrostatic interaction between the counterions of the EDL. Thus, this component can become either attractive or repulsive and is expressed as $2\sigma_t\sigma_s$ in eq. 2.29. Though the name EDL force associates an electrostatic interaction, actually the osmotic pressure component is more dominant⁵¹⁾ and EDL forces can become repulsive even when the surface charge of the tip and sample have opposite signs. By adding the van der Waals force and EDL force, the following expression is obtained.

$$\begin{aligned} F_{DLVO}(r) &= F_{EDL}(r) + F_{vdW}(r) \\ &= \frac{2\pi R_0}{\epsilon\epsilon_0\kappa} \left((\sigma_1^2 + \sigma_2^2) e^{-2\kappa r} + 2\sigma_1\sigma_2 \right) \frac{1}{1 - e^{-2\kappa r}} - \frac{AR_0}{6r^2} \end{aligned} \quad (2.30)$$

2.3.3 Hydration Forces (Solvation Forces)

Hydration forces are due to the overlap of the water molecules constructing the hydration structure. It is said that the first paper which referred about hydration forces was I. Langmuir in 1938.⁷⁴⁾ Due to the oscillation behavior in the water molecule distribution, hydration forces are also known to oscillate and can be expressed by the following empirical formula.

$$F_{hyd}(r) = A \cos\left(\frac{r}{\sigma}\right) \exp\left(-\frac{r}{\sigma}\right) \quad (2.31)$$

2.4 Scanning Modes of AFM Measurements

Where σ is the size of the solvent molecule.(in hydration structures $\sigma = 0.3\text{nm}$) Practically, a background expressed by an exponential component sometimes appeared in the force curves obtained in this thesis and has also been reported in proceeding studies.^{75,76)} The origin of the background are unknown and are suggested to be caused by the tip effect, an entropic effect in order to exclude ions from the solid-liquid interface⁷⁶⁾ or the fluctuation of the surface molecules.⁵¹⁾ In this thesis, it's assumed that hydration forces appear as eq. 2.31 and the exponential background doesn't include information about the hydration structure.

2.4 Scanning Modes of AFM Measurements

Figs. 2.7(a) and (b) illustrate the two scanning methods applied in this study. The constant force mode was applied to obtain the topographic image of the sample surface while the two-dimensional (2D) force mapping technique was conducted to achieve the local hydration structure atop the surface. In the constant force mode, the frequency shift due to the tip-sample interaction is constant throughout the measurement by controlling the tip-sample distance. The movement of the piezo actuator is recorded as the topographic image.

Fig. 2.7(c) presents the details of the 2D force mapping technique. The force mapping technique is an open-loop method. The x and y axes are parallel to the solid surface and the z axis is normal to the sample, as depicted in Fig. 2.7(c). The 2D force mapping technique is a collection of consecutive frequency shift curves. First, the oscillating tip approaches the surface while the frequency shift is recorded. (depicted as 1 in Fig. 2.7(c)) When the frequency shift exceeds the threshold , (depicted as 2) the tip retracts to its original height and moves one pixel next in the x direction (depicted as 3) and continues the sequence until a 2D frequency shift map of the ZX plane is achieved. The threshold is assumed to be the sample surface in this thesis, though this interpretation is not always clear as mentioned in section 2.3.

2. SOLID-LIQUID INTERFACE STUDIES BY AFM MEASUREMENTS

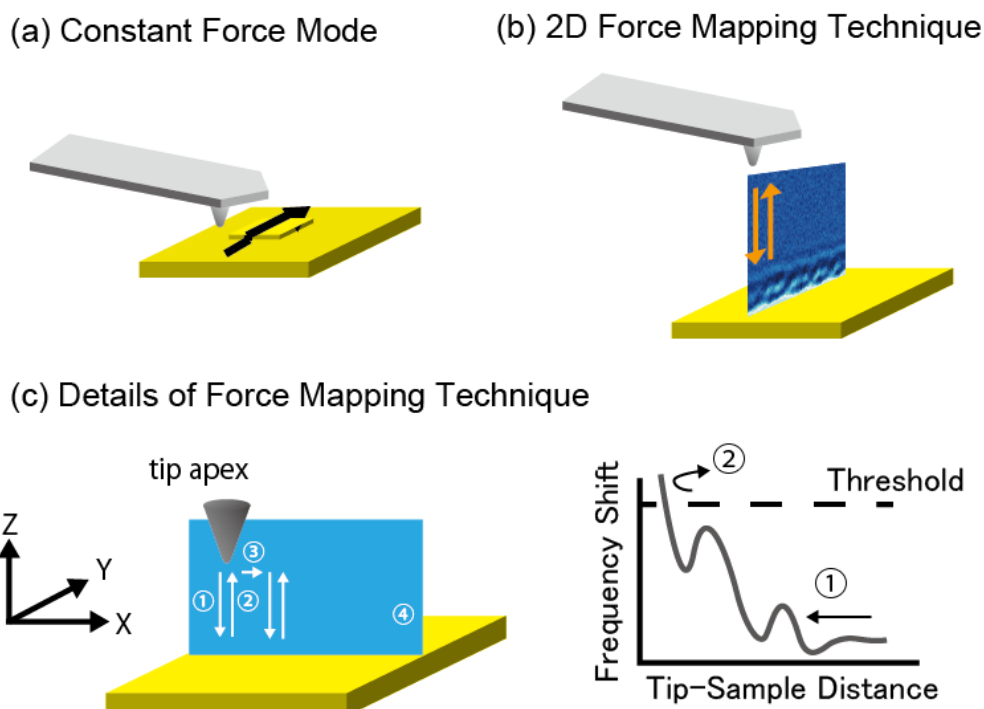


Figure 2.7: A schematic illustration of the scanning modes of the FM-AFM used in this study.

Correlation Between the 2D Frequency Shift Maps and Water Molecule Distribution

Although 2D and 3D frequency shift maps have already been obtained on a wide variety of samples, the physical interpretation of these images is not straightforward. In other words, the position of the water molecules in the images can't easily be defined. In many situations, a MD simulation is also conducted and the experimental force curves are compared with the water molecule distributions obtained from calculations.^{46,75,77} Similarities between the two curves can be recognized and is often concluded that the experimental force curves are due to hydration forces. Other calculation methods such as free energy calculations^{78,79} and 3D reference interaction site model (RISM) theory²³ have been conducted and have also shown analogy with experimental results. Therefore, many researchers now accept that the 2D frequency shift map holds some kind of information about the hydration structure. However, this can't give the position of the

water molecules and is still a difficult problem in FM-AFM hydration structure measurements. This problem will be considered in section 4.5.2.

2.5 Summary

In this chapter, an overview of measuring the solid-liquid interface with an FM-AFM was presented. The formation mechanism of the EDL and hydration structures were described. The forces acting on the tip in liquid conditions were described and simple calculations were conducted to explain the tip-sample forces deriving from Lennard Jones potentials. Also, an overview of the AFM measurement techniques were presented. Especially, the relationship between the frequency shift and tip-sample interaction force were described and the deconvolution method utilizing the Sader method was explained in detail. Furthermore, the force mapping technique was described which was used to achieve local hydration structures.

3

Hydration Structures of Hydrophilic and Hydrophobic SAMs

3.1 Introduction

Hydrophobicity is a general conception recognized in daily life, but the microscopic origin of this property is still not fully understood. Today, one of the biggest goals in surface science is to elucidate the relationship between the macro hydrophobicity and the micro scale hydrophobic surface/water interface. The hydrophobic surface/water interface is a result of minimizing the total free energy of the system including the water molecules. To theoretically solve the problem, all of the water molecules inside the system have to be considered which makes the problem severely complex. Plus, in reality, hydrophobic solutes in the solution such as gas molecules and hydrocarbon contamination easily effect the experimental measurements and causes difficulties in obtaining reproducible results.

When two hydrophobic surfaces approach each other in an aqueous solution, a strong attractive forces acts between the hydrophobic materials called hydrophobic interaction. This force is known to affect a wide variety of phenomena such as protein folding⁸⁰⁾ and stabilization.⁸¹⁾ Therefore, enormous amounts of research have been conducted on investigating the hydrophobic surface/water interface using sum-frequency generation (SFG),³⁹⁾ neutron/X-ray reflectivity^{35,36)}

and atomic force microscopy (AFM).⁸²⁻⁸⁴) A major topic about the hydration structure on hydrophobic surfaces is whether the water molecules form an ordered structure or not. Many SFG measurements on hydrophobic silane self-assembled monolayers (SAMs) have indicated water molecules to form ordered, or sometimes explained as "ice" like structures, due to the strong peak at about 3200 cm^{-1} usually labeled as hydrogen bonds.^{39,85}) However, Tyrode et al., recently pointed out the possibility of water molecules directly interacting with the substrate through gauche defects in the silane SAM.³⁹) The controversy is due to the lack of lateral resolution from the experimental methods and real space measurements are demanded to draw a more detailed picture of the hydration structure on hydrophobic surfaces.

Alkanethiol self-assembled monolayers (SAMs) were chosen as a model system to investigate the hydration structure. Alkanethiol molecules are famous to form a well ordered monolayer with the sulfur head group facing the metal surface and the functional group on the opposite side confronting the atmosphere. Therefore, the functional group modifies the surface property. Another major advantage of alkanethiol SAMs is its simpleness of fabrication, mostly just immersing metal substrates into a solution containing alkanethiol molecules. When two molecules are included in the solution, the molecules either form a mixed-up SAM, or a phase separated SAM where the molecules gather and are homogeneous inside the domains. The formation of phase separated SAMs rely on the functional group and chain length difference of the two molecules.⁸⁶) These phase separated alkanethiol SAMs are an ideal sample to study the local hydration structure of both hydrophilic and hydrophobic surfaces, where the hydration structures of both phases can be measured in the same image, which invalidates the argument of tip effects; an ineluctable problem in AFM imaging.

In this chapter, a 2D force mapping technique was conducted on hydrophilic and hydrophobic alkanethiol SAMs to investigate the relation between the hydration structure and the hydrophilicity/hydrophobicity of the substrate using FM-AFM. To avoid the tip effect, a binary phase separated SAM composed of both hydrophilic and hydrophobic molecules was also fabricated and a cross-sectional 2D frequency shift map of the phases was measured. The results clearly

3. HYDRATION STRUCTURES OF HYDROPHILIC AND HYDROPHOBIC SAMs

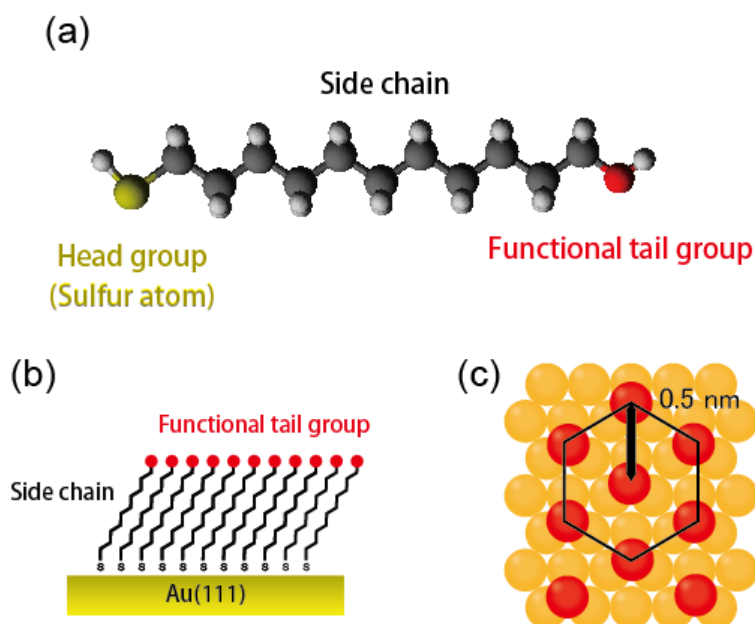


Figure 3.1: (a) Ball-stick model of a 1-hexadecanethiol molecule. (b) Schematic image of a side view of an alkanethiol SAM. (c) Schematic image of the position of the alkanethiol molecules over the Au(111) plane. The red spheres depict the alkanethiol molecules and the yellow spheres represent the gold atoms.

demonstrate that the molecular composition of the surface dramatically alters the hydrophilicity/hydrophobicity of the substrate and the local hydration structure.

3.2 Alkanethiol Self-Assembled Monolayers

The self assembly phenomenon of alkanethiol molecules on gold surfaces has been known for decades called self-assembled monolayers (SAMs).⁸⁷⁾ These SAMs are formed spontaneously when the alkanethiol molecules can access a bare gold surface and also stops growing when the monolayer is formed. Thus, fabricating alkanethiol SAMs is very simple and is applied in many research fields such as electronics,⁸⁸⁾ lubrication⁸⁹⁾ and nanopatterning.⁹⁰⁾ The self assembly phenomenon of alkanethiol molecules are due to the interaction between the surface and the molecule, and between the alkane side chain themselves. Fig. 3.1(a) shows a ball-stick model of a 11-mercapto-1-undecanol molecule (C₁₁OH), which

is a typical alkanethiol molecule forming SAMs. Fig. 3.1(b) presents a schematic image of the side view of a C11OH SAM. Sulfur atoms of the mercapto moiety form a covalent bond with the gold atoms on the surface. The alkane side chain interact with themselves through van der Waals forces which stabilizes the SAM. Hence, the longer chainlength of the alkanethiol molecule makes the SAM more stable and rigid, which effects the whole structure of the SAM. This will be further discussed in chapter 4. Fig. 3.1(c) displays a schematic image of the $(\sqrt{3} \times \sqrt{3})R30^\circ$ structure which is frequently observed in alkanethiol SAMs. Molecules are hexagonally packed with a intermolecular distance of 0.5 nm. In general, long chain alkanes are known to form crystals due to van der Waals interactions between themselves and the intermolecular distance is about 0.4 nm. In alkanethiol SAMs, the molecules tilt for about 30° ⁹¹⁻⁹³) to alter the intermolecular distance from 0.5 nm to $0.5 \times \cos(30^\circ) = 0.43$ nm, which matches the intermolecular distance of alkane crystals.⁹⁴) Back to Fig. 3.1(b), the functional tail groups of the molecule protuberates toward the atmosphere. As a result, a surface modified with an alkanethiol SAM is covered with the functional tail group at the surface and makes alkanethiol SAMs a powerful surface modification technique. The ability to control the surface property and structure of a gold surface makes alkanethiol SAMs a useful model system to study the influence of these properties and the hydration structure above it.

3.3 Experimental

3.3.1 Materials

3-mercaptopropionic acid (C2COOH, purity 99%), 6-mercapto-1-hexanol (C6OH, purity 97%), 1-decanethiol (C10, purity 95%), 11-mercapto-1-undecanol (C11OH, purity 97%), 11-mercaptoundecanoic acid (C11COOH, purity 95%) and 1-hexadecanethiol (C16, purity 95%) were purchased from Sigma-Aldrich, ethanol (purity 99.5%) was purchased from Kishida Chemical and mica substrates were purchased from Furuuchi Chemical.

3. HYDRATION STRUCTURES OF HYDROPHILIC AND HYDROPHOBIC SAMs

3.3.2 Fabrication of an Atomically Flat Au(111) Plane

Alkanethiol SAMs were formed on atomically flat Au(111) films, which were fabricated according to a previous work by DeRose.⁹⁵⁾ First, mica substrates were cleaved with adhesive tape to obtain clean surfaces in ambient condition. Then, the mica substrates were quickly mounted to a lab-made evaporation apparatus and were heated for more than a day at 430°C, prior to evaporation. Deposition was conducted when the vacuum was under 5×10^{-8} Torr. The typical deposition rate was 1.0 Å/s and 150 nm of gold was deposited on the mica substrates. After the deposition, the gold films were continued heated for more than 90 minutes to allow the gold atoms to migrate on the gold surface which enlarged the terraces of the film. This was a crucial step in fabricating gold films with wide terraces.

3.3.3 Fabrication of Alkanethiol SAMs

Alkanethiol SAMs were fabricated by immersing the gold films into ethanol solution containing the alkanethiol molecules. Several concentration conditions of the alkanethiol molecules were performed in this study from 1 μ M to 1 mM, but the concentration didn't affect the quality of the SAMs much. The gold films were either immersed in room temperature, or put in a oven and heated at 70° to 78°C. The immersion was conducted for more than a day. The effect of the immersion temperature on the topography will be discussed in section 4.4.2.

Binary phase separated SAMs were formed according to previous studies conducted by Kakiuchi.^{96–98)} Two alkanethiol molecules were mixed in an ethanol solution and the total concentration was set to 1 μ M. The combination of the two molecules were chosen to have a difference in the chain length of at least 8 units. The tail end group of the longer molecule was always a methyl group and a hydrophilic functional group was choosed for the shorter molecules. The concentration of the short chain alkanethiol molecule was three to four times higher than the long chain alkanethiol molecule. The gold films were immersed for more than a day in room temperature. In these conditions, binary phase separated SAMs were reproducibly fabricated.

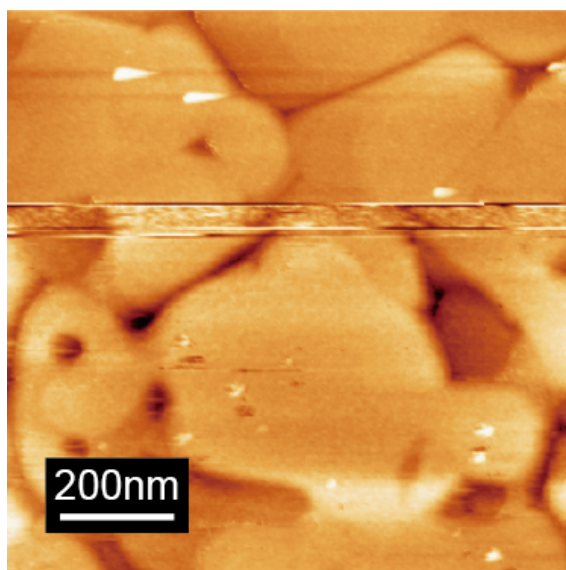


Figure 3.2: A typical wide view topographic image of the gold film fabricated on a mica substrate. The image was obtained in 0.1 M KCl solution.

3.4 Topography of the Au(111) plane

Fig. 3.2 presents a typical wide view topographic image of the gold film deposited on mica. Atomically flat wide terraces were formed which were crucial in fabricating alkanethiol SAMs. Since the interatomic distance of the Au(111) plane is 0.29 nm, the atomic resolution topographic image of the Au(111) plane wasn't imaged in this study. However, from the hexagonal structures of the alkanethiol SAMs formed on the gold film, the surface of the gold film was defined as the Au(111) plane.

3.5 Influence of the Functional Group on Alkanethiol SAMs

3.5.1 Wide View Topographic Images of Alkanethiol SAMs

Fig. 3.3(a) shows a typical wide view image of a C11OH SAM fabricated in 70°. Fig. 3.3(b) presents a cross section profile depicted as a black line in Fig. 3.3(a). In the wide view images, some regions in the SAM were lower than the global

3. HYDRATION STRUCTURES OF HYDROPHILIC AND HYDROPHOBIC SAMs

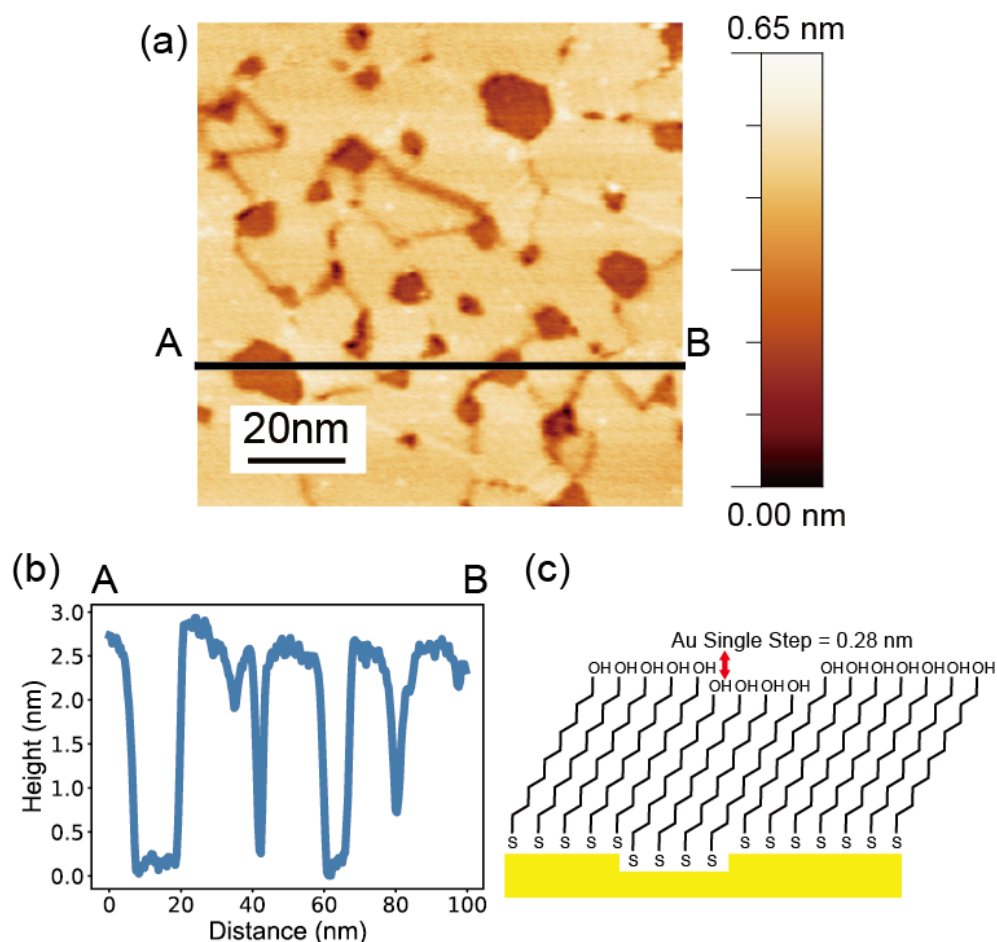


Figure 3.3: (a) A typical wide view topographic image of the C11OH SAM fabricated on a Au(111) plane. The sample was immersed in 70°C for a day. The image was obtained in 0.1 M KCl solution. (b) Cross section profile depicted as a black line in (a). (c) A schematic image of a side view of an etch pit formed on an Au(111) plane.

plane. The height difference was 0.26 nm in this study which matches well with the height difference of a single step in the Au(111) crystal. Therefore, these low areas are concluded to be etch pits which are frequently reported on alkanethiol SAMs⁹⁹⁾ and other organic molecular SAMs formed on metal substrates.^{100–102)} Fig. 3.3(c) displays a schematic image of an etch pit formed on an alkanethiol SAM. The origins of these etch pits haven't been disclosed so far. Early studies from Poirier proposed that etch pits are formed to relax the surface stress when

3.5 Influence of the Functional Group on Alkanethiol SAMs

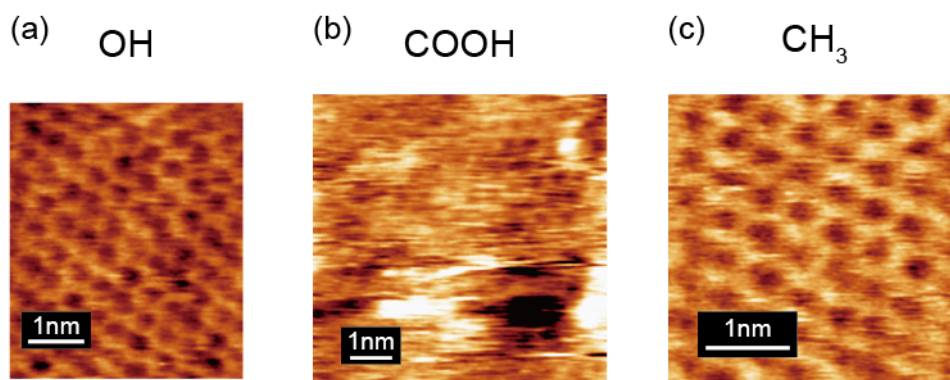


Figure 3.4: (a), (b) and (c) are molecular images of alkanethiol SAMs terminated with the hydroxy group, carboxy group and methyl group, respectively. Each SAM showed a hexagonal ($\sqrt{3} \times \sqrt{3}$)R30° structure. All images were achieved in 0.1 M KCl solution.

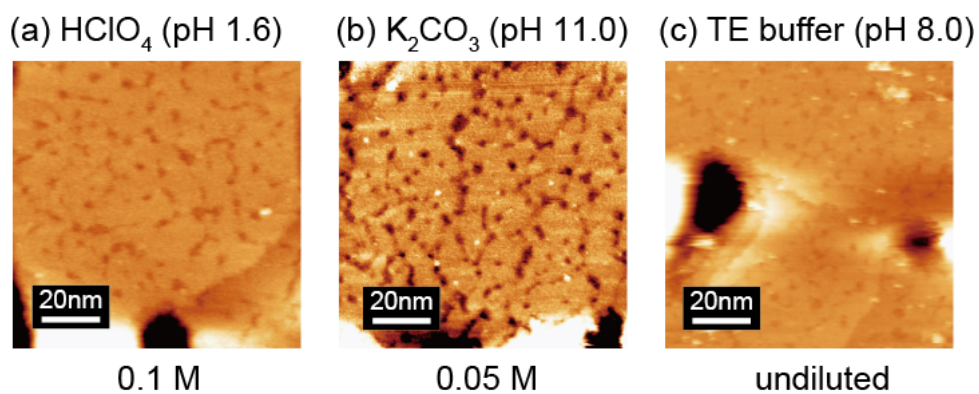
surface reconstruction occurs during alkanethiol SAM formation on the herringbone structure,⁹⁹⁾ but recent papers have argued about the complex gold/sulfur interface where calculations have confirmed that the interface is most stable when gold adatoms are involved.^{103,104)} In this case, the etch pits are formed to supply gold adatoms to the etch pits. This scenario is also supported from SAM formation of perylene derivatives on Cu(111) substrates. Cu adatoms are also involved in this system which results in etch pits, similar to alkanethiol SAMs.^{100,101)} The lines that connect the etch pits are domain boundaries. The molecular images achieved throughout this study were obtained over these flat SAMs. The wide view topographic images of methyl terminated and carboxy terminated SAMs were also measured, but similar images were obtained independent of the tail end functional group. It is worth noting that nanobubbles,¹⁰⁵⁾ frequently reported in AFM imaging of hydrophobic substrates in aqueous solutions, were not observed on methyl terminated SAMs throughout this study.

3.5.2 Influence of the Functional Group on the Molecular Structure

Fig. 3.4 presents the molecular images taken over C11OH, C11COOH and C10 SAMs. The SAMs in Fig. 3.4 were terminated with (a) hydroxy (OH) group,

3. HYDRATION STRUCTURES OF HYDROPHILIC AND HYDROPHOBIC SAMS

without halogen ions



with halogen ions

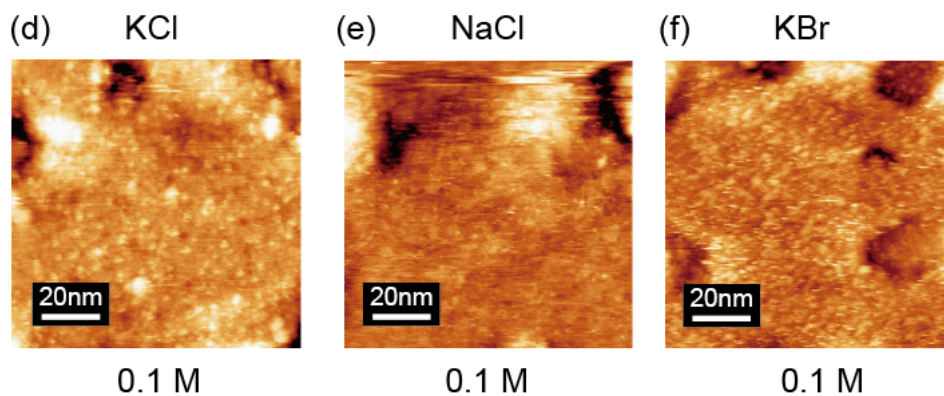


Figure 3.5: $100 \times 100 \text{ nm}^2$ scale topographic images of the C_{11}COOH SAM imaged in aqueous solutions with different electrolytes. The conditions of the electrolytes were (a) 0.1 M HClO_4 , (b) 50 mM K_2CO_3 , (c) TE buffer (undiluted), (d) 0.1 M KCl, (e) 0.1 M NaCl and (f) 0.1 M KBr, respectively.

3.5 Influence of the Functional Group on Alkanethiol SAMs

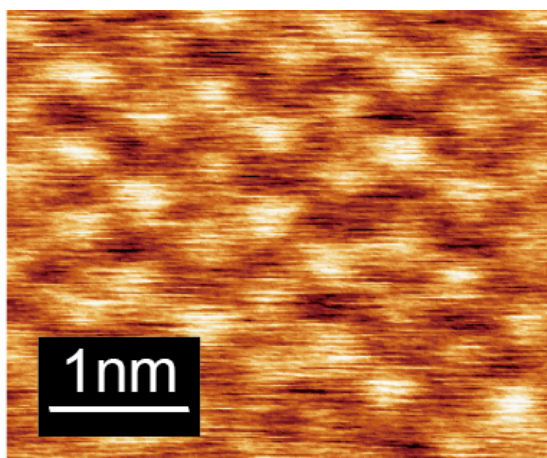


Figure 3.6: Narrow view image of the C11COOH SAM measured in 0.1 M HClO₄ solution. The molecules showed a $(\sqrt{3} \times \sqrt{3})R30^\circ$ structure.

(b) carboxy group (COOH) and (c) methyl group (CH₃), respectively. The chain lengths were similar in all SAMs and the differences were concluded to derive from the tail end functional group. All of the SAMs showed a hexagonal structure with a intermolecular distance of 0.5 nm which are typical features of the $(\sqrt{3} \times \sqrt{3})R30^\circ$ structure. The bulge found in the COOH SAM were repeatedly observed on COOH SAMs in 0.1 M KCl solutions. The bulges appeared even if the KCl solutions were renewed, so the possibility of hydrocarbon contamination was ruled out.

Fig. 3.5 displays the $100 \times 100 \text{ nm}^2$ scale topographic images of the C11COOH SAM in different electrolytes. It was found that the images obtained in solutions containing halogen ions (KCl, NaCl and KBr) were corrupted, while the images achieved in solutions not containing halogen ions were clearly imaged. Fig. 3.6 shows the molecular image of the C11COOH SAM imaged in 0.1 M HClO₄ solution. The image depicts a $(\sqrt{3} \times \sqrt{3})R30^\circ$ structure, which is consistent with previous STM studies observing the COOH terminated alkanethiol SAMs.^{106,107} Hence, the bulges recognized in the molecular images of COOH terminated SAMs (such as in Fig. 3.4(b)) were caused by the halogen ions in the solution. However, since the isoelectric point of COOH terminated SAMs are reported to be 3.5,¹⁰⁸ the COOH functional groups are predicted to deprotonate and become negatively charged. Therefore, it's counterintuitive that the halogen anions interacted with

3. HYDRATION STRUCTURES OF HYDROPHILIC AND HYDROPHOBIC SAMS

the negatively charged COO^- groups. Considering that clear topographic images were obtained in a wide pH region in solutions free of halogen ions, it may be possible that a stronger interaction other than the repulsive electrostatic interaction occurred between the halogen anions and the COO^- groups and caused these problems. In this study, it wasn't possible to clarify the mechanism why the halogen ions corrupted the topographic images.

3.5.3 Hydration Structure Measurements

Figs. 3.7 (a) and (b) display the 2D frequency shift map taken over a C11OH SAM and a C11COOH SAM, respectively. The yellow line in the images is the position where the tip retracted in the force mapping technique and corresponds to the surface of the sample. The yellow line showed a sinusoidal pattern which is due to atomic corrugation of the SAM surface. The protrusions of the line (depicted in blue arrows) correspond to the positions where alkanethiol molecules are positioned and the valleys (depicted in red arrows) stand for the position between alkanethiol molecules. In the 2D frequency shift maps a dot like pattern was observed on the C11OH and C11COOH SAM. The residence time of water molecules inside the hydration structure of an alkanethiol SAM have been calculated to be no longer than several tens of picoseconds,^{109,110} while the period of the cantilever oscillation cycle is no more faster than several microseconds in this experiment. Therefore, the 2D frequency shift maps reflects the time average or probability distribution of the water molecule density. Dot like patterns mean that the water molecules are locally restricted to the surface due to hydrogen bonds with the hydroxy and carboxy functional groups. Figs. 3.7 (c) and (d) depict the frequency shift versus distance curve extracted from Fig. 3.7 (a) and (b), respectively. In Fig. 3.7(a) the curves were extracted from the valleys and protrusions from three different points depicted in the blue and red arrows in Fig. 3.7(a), while in Fig. 3.7(b) the curves were averaged from two points depicted by the arrows. An oscillation was found on the frequency shift versus distance curve with a period of 0.3 nm, which matches the size of a single water molecule and is the biggest evidence that the oscillation is due to hydration forces. Figs. 3.7(e) and (f) present the force versus distance curves converted from

3.5 Influence of the Functional Group on Alkanethiol SAMs

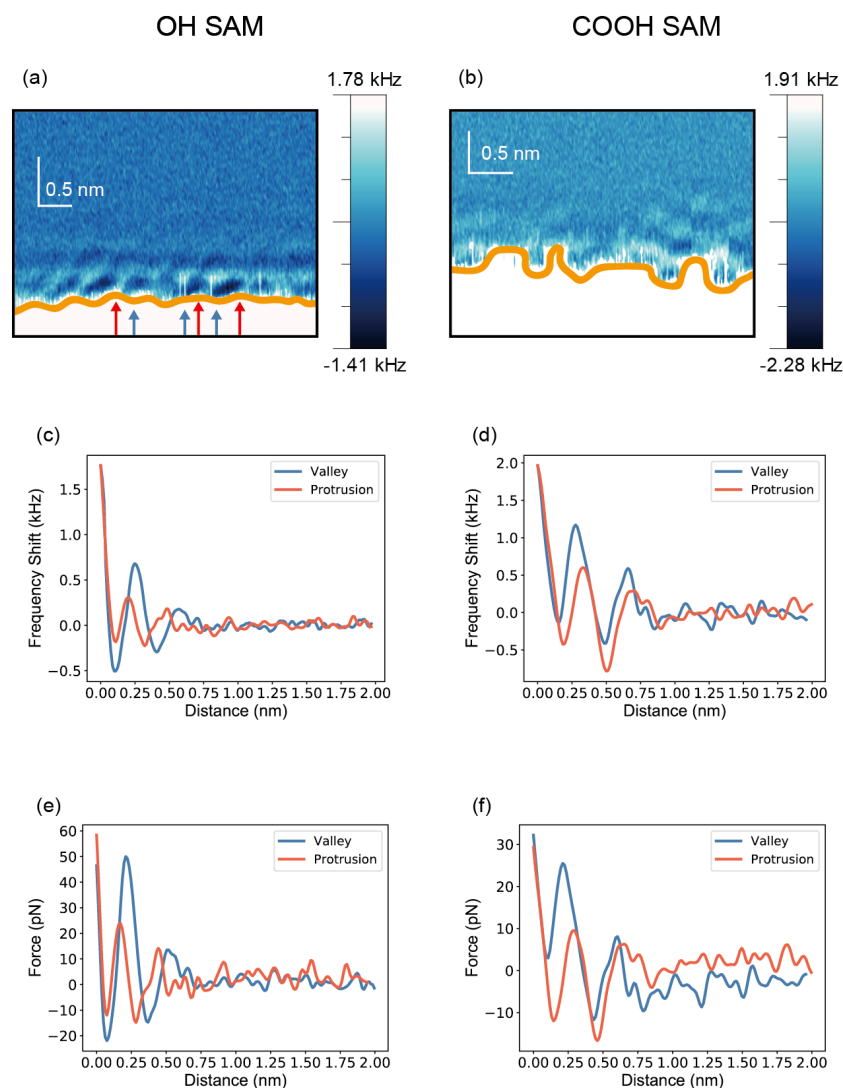


Figure 3.7: 2D frequency shift maps taken over (a) C11OH SAM and (b) C11COOH SAM, respectively in 0.1 M KCl solution. The yellow line in the image depicts the position where the tip retracted from the surface which corresponds to the surface of the sample. The blue and red arrows show the valley and protrusions of the sample. Both 2D frequency shift maps were measured over the $(\sqrt{3} \times \sqrt{3})R30^\circ$ structure. (c) and (d) are frequency shift versus distance curves extracted from (a) and (b), respectively. (e) and (f) are force versus distance curves converted from (c) and (d), respectively, using the Sader method.⁷⁰⁾

3. HYDRATION STRUCTURES OF HYDROPHILIC AND HYDROPHOBIC SAMS

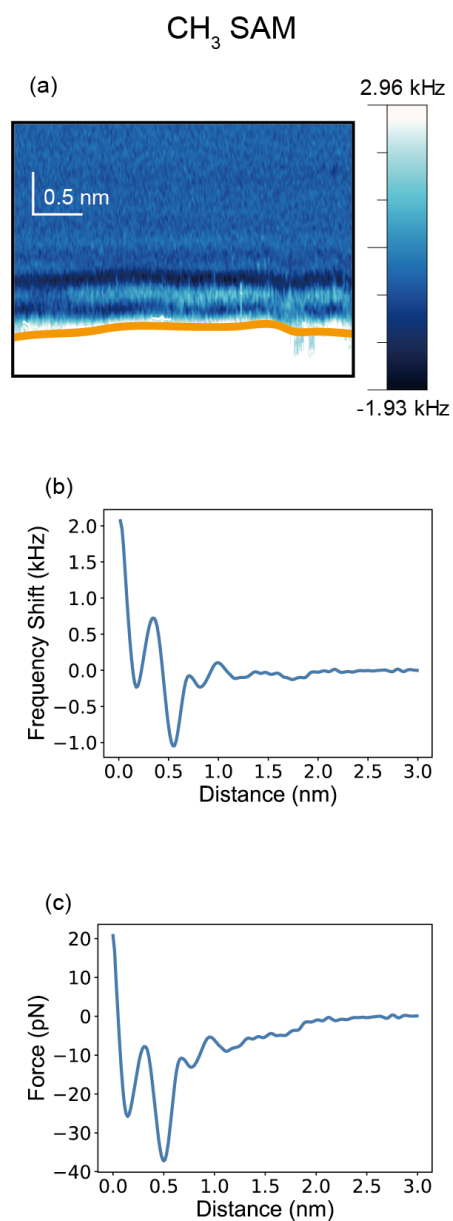


Figure 3.8: (a) presents a 2D frequency shift map taken over a C10 SAM in 0.1 M KCl solution. The yellow line in the image depicts the position where the tip retracted from the surface which corresponds to the surface of the sample. The 2D frequency shift map was measured over the $(\sqrt{3} \times \sqrt{3})\text{R}30^\circ$ structure. (b) is the frequency shift versus distance curves extracted from (a). (c) is the force versus distance curves converted from (b).

3.5 Influence of the Functional Group on Alkanethiol SAMs

Figs. 3.7(c) and (d), respectively, using the Sader method.⁷⁰⁾ The amplitude of the hydration force of the C11OH SAM was larger than the amplitude of the C11COOH SAM. It is known that hydrogen bonds between carboxy groups and water molecules are stronger than the hydrogen bonds between hydroxy groups and water molecules.¹¹¹⁾ Thus, the measured hydration force is inconsistent with this fact. This is due to the variation in the quality of the cantilever, specifically the sharpness of the tip apex. This quality variation of a cantilever is the biggest disadvantage in AFM and questions the reliability of quantitative values and sometimes appears as artifacts in topographic images. Hence, to overcome this problem the samples have to be imaged with the same tip and ideally, should be measured at the same time to prevent the shape of the tip to alternate between measurements. This problem will be argued in detail in section 3.6.

Fig. 3.8 (a) shows the 2D frequency shift map taken over a C10 SAM. Notice that the 2D frequency shift maps obtained in Figs. 3.7(a), (b) and Fig. 3.8(a) are all measured with different cantilevers. Fig. 3.8(b) displays the frequency shift versus distance curve extracted from Fig. 3.8(a). The frequency shift versus distance curve was averaged for all 256 lines in the 2D frequency shift map. In Fig. 3.8(a), line patterns were observed which indicate that the water molecule density is equal on any position on the C10 SAM. Thus, the water molecules are not constrained and move around freely in a quasi 2D plane. This is consistent with the fact that the methyl groups of the C10 SAM can't interact with the water molecules through hydrogen bonds or coulomb interactions. Previous studies measuring the hydration structure on other hydrophobic surfaces such as HOPG have also shown an in-plane homogeneous distribution of water molecules.⁸²⁾ The period of the oscillation was 0.3 nm which matches the size of a single water molecule. Fig. 3.8(c) presents the force versus distance curve converted from the frequency shift versus distance curve using the Sader method.⁷⁰⁾ Comparing the oscillation amplitude in the force versus distance curve of the C10 SAM (Fig. 3.8(c)) with the oscillation amplitude in the C11OH SAM (Fig. 3.7(e)), the amplitude was larger on the C11OH SAM than the C10 SAM. However, the local water molecule density of the first hydration peak have been calculated from MD simulations and show a higher density on methyl terminated SAMs,¹¹²⁾ which is contractive with this result. Again, as in the case of the C11OH and

3. HYDRATION STRUCTURES OF HYDROPHILIC AND HYDROPHOBIC SAMs

C11COOH SAMs, the quantitative values of the hydration force doesn't agree with proceeding works and shows the impact of using different cantilevers in AFM measurements.

Besides the locality of the water molecules in the hydration structure, another topic at the hydrophobic surface/water interface is whether "depletion layers" exist at the interface. As mentioned before, the hydration structure over hydrophobic surfaces have been intensively investigated using neutron and X-ray reflection techniques. Many of these studies have suggested the existence of a low water molecule density layer which are called a depletion layer.^{34,113)} The length of the depletion layer varies between publications from 2-5 Å to several nanometers.³⁴⁾ Comparing the 2D frequency shift map of the C11OH and C10 SAMs, the boundary of the SAM and water phase has atomic corrugation in the C11OH SAM while most of the boundary was flat and didn't show any roughness in the C10 SAM. This suggests that the tip reaches the surface in the hydrophilic C11OH SAM, while the tip is restricted from reaching the surface with a certain distance on the C10 SAM. This topic will be argued again later in section 3.6.

3.5.4 Effect of Hydrocarbon Contamination on Hydrophobic Surfaces

Though reproducibility was achieved, it was extremely difficult to measure the hydration structure on hydrophobic substrates. Fig. 3.9 (a) displays a typical 2D frequency shift map taken over a C16 SAM. Figs. 3.9 (b) and (c) show the frequency shift versus distance curve and the dissipation versus distance curve, respectively. The influence of the frequency shift versus distance curves were exceeded from the dissipation versus distance curves according to a previous study.¹¹⁴⁾ The frequency shift versus distance curve and dissipation versus distance curve were averaged over all lines in the image. (256 lines) Abnormal features can be confirmed in Fig. 3.9 (a) compared to hydration structures on hydrophilic substrates. (i) The period of the oscillations were 0.5 nm, (ii) a dip in the frequency shift curve was found around 2 nm from the surface (iii) a sharp peak in the dissipation signal found in the same position as the dip in (ii). The same features were also reported recently by Schlesinger and Sivan, where

3.5 Influence of the Functional Group on Alkanethiol SAMs

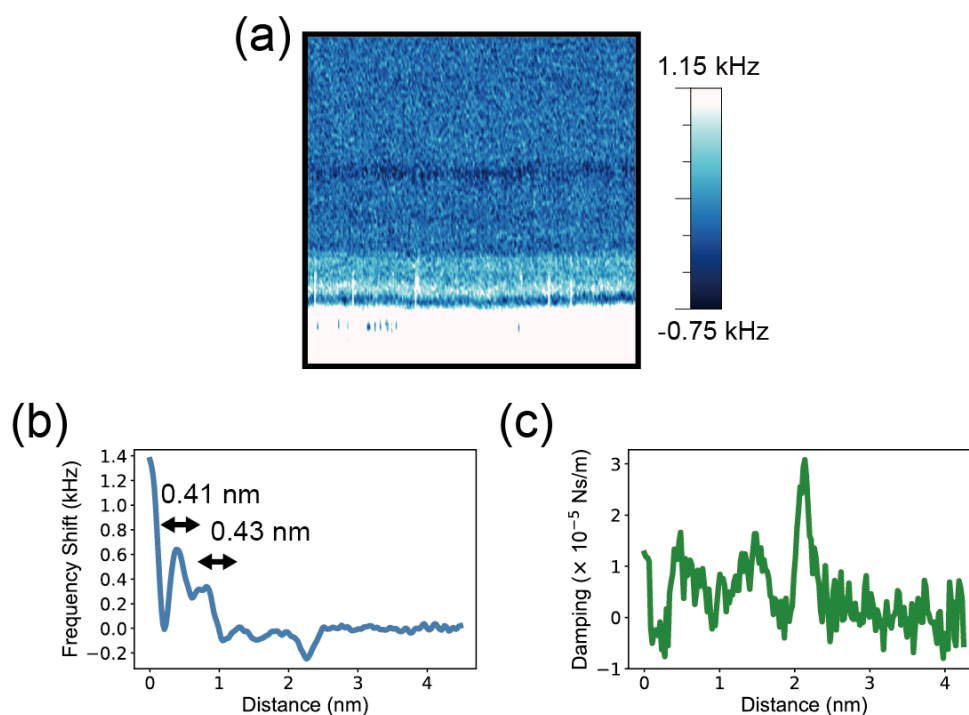


Figure 3.9: (a) 2D frequency shift image measured over a C16 SAM. (b) 1D frequency shift versus distance curve extracted from (a). (c) 1D dissipation versus distance curve taken from the same position of (b) was extracted.

they used FM-AFM to study the hydration structures of HOPG and fluorinated silane SAMs.^{83,84}) Their paper concluded these characteristics were due to gas molecules accumulated on the hydrophobic surface, which form a condensed gas molecule layer. The accumulation of gas molecules on hydrophobic surfaces has also been predicted in MD simulations,¹¹⁵) and matches with the recent trend that gas molecules are involved in hydrophobic interactions. However, this scenario doesn't explain the frequency shift dip observed in this study. Generally, nitrogen molecules are mostly thought of as a hydrophobic solute. If a hydrophilic tip moves from a water layer to a hydrophobic layer, this should not energetically favor the tip, causing a repulsive force and should result in a positive frequency shift. Nonetheless, it is reasonable enough to think that the frequency shift dip derives from some kind of hydrophobic molecule gathering on the hydrophobic surface.

3. HYDRATION STRUCTURES OF HYDROPHILIC AND HYDROPHOBIC SAMS

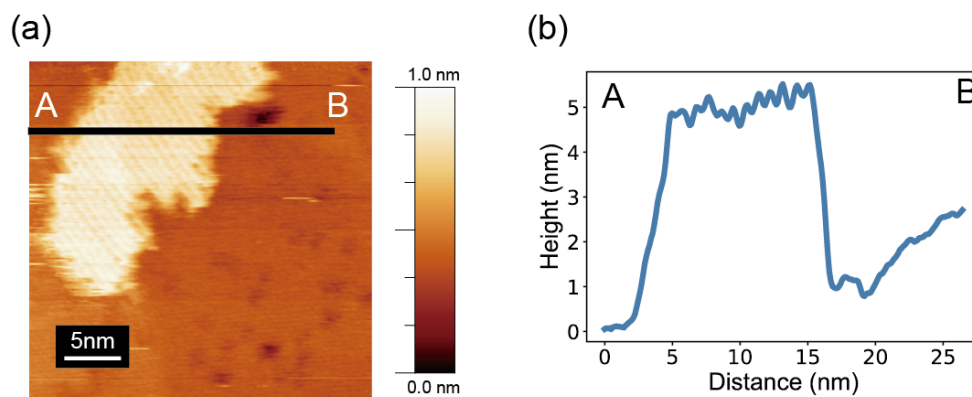


Figure 3.10: (a) Topographic image of a C16 SAM observed in 0.1 M KCl solution. (b) Cross-sectional profile of the contamination depicted by a black line in (a). The height difference was 0.5 nm which matches the oscillation period measured in frequency shift versus distance curves.

Another issue on the hydrophobic surface/water interface is the involvement of hydrocarbon contamination. Although HOPG is considered as a typical hydrophobic substrate with a contact angle (CA) of about 90 degrees, recent studies suggest airborne contamination strongly alters the CA and that a pristine HOPG substrate is more hydrophilic than expected.¹¹⁶⁾ In this investigation, the three features mentioned above frequently occurred when the cantilever holder cleaning was inadequate. (i.e. only sonicating in pure water) The author also thinks that this could be the same case in the previous reports.⁸⁴⁾ Besides the features mentioned above, they also reported a periodic line pattern on HOPG with a period of about 4-5 nm. Periodic structures were also observed on a hydrophobic C16 SAM in 0.1 M KCl solution and is presented in Fig. 3.10. The height of the periodic structure was 0.5 nm which matches the oscillation distance pointed out in (i). The periodic pattern on HOPG have also been reported by several groups in liquid^{84,117)} and in ambient conditions,^{118,119)} and are concluded to be the result of gas enrichment of the surface,^{84,117)} or the self-assembly of some kind of hydrocarbon contamination.¹¹⁸⁾ For example, the images well resemble the self-assembly of alkanes on HOPG in aqueous solutions.¹²⁰⁾ From these reasons, a hypothesis was made that the 2D frequency shift map features are strongly correlated with contamination and not gas molecules dissolved in the solution.

3.5 Influence of the Functional Group on Alkanethiol SAMs

Although the negative frequency shift dip in Fig. 3.9 is peculiar, the behavior has strong analogies with a recent work measuring the collapse of micelles with FM-AFM.¹²¹⁾ In this work, (1) an oscillation period of 0.4 nm was found which is larger than a single water molecule, (2) a negative frequency shift dip was found around 2 nm from the surface. When the cantilever penetrates the micelle in the approach process, the surfactant molecules are forced to reconstruct and the long chain of the molecule orientate parallel to the surface. Just after the tip penetrates the micelle, there is not enough space for anything besides the surfactant molecules to get into the space between the tip and sample. Therefore, virtually "nothing" is there and an attractive force occurs on the tip and causes (2). After that, the cantilever shows a 0.4 nm oscillation which matches the size of the diameter of long-chain alkanes.¹²²⁾ A similar phenomenon is hypothesized to occur during this experiment. The alkanethiol molecules physisorbed to the SAM or desorbed from the substrate gathered near the SAM surface and spontaneously formed a structure, which reconstructs after the tip retracts from the surface. Since the dissolution of gas molecules wasn't controlled in this experiment, it can't be ruled out the influence of gas molecules but in that case, the reason for the negative frequency shift should also be taken into account.

The features mentioned above were measured frequently when a conventional cleaning process was conducted to the cantilever holder, which was just sonicating the holder with deionized water. Suspecting that the peculiar results were due to hydrocarbon contamination, the cleaning process was reexamined to the following procedure, 15 minutes of sonication in ethanol and deionized water and then 30 minutes of UV/ozone cleaning. In the conventional cantilever holder, an adhesive agent was used to build the holder. This prevented conducting UV/ozone cleaning because the adhesive agent decomposed when the UV/ozone cleaning was conducted. Thus, a new cantilever holder was designed and utilized in the AFM measurements on hydrophobic samples. This decreased the measurement of the peculiar results and 0.3 nm oscillations due to hydration forces were measured. The design of the new cantilever holder will be presented in section 5.2.

3. HYDRATION STRUCTURES OF HYDROPHILIC AND HYDROPHOBIC SAMs

3.6 Measurements of Binary Phase Separated SAMs

As mentioned in section 3.5.3, although the local hydration structure was imaged with three different functional groups, the quantitative values were unreliable due to the variation of the tip quality. To overcome this problem, a binary phase separated SAM was fabricated which is composed of two different functional groups. By measuring the local hydration structure crossing two different phases, the hydration structure could be directly compared with the same tip, which should enhance the reliability of the experiments. Binary phase separated SAMs have been fabricated by several methods,^{97,123,124)} but the simplest method is to immerse gold substrates into an organic solution containing two alkanethiol molecules mixed together.⁹⁶⁾ In this case, the interaction between the gold substrate and the alkanethiol molecules, and the interaction between the different alkanethiol molecules strongly effect the binary phase separated SAM. This means that the coverage ratio of the two alkanethiol molecules aren't equal with the concentration ratio of the two molecules in the solution and strongly depends on the fabrication conditions. For example, the chain length, functional group, total concentration and concentration ratio of the two alkanethiol molecules have a huge impact on the coverage ratio. Previous studies report binary phase separated SAMs when the following conditions are satisfied; (a) the two molecules have different chain length (usually more than 10) and (b) the longer molecule has a methyl functional group. Based on these requirements, a binary phase separated SAM composed of C6OH and C16 molecules were fabricated and the influence of the surface hydrophilicity/hydrophobicity on local hydration structures was investigated.

3.6.1 Single Phased SAMs

Figs. 3.11(a) and (b) present the narrow view topographic image of a C6OH SAM and C16 SAM, respectively. Both images showed a hexagonal pattern with a intermolecular distance of 0.5 nm which matches the features of a $(\sqrt{3} \times \sqrt{3})R30^\circ$ structure. It should be noted that the $(\sqrt{3} \times \sqrt{3})R30^\circ$ structure and the

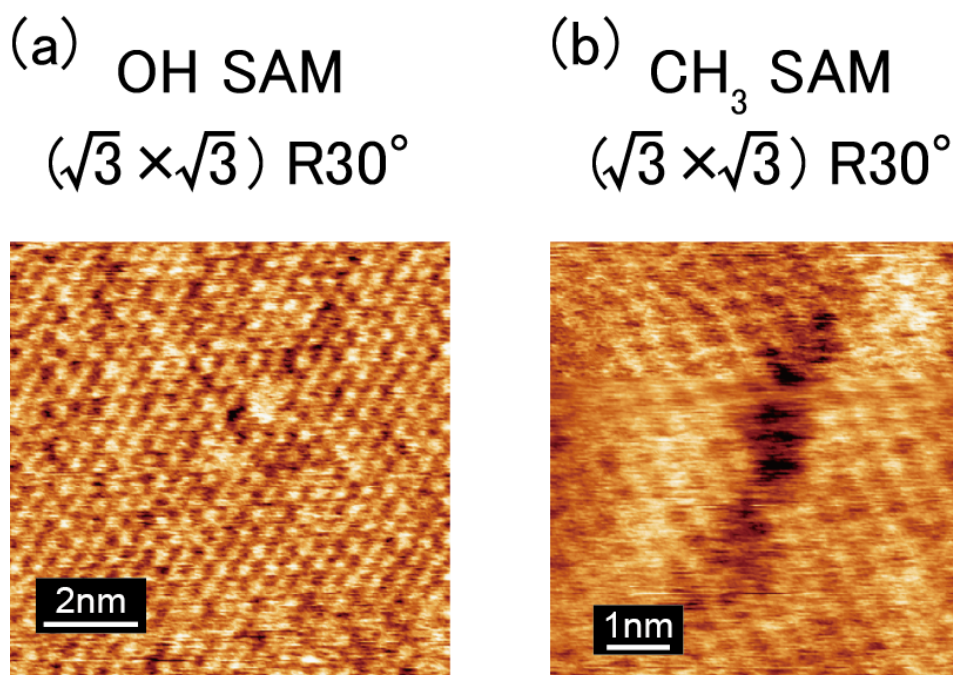


Figure 3.11: Molecular scale image of (a) C6OH SAM and (b) C16 SAM, respectively. Both images showed a hexagonal pattern which represent the $(\sqrt{3} \times \sqrt{3})R30^\circ$ structure.

$c(4 \times 2)$ superlattice structure were both observed on the C6OH SAM, while the $(\sqrt{3} \times \sqrt{3})R30^\circ$ structure was only found on the C16 SAM. (The molecular image and hydration structure of the $c(4 \times 2)$ superlattice structure of a C6OH SAM is discussed in section 4.5.1.)

Figs. 3.12(a) and (b) display the 2D frequency shift map obtained over a C6OH and C16 SAM, respectively. The C6OH SAM presented a dot like pattern which corresponds to a inhomogeneous in-plane distribution of water molecules. On the other hand, the C16 SAM showed a line pattern which stands for the homogeneous in-plane distribution of water molecules. These results are consistent with 2D frequency shift maps achieved over a C11OH and C10 SAM and are not due to the variation of the tip quality.

3. HYDRATION STRUCTURES OF HYDROPHILIC AND HYDROPHOBIC SAMS

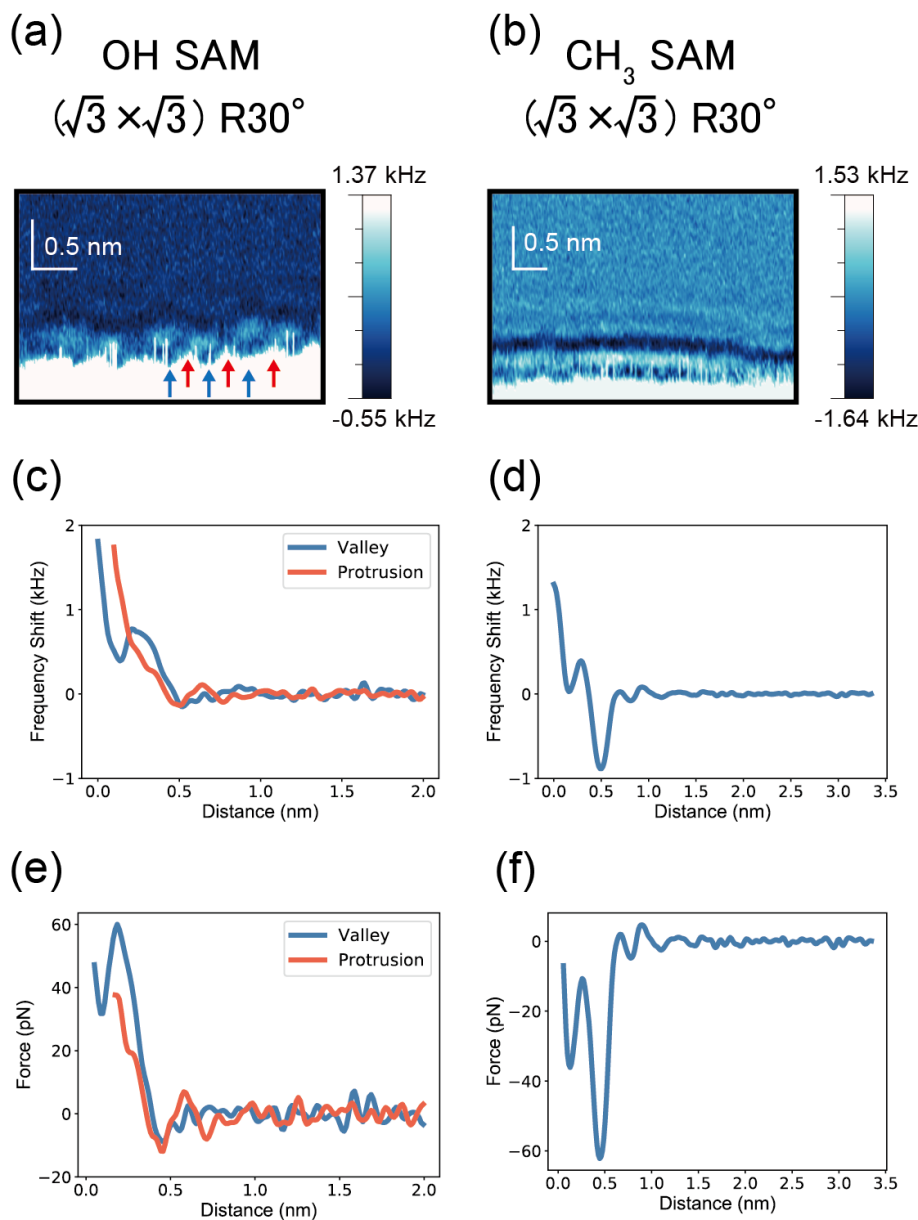


Figure 3.12: (a), (b) 2D frequency shift map measured over C6OH SAM and C16 SAM, respectively. (c), (d) Frequency shift versus distance curve extracted from (a) and (b), respectively. The red and blue curves in (c) represent the frequency shift versus distance curves extracted over the valleys and protrusion of the SAM surface. The blue and red arrows in (a) depict the position where the frequency shift versus distance curves were extracted. (e), (f) Force versus distance curves extracted from (c) and (d), respectively, using the Sader method.⁷⁰⁾

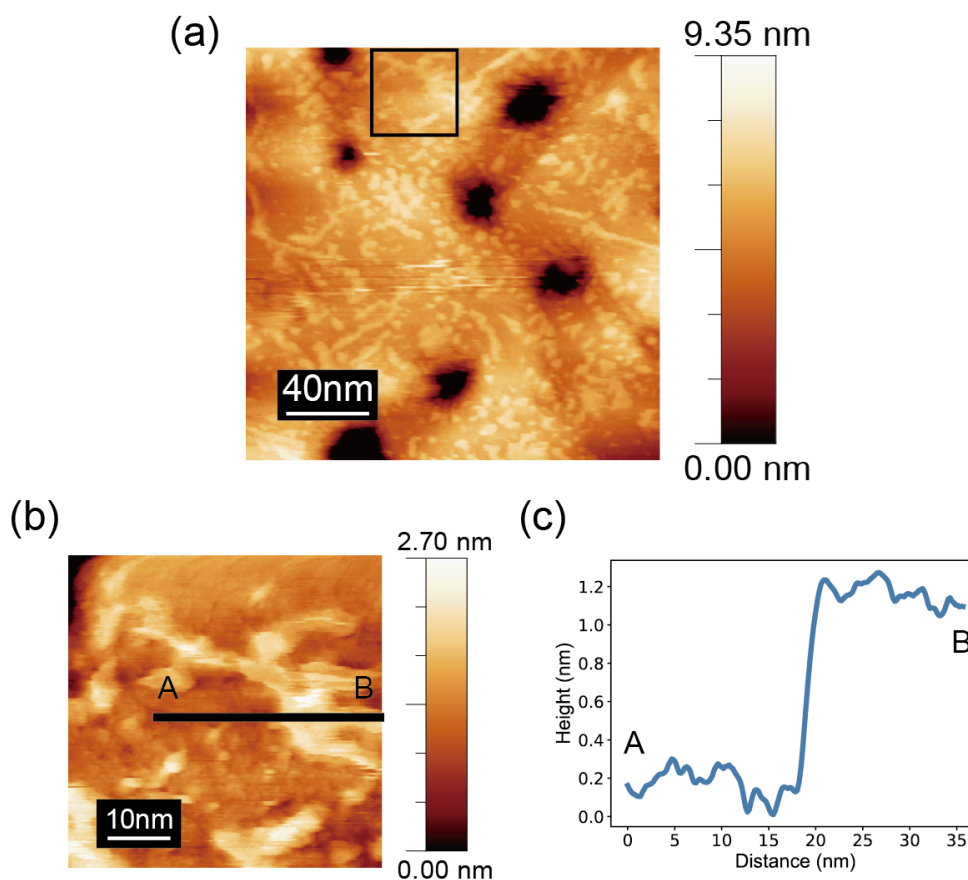


Figure 3.13: (a) Wide view topographic image of a binary phase separated SAM composed of C6OH and C16 molecules. (b) A magnified topographic image of (a). (c) Cross sectional profile of the phase separated SAM depicted in the black line in (b). The height difference was 1.0 nm which matches the values obtained from molecular models.

3.6.2 Binary Phased Separated SAMs

Fig. 3.13 (a) displays a $200 \times 200 \text{ nm}^2$ scale topographic image of the binary phase separation SAM composed of C6OH and C16 molecules. Fig. 3.13 (b) presents a magnified topographic image of the area depicted by a black square in Fig. 3.13(a). Fig.3.13 (c) shows the profile of the black line in Fig. 3.13(C). The height difference was approximately 1.0 nm. The length of the alkanethiol molecules was calculated to be 0.90 nm for C6OH molecules and 2.04 nm for C16 molecules, respectively. Thus, considering a 30° tilt, the height difference was

3. HYDRATION STRUCTURES OF HYDROPHILIC AND HYDROPHOBIC SAMS

predicted to be 0.99 nm, which well matches the measured height difference in Fig. 3.13(c) Hence, it was confirmed that the binary phase separated SAM was composed of C6OH and C16 molecules were successfully fabricated.

Fig. 3.14 (a) shows the 2D frequency shift map taken over both the C6OH and C16 SAM phase. Fig. 3.14 (b) displays the frequency shift versus distance curves extracted from the C6OH and C16 phase in Fig. 3.14 (a). Fig. (c) shows the force versus distance curve converted from Fig. 3.14 (b) using the Sader method.⁷⁰⁾ Two features can be seen from Fig. 3.14 (a). (I) The hydration structure over the C6OH SAM displayed a dot like pattern while the C16 SAM showed a line pattern (II) The height difference was 1.2 nm which is 0.2 nm longer than the topographic image (Fig. 3.13) and the molecular model. (I) strongly supports the conclusion made in the one phase hydration measurements that OH terminated SAMS have an inhomogeneous in-plane water molecule distribution while CH₃ terminated SAMs have a homogeneous in-plane water molecule distribution. Since proceeding studies have shown the same trend on hydrophilic^{23,46)} and hydrophobic^{82,84)} samples, the in-plane water molecule distribution can be said to have a strong correlation with the overall contact angle. (II) is due to the depletion layer formed over hydrophobic surfaces. The value 0.2 nm matches a typical value reported from neutron/X-ray reflection measurements. Also, when the force versus distance curve measured over the C16 SAM was fitted with van der Waals forces, the fitting matched well when it was assumed that the tip was 0.2 nm apart from the surface when the tip retracted. This means that the C16 force versus distance curve was fitted with the following equation.

$$F'_{vdW}(r) = -\frac{AR_0}{6(r + 0.2[nm])^2} \quad (3.1)$$

In eq. 3.1, the Hamaker constant of the van der Waals force was 9.4×10^{-21} J which matches with proceeding studies.^{84,125)} To explain why the tip retracts at the depletion layer, the relation between the water molecule distribution and the force acting on the tip will be considered. A simple but yet, effective equation to interpretate force versus distance curves obtained from FM-AFM was recently demonstrated by Watkins and Amano called the solvation tip approximation

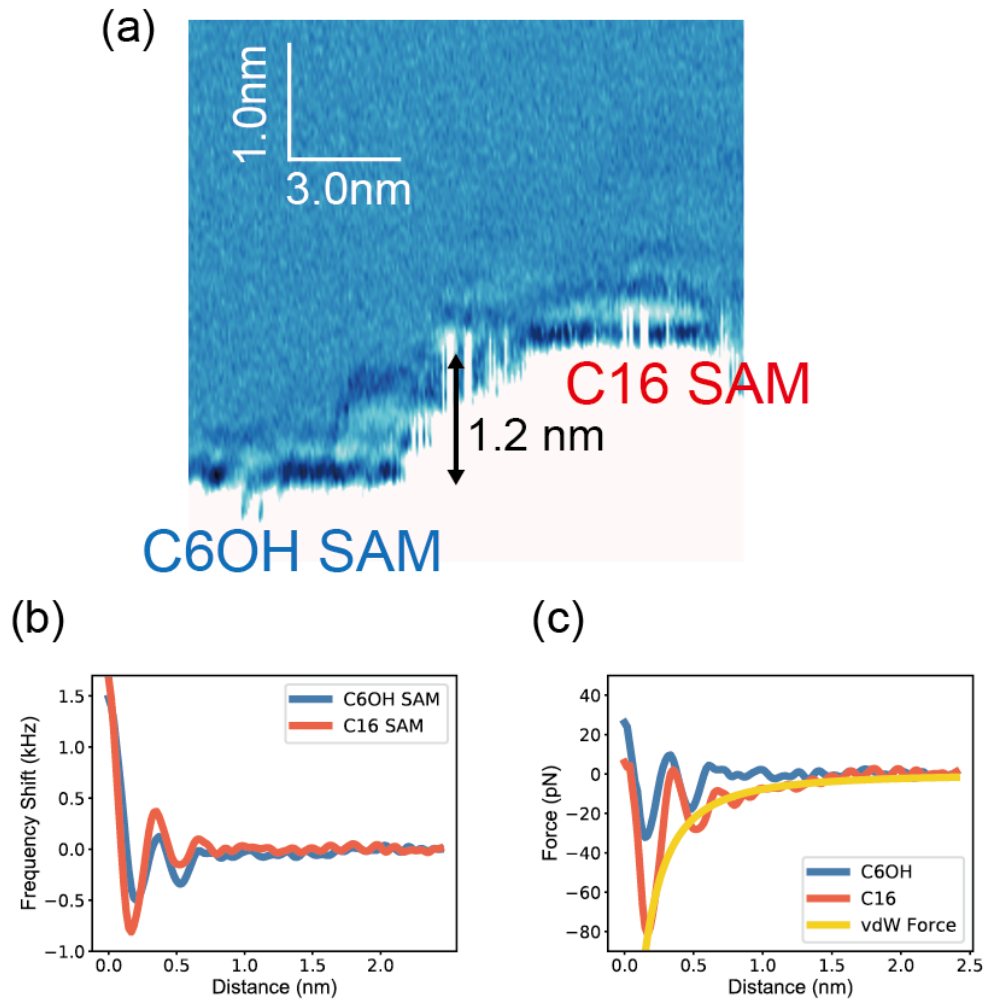


Figure 3.14: (a) 2D frequency shift map obtained over a binary phase separated SAM composed of C6OH and C16 molecules. (b) Frequency shift versus distance curve extracted from (a). The blue and red curves were extracted over the C6OH SAM and the C16 SAM, respectively. (c) Force versus distance curve converted from (b) using the Sader method.⁷⁰⁾ The red and blue curves depict the force curve obtained from the C6OH SAM and C16 SAM, respectively. The yellow curve presents the van der Waals fitting with a Hamaker constant of 9.4×10^{-21} J.

3. HYDRATION STRUCTURES OF HYDROPHILIC AND HYDROPHOBIC SAMs

(STA).^{126, 127)}

$$f(z) = \frac{k_B T}{\rho(z)} \frac{d\rho(z)}{dz} \quad (3.2)$$

Where z is the distance between the tip and the sample, $f(z)$ is the force acting on the tip, $\rho(z)$ is the local water molecule distribution, k_B is the Boltzmann constant and T is the temperature of the system. This formula assumes that the tip is hydrated and the force acting on the tip is equal to the force acting on the water molecule positioned at the apex of the tip. Recently, Miyazawa *et al.* pointed out that a strong repulsive force should act on the tip when $\rho(z)$ is small and its gradient $d\rho(z)/dz$ is large.⁷⁵⁾ This situation occurs at the depletion layer and causes a strong repulsive force to the tip without any contact between the tip and sample. On the other hand, in topographic imaging, a larger amplitude was set during imaging (1.0 nm peak-to-peak) which drives a stronger force to the sample, penetrating the depletion layer and arriving to the SAM surface. This is the reason why the topographic image didn't show a height difference with the molecular model. Therefore, by measuring a 2D frequency shift map and analyzing the force versus distance curve over a binary phase separated SAM, the influence of the depletion layer was elucidated by FM-AFM.

3.6.3 Effect of Contamination on the Hydration Structure of Phase Separated SAMs

The effect of contamination was also found on binary phase separated SAMs. Fig. 3.15 presents a 2D frequency shift map measured over a binary phase separated SAM composed of C2COOH and C16 molecules. The C2COOH and C16 SAM were fabricated by mixing the two alkanethiol molecules in a ratio of 3:1 to 4:1 with a total concentration of 1 μ M. The peculiar features found in section 3.5.4 were also observed in Fig. 3.15; i.e. (i) an oscillation distance of 0.5 nm, (ii) a dip in the frequency shift versus distance curve and (iii) a peak in the dissipation versus distance curve found in the same position of (ii). In addition, the dip in the frequency shift versus distance curve was measured in an arch like pattern above the C16 SAM island. This is because the hydrocarbon contamination gathered to the vicinity of the C16 SAM and formed a hemisphere like structure in

3.6 Measurements of Binary Phase Separated SAMs

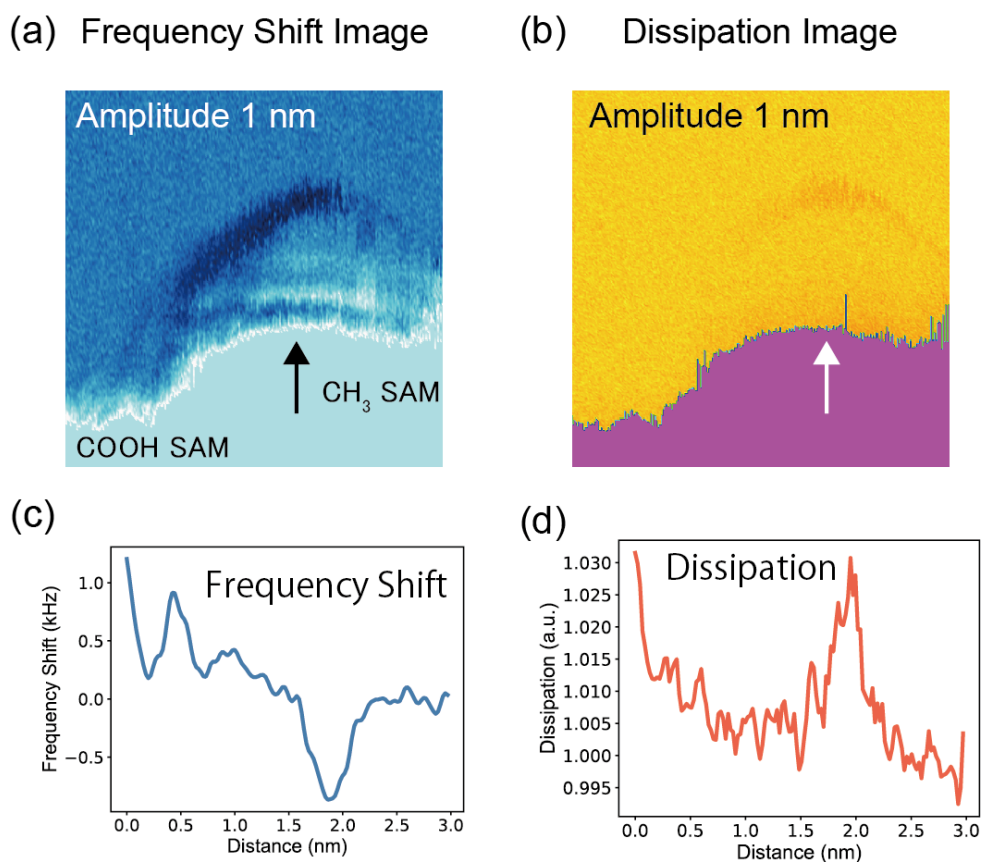


Figure 3.15: (a) 2D frequency shift image obtained over a phase separated SAM composed of C2COOH and C16 molecules. (b) 2D dissipation image simultaneously obtained with the 2D frequency shift map. (c) Frequency shift versus distance curve extracted over the CH₃ SAM in (a). (d) Dissipation versus distance curve extracted over the CH₃ SAM in (b). (c) and (d) were extracted from the same position.

order to minimize the surface area in contact with water. Although the situation is different for a homogeneous hydrophobic sample, from this result it can be hypothesized that a similar phenomenon can occur on a homogeneous hydrophobic sample. The hydrocarbon contaminations form a self-assembled structure to minimize the surface area which causes a frequency shift dip in force mapping measurements.

3. HYDRATION STRUCTURES OF HYDROPHILIC AND HYDROPHOBIC SAMs

3.7 Summary

In this chapter, the hydration structure of hydroxy and methyl terminated alkanethiol SAMs were measured by the 2D force mapping technique using FM-AFM. The hydration structure of hydrophilic SAMs showed dot like patterns, while line patterns appeared on the hydrophobic SAMs. These patterns reflect the locality of the water molecules on the surface. Strange frequency shift versus distance curves were frequently obtained on hydrophobic SAMs which resemble results measured by other research groups. The author suspects the features result from hydrocarbon contamination, since conducting a thorough cleaning process to the cantilever holder was effective. To neglect the tip effect which often causes artifacts in AFM images, the 2D frequency shift map on a binary phase separated SAM which is composed of both hydroxy and methyl terminated alkanethiol molecules were measured. The patterns were the same with the one phase SAMs, which excludes the possibility of tip effects in this investigation. In addition, the influence of the depletion layer on the methyl terminated SAM was found, causing a 0.2 nm height difference from the topographic image. The assumption of the depletion layer was also necessary to fit the force versus distance curves with van der Waals forces.

4

Hydration Structure Measurements on Different Surface Molecular Arrangements of Hydroxy Terminated SAMs

4.1 Introduction

Hydration structures of various substrates have been intensively studied by X-ray/ neutron reflectivity^{35,36)} and SFG,³⁸⁾ but the relationship between the surface and the hydration structures is quite complicated and still not fully understood. The hydration structures result from a competition of two different interactions; i.e., the interaction between water molecules and the surface, and the interaction between the water molecules themselves. Since the former interaction is governed by the electrostatic interactions between the surface charges and dipoles of the water molecules, the arrangement of the water molecules at the interface are determined by the atomic/ionic species of the outermost solid surface. However, since water molecules have a finite volume, the hydration structures are significantly influenced by the atomic-scale arrangement of the surface atoms and ions with respect to the size and shape of the water molecules.⁵¹⁾ Even for an atomically flat surface, the corrugation of the surface atoms may range from ten to several tens of picometers.³⁵⁾ Fig. 4.1 shows a schematic illustration of the atomic

4. HYDRATION STRUCTURE MEASUREMENTS ON DIFFERENT SURFACE MOLECULAR ARRANGEMENTS OF HYDROXY TERMINATED SAMs

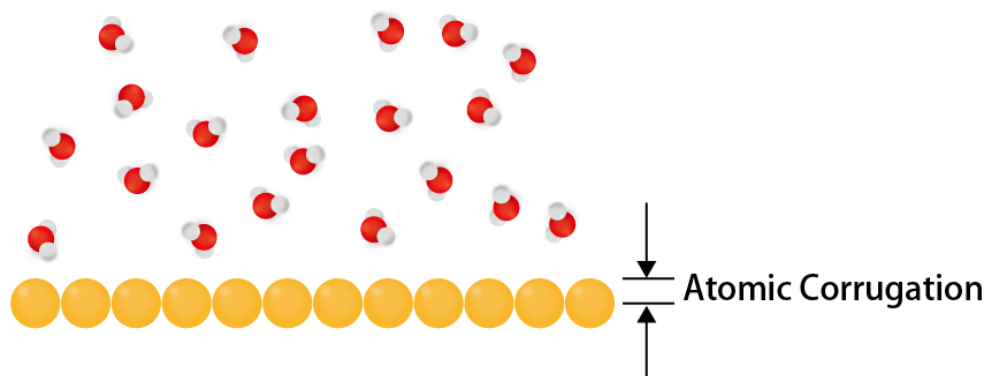


Figure 4.1: Schematic illustration of the impact of atomic corrugation on the hydration structure. An atomically flat surface still has atomic corrugation in the size of a fraction of a water molecule and can effect the total hydration structure.

corrugation of the surface effecting the hydration structure. Although the height difference in the atomic corrugation is very low, they are comparable to a fraction of the size of a single water molecule and large enough to reconstruct the entire hydration structure. Till now, most researches have been conducted on hydrophilic substrates which have functional groups or ions on the surface. Little work has focused on the influence of the topography to the hydration structure.¹²⁸⁾

Alkanethiol SAMs are stabilized by van der Waals forces between the alkane chains, hence the molecular structure of the SAM deeply depends on the alkane chain length. The relationship between the chain length and molecular structure of methyl terminated alkanethiol SAMs are well known. When an adequate amount of thiol molecules are bonded to the surface, alkanethiol SAMs form a closed-packed structure and the molecular arrangements are dominated by two structures, namely the $(\sqrt{3} \times \sqrt{3})R30^\circ$ structure and the $c(4 \times 2)$ superlattice structure. Although the origin of the difference of these two structures are still argued, it is an ideal sample to investigate the relation between the topography and the hydration structure, because the topography of the surface can be altered without changing the chemical composition of the sample. Therefore, there are no extra hydrogen bonds or electrostatic interactions which had to be considered if the surface composition changed and simply concentrate on the surface topography and how it affects the packing structure of the water molecules.

4.2 Molecular Structures of the Alkanethiol SAM

In this chapter, the hydration structures of hydroxyl (-OH) terminated alkanethiol SAMs were investigated using an FM-AFM. Two molecular structures were observed and the hydration structure were measured on both molecular structures using the force mapping technique. The frequency shift versus distance curves were converted to local water molecule distributions and compared with proceeding researches conducting MD simulations on OH terminated alkanethiol SAMs which matched well. By comparing the hydration structure of the two molecular structures, the relationship between the atomic corrugation and the local hydration structure were investigated.

4.2 Molecular Structures of the Alkanethiol SAM

It has long been known that methyl terminated alkanethiol molecules have two molecular structures, namely, the $(\sqrt{3} \times \sqrt{3})R30^\circ$ structure and the $c(4 \times 2)$ superlattice structure. The $(\sqrt{3} \times \sqrt{3})R30^\circ$ structure is a hexagonal structure formed over a Au(111) plane with an intermolecular distance of 0.5 nm. The unit cell is $\sqrt{3}$ times enlarged and rotated 30° against the unit cell of the Au(111) plane. Early studies on the structure of alkanethiol SAMs reported the $(\sqrt{3} \times \sqrt{3})R30^\circ$ structure from transmission electron diffraction^{129,130)} and infrared (IR) spectroscopy¹³¹⁾ However, the presence of a different structure was shown from IR spectroscopy measurements.¹³²⁾ Afterwards, the existence of a larger orthorhombic unit cell was confirmed from helium diffraction¹³³⁾ and STM,⁹³⁾ and the new structure was named the $c(4 \times 2)$ superlattice structure, defined over the hexagonal $(\sqrt{3} \times \sqrt{3})R30^\circ$ structure. The structure is also called the $(3 \times 2\sqrt{3})$ structure, due to the orthorhombic primitive unit cell. Further STM and AFM experiments discovered that the $c(4 \times 2)$ superlattice structure possesses several arrangements.¹³⁴⁾ Fig. 4.2 shows a schematic model of the different arrangements typically found on alkanethiol SAMs. The α - phase depicts the $(\sqrt{3} \times \sqrt{3})R30^\circ$ structure. The β -, γ -, δ -, ϵ - and ζ - phase are different arrangements found in the $c(4 \times 2)$ superlattice structure.¹³²⁻¹⁴¹⁾ The thiol molecules inside the primitive unit cell are known to show several height states which cause the different arrangements.

4. HYDRATION STRUCTURE MEASUREMENTS ON DIFFERENT SURFACE MOLECULAR ARRANGEMENTS OF HYDROXY TERMINATED SAMS

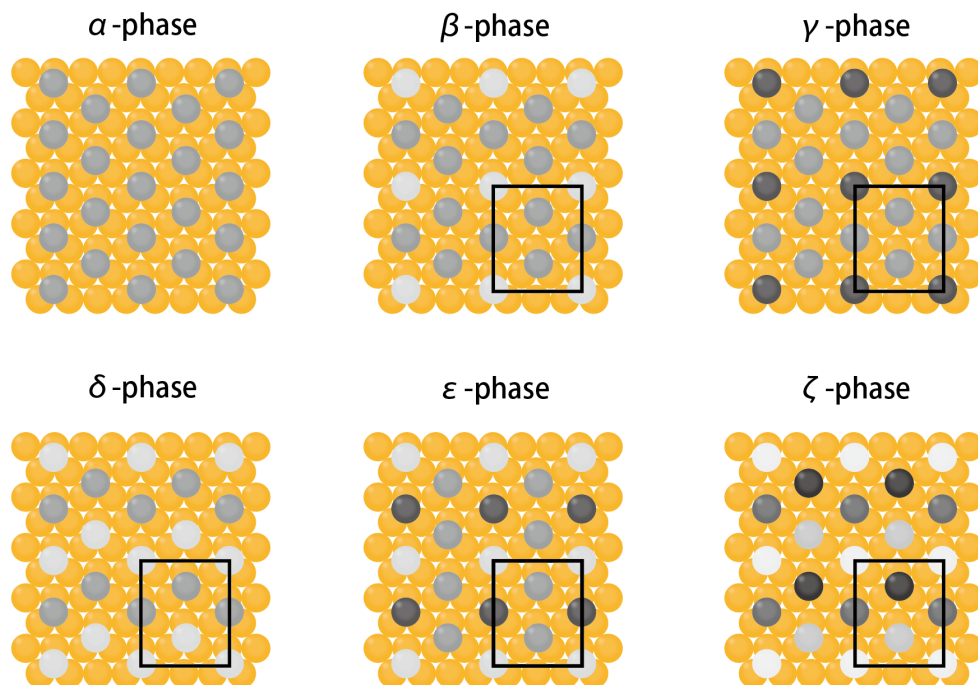


Figure 4.2: Schematic model of the different phases found on alkanethiol SAMs. The yellow circles depict the gold atoms of the Au(111) plane while the black to white circles depict the alkanethiol molecules forming the SAM. The brighter alkanethiol molecules correspond to a higher arrangement than the neighboring molecules. The rectangle in the β -, γ -, δ -, ϵ - and ζ - phase shows the $(3 \times 2\sqrt{3})$ primitive unit cell.

4.2.1 Origin of the different structures in alkanethiol SAMs

Although numerous amounts of research have been conducted to discover the origin of the $(\sqrt{3} \times \sqrt{3})R30^\circ$ and $c(4 \times 2)$ superlattice structure, the issue is yet to be solved. Most researchers now suspect that the interface between the sulfur atom and gold surface is deeply related to these structures. When alkanethiol SAMs were first found, the sulfur atoms were thought to be positioned on the three fold sites on the Au(111) plane. However, this obviously can't explain the height modulation in the $c(4 \times 2)$ superlattice structure and early studies concluded that the structures were derived from different tilt¹³²⁾ or twist angles¹³³⁾ of the alkanethiol molecules. Fenter et al., stated from X-ray diffraction measurements that the $c(4 \times 2)$ superlattice structure derives from the dimerization of the

4.3 Sample Preparation and Experimental Procedures

two neighboring sulfur atoms which form a disulfide moiety.¹⁴⁰⁾ The S-S distance was 2.2 Å, which is shorter than the Au-Au distance on a Au(111) plane (2.8 Å) which alters the binding site of the two alkanethiol molecules forming a disulfide. Later, normal incidence X-ray standing wave measurements disclosed the fact that gold adatoms are included in the gold/sulfur interface.¹⁴²⁾ The presence of the gold adatoms were also confirmed from STM on short chain alkanethiol SAMs and is now strongly believed that a gold adatom is included in the gold/sulfur interface. The existence of the gold adatoms explains the appearance of the etch pits which are necessary to supply gold atoms as adatoms. Etch pits are also found in other organic molecule SAM/metal surface systems where the metal adatoms also appear in the SAM/metal interface.^{100–102)} From density functional theory (DFT) calculations, it was found that two alkanethiol molecules bonding with a single gold adatom is the most energetically favorable model.^{103,104)} In this case, it is thought that the steric hindrance between the neighboring alkanethiol molecules slightly alters the twist angle of the alkane chain and causes the height difference in the unit cell.¹⁴³⁾ However, this model doesn't explain the gold/sulfur interface structure of the $(\sqrt{3} \times \sqrt{3})R30^\circ$ structure and still remains an open question. The most important fact is that the $c(4 \times 2)$ superlattice structure has been measured in various methods, such as helium diffraction,¹³³⁾ low-energy electron diffraction,¹³⁹⁾ grazing incidence X-ray diffraction^{140,141)} and FM-AFM.¹³⁵⁾ Taking into account of these proceeding investigations, the height difference observed in this experiment (Fig. 4.3 (b)) was concluded to actually reflect the "true" topography of the sample and are not caused by the nearest hydration layer above the surface.

4.3 Sample Preparation and Experimental Procedures

The gold films were fabricated as mentioned in section 3.3.2. The gold films were then immersed into ethanol solutions containing alkanethiol molecules with a typical concentration of 10 μM and were heated in a oven at 78°C for more than a day, or kept at room temperature also for more than a day to fabricate

4. HYDRATION STRUCTURE MEASUREMENTS ON DIFFERENT SURFACE MOLECULAR ARRANGEMENTS OF HYDROXY TERMINATED SAMS

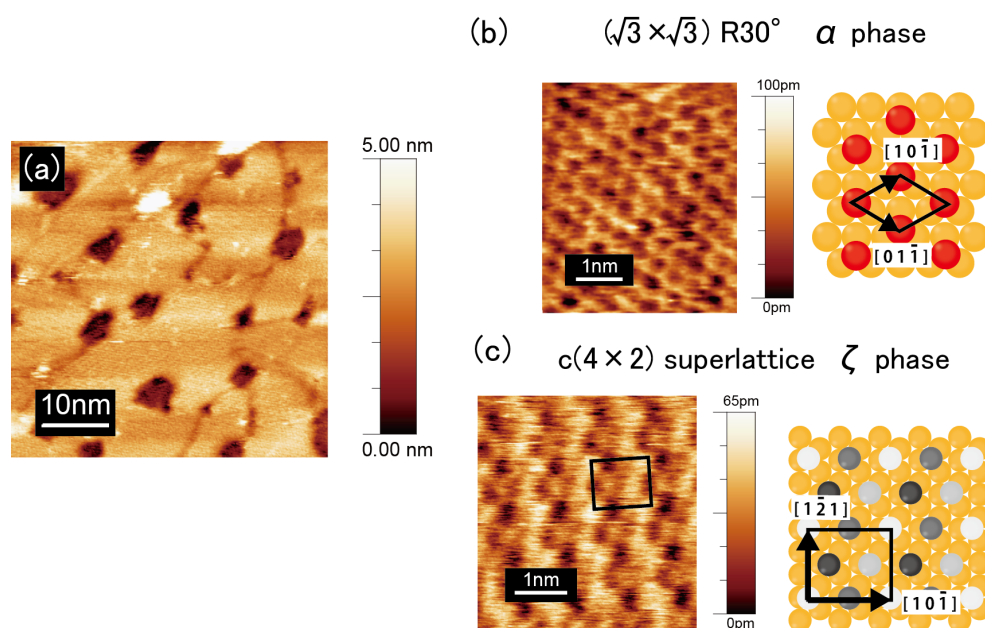


Figure 4.3: (a) Wide view topographic image of a C11OH SAM. (b) A molecular image and a cartoon showing the $(\sqrt{3} \times \sqrt{3}) R30^\circ$ structure. (c) A molecular image and a cartoon showing the $c(4 \times 2)$ superlattice structure.

the alkanethiol SAMs. Heating the sample during SAM fabrication reduced the number of defects and made wide domains.¹⁴⁴⁾ The samples were rinsed with pure ethanol and deionized water and blown in nitrogen gas before observation. Then, the samples were glued to a stainless plate or a teflon cup and mounted on the AFM instrument within 1 hour from air exposure. The measurements were performed in 0.1 M KCl solution to suppress long-range electrostatic forces.²³⁾

Hydration structures were measured by a 2D force mapping technique as mentioned in chapter 2. The frequency shift versus distance curves were converted to force versus distance curves using the Sader method.⁷⁰⁾ 2D force maps were obtained after the topographic images were acquired. The scan direction was rotated to match the desired orientation of the 2D crystal. Data processing was conducted using a free software WSxM¹⁴⁵⁾ or lab made Python programs.

4.4 Topography of the C11OH SAM

4.4.1 Molecular Structure of C11OH SAMs

Fig. 4.3 (a) shows a wide view topographic image of the C11OH SAM. As mentioned in chapter 3, etch pits and domain boundaries can be observed in the image which are typically found in alkanethiol SAMs.⁸⁷⁾ Fig. 4.3 (b) and (c) show the molecular image of the C11OH SAM. The hexagonal structure shown in Fig. 4.3 (b) derives from the $(\sqrt{3} \times \sqrt{3})R30^\circ$ structure. On the other hand, as depicted in Fig. 4.2, some molecular images showed a "zig-zag" like pattern or a rectangular pattern which are known to derive from the $c(4 \times 2)$ superlattice structure.¹³⁵⁾ Fig. 4.3 (c) shows the molecular image which the force mapping technique was conducted in this study. Four height states can be recognized which strongly resembles the ζ - phase of the $c(4 \times 2)$ superlattice structure.¹³⁷⁾ The $c(4 \times 2)$ superlattice structure has also been reported on hydroxyl-terminated alkanethiol SAMs using electrochemical scanning tunneling microscopy (EC-STM)^{146,147)} or FM-AFM in aqueous conditions^{148,149)}. The maximum height difference was around 50 pm which matches the order of proceeding STM investigations on methyl and hydroxyl terminated alkanethiol SAMs.^{136,150)}

4.4.2 Influence of Temperature on C11OH SAMs

Figs. 4.4 (a) and (b) show a $100 \times 100 \text{ nm}^2$ size topographic image of a C11OH SAM fabricated by immersing the sample in room temperature and in 70°C , respectively. As in Fig. 4.3 (a), etch pits and domain boundaries can be recognized in both samples but there were many more etch pits in the sample fabricated in room temperature. Plus, the area of the etch pits fabricated in 70° were larger than fabricated in room temperature. Therefore, heating the sample during immersion decreased the number of defects and etch pits and also enlarged the area of each etch pit. Yamada reported the same trend on ex-situ STM measurements on 1-decanethiol SAMs and suggested a Ostwald ripening growth process of the etch pits.¹⁵¹⁾ Ostwald ripening is a growth mechanism usually applied to nanoparticles.¹⁵²⁾ The stability of nanoparticles depend on its size and when two nanoparticles exist in a solution, the atoms consisting the smaller nanoparticle

4. HYDRATION STRUCTURE MEASUREMENTS ON DIFFERENT SURFACE MOLECULAR ARRANGEMENTS OF HYDROXY TERMINATED SAMS

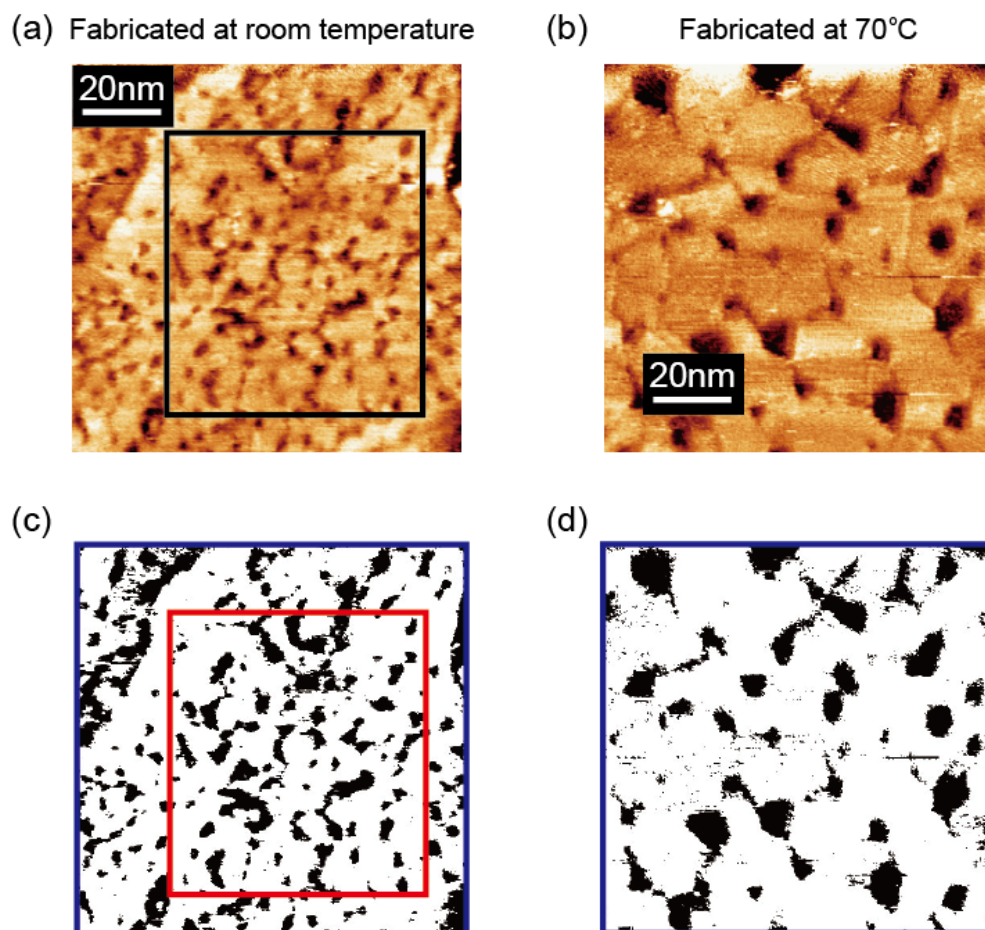


Figure 4.4: $100 \times 100 \text{ nm}^2$ size topographic image of a C11OH SAM fabricated at (a) room temperature and (b) 70° . The black rectangle in (a) displays the area where the etch pits analysis was conducted. (c) and (d) are the binary images of (a) and (b), respectively, which were used in the analysis. The red rectangle in (c) shows the same area of the black rectangle in (a).

transfer to the larger nanoparticle. When the process finishes, the number of the nanoparticles decrease and only large nanoparticles exist. Yamada et al. suggested that the same phenomenon occurred to the etch pits on the alkanethiol SAM. For proof, they showed that the ratio of the area of the etch pits were constant and independent of the immersion temperature. In this experiment, the ratio of the etch pits were analyzed by a free software, ImageJ.¹⁵³⁾ Since steps existed in Fig. 4.4 (a), the ratio of the etch pits were analyzed in the area inside

4.4 Topography of the C11OH SAM

the black rectangle in Fig. 4.4 (a). Figs. 4.4 (c) and (d) displays the binary image used in analyzing the etch pits. The black regions depicts the area which are counted as etch pits. From the analyses, the ratio of the etch pits was 20% in the sample fabricated in room temperature while the ratio was 16% in the 70°C fabricated sample. If the $c(4 \times 2)$ superlattice structure derives from the complex RS-Au(adatom)-SR moiety mentioned earlier, and the adatoms were only supplied from etch pits, the coverage ratio of the Au adatoms on a $c(4 \times 2)$ superlattice structure SAM would be 16%, which matches well with the ratio of Fig. 4.4 (b).¹⁵⁴⁾ The difference of the etch pit ratio in the sample fabricated in room temperature may be due to statistical error, contribution of RS-Au(adatom) moieties in the $(3 \times 2\sqrt{3})$ structure^{155,156)} or adatom diffusion from steps.¹⁵⁴⁾ In AFM measurements, practically, it's impossible to eliminate thermal drift in the apparatus and therefore, it's desirable to use SAMs with larger domains.

Although SAMs fabricated in 70°C were suitable for the hydration structure measurements, the $(\sqrt{3} \times \sqrt{3})R30^\circ$ structure wasn't observed in this method. On C16 SAMs, annealing has been reported to increase the coverage area of the $c(4 \times 2)$ superlattice structure,¹⁵⁷⁾ which is consistent with this study. Therefore, the $(\sqrt{3} \times \sqrt{3})R30^\circ$ structure was imaged by fabricating the SAMs at room temperature while the SAMs with the $c(4 \times 2)$ superlattice structure were fabricated at 70°C.

4.4.2.1 Fluctuation of the Molecular Structure in the C6OH SAM

Although X-ray experiments, STM observations and DFT calculations have presented numerous results that the $c(4 \times 2)$ superlattice structure derives from the complex gold/sulfur interface,^{103,104,142,158,159)} there are still contrary opinions that the structures are due to artifacts. For example, some believe STM observations are measuring the difference of the electrical tunneling current of the alkanethiol SAMs and not the true sample surface. In this study, the molecular structure sometimes altered from the $(\sqrt{3} \times \sqrt{3})R30^\circ$ structure to the $c(4 \times 2)$ superlattice structure, or vice versa when imaging the same location. Fig. 4.5 displays two topographic images taken over a C6OH SAM. Fig. 4.5 (b) was imaged 50 seconds later than Fig. 4.5 (a) and both images were scanned from

4. HYDRATION STRUCTURE MEASUREMENTS ON DIFFERENT SURFACE MOLECULAR ARRANGEMENTS OF HYDROXY TERMINATED SAMS

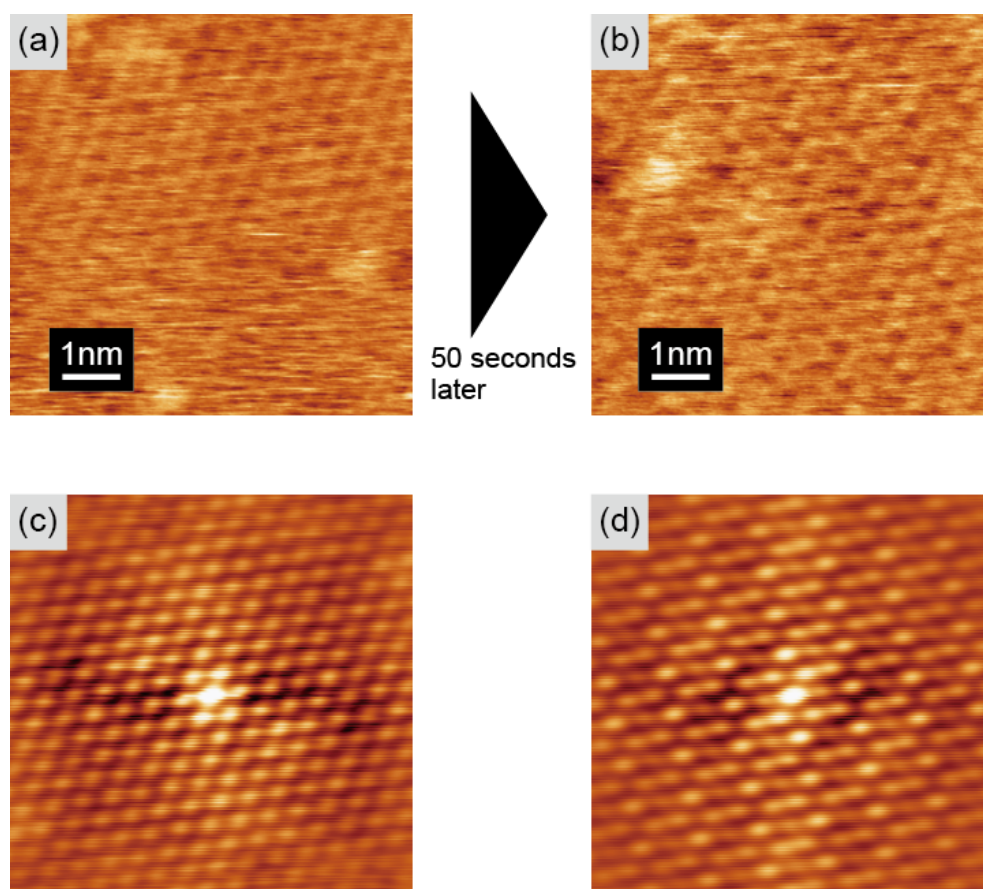


Figure 4.5: (a) and (b) are narrow view topographic images taken over a C6OH SAM. (b) was obtained about 50 seconds after (a) was achieved. (c) and (d) depicts the self-correlation image of (a) and (b), respectively.

down to up. It can be seen that the $(\sqrt{3} \times \sqrt{3})R30^\circ$ structure changed to the $c(4 \times 2)$ superlattice structure during the scan. Fig. 4.5 (c) and (d) are the 2D self-correlation images of the two topographic images (a) and (b), respectively. The self-correlation images confirm that the imaged molecular structure altered during the scan. The structure fluctuation has been reported early STM measurements on methyl terminated alkanethiol SAMs in ultra-high vacuum environments.¹³⁸ They have been thought to be due to the change in the "true" surface or artifacts due to tip changes or the electric potential of the STM. It is hard to discuss the origin of this phenomenon but it's interesting that this was found in an AFM measurement, since the electrical potential can be ruled out. Also, tip changes

4.5 Hydration Structure of the alkanethiol SAM

are believed to instantaneously disrupt the images which was not observed in this data set. Thus, it seems that the "true" surface arrangement varied during the scan, although further investigations should be conducted to draw any conclusion. This means that the energetic stability between the two structures are small which can be also confirmed by the fact that these two structures coexist on the SAM.¹⁶⁰⁾ In either case, the molecular structure of the 2D frequency shift maps were confirmed by checking the period of the corrugation of the surface.

4.5 Hydration Structure of the alkanethiol SAM

4.5.1 Frequency Shift Maps of the C11OH SAM

Fig. 4.6(a) and (b) show a frequency shift image taken over the ($\sqrt{3} \times \sqrt{3}$)R30° structure and the $c(4 \times 2)$ superlattice structure, respectively. In the force mapping technique, when the frequency shift exceeds the threshold the tip retracts, so there are no data points in the bottom part of the picture (white area) and the boundary indicated by the yellow line reflects the topography of the surface. Protrusions and valleys can be found in the image which are depicted by red and blue arrows, respectively. The protrusions and valleys found in Fig. 4.6 reflect the morphology of the C11OH SAM. Above the surface, bright and dark spots can be found in the images which indicate the positive or negative frequency shift of the cantilever from the resonance frequency. Figs. 4.6(c) and (d) illustrate the relationship between the slow scan direction of the tip and the SAM surface. Fig. 4.6 (a) and (b) were taken both taken along the $[1\ 0\ \bar{1}]$ direction. Fig. 4.7 (a) and (b) show the frequency shift versus distance curve extracted from Fig. 4.6 (a) and (b). The frequency shift versus distance curve over the protrusion of both structures were shifted to adjust the height difference found in the 2D frequency shift image, which includes the "true" surface and slight indentation caused by the force mapping technique. The frequency shift versus distance curves over the protrusions and valleys were completely different, where an oscillation occurred near to the surface over the valley in both structures. The period of the oscillation was around 0.3 nm which matches the size of a single water molecule. Fig. 4.7 (c) and (d) are force versus distance curve converted from the frequency shift versus

4. HYDRATION STRUCTURE MEASUREMENTS ON DIFFERENT SURFACE MOLECULAR ARRANGEMENTS OF HYDROXY TERMINATED SAMS

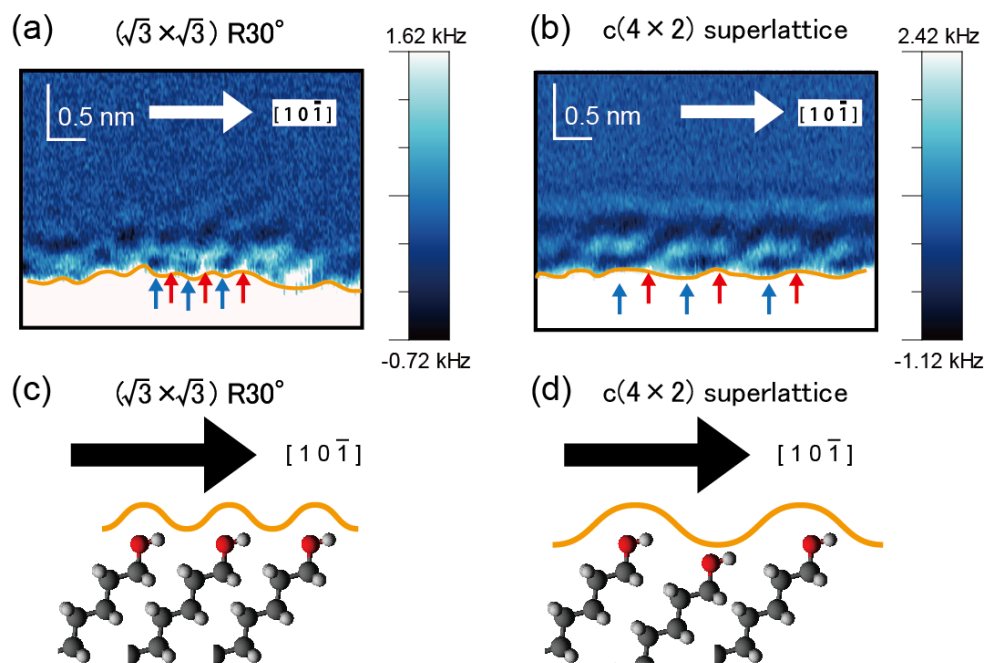


Figure 4.6: Frequency shift image taken over a C11OH SAM. The frequency shift maps were taken over the (a) $(\sqrt{3} \times \sqrt{3})R30^\circ$ structure along the $[1\ 0\ \bar{1}]$ direction and (b) $c(4 \times 2)$ superlattice structure along the $[1\ \bar{2}\ 1]$ direction. The orange line is a guide to the eye of the topography of the surface. The arrows indicate the points where the frequency shift versus distance curves were averaged and plotted in Fig. 4.7 (a) and (b). A schematic summary of the force mapping technique conducted on (c) $(\sqrt{3} \times \sqrt{3})R30^\circ$ structure and (d) the $c(4 \times 2)$ superlattice structure.

distance curves using the Sader method. Although it's not easy to determine whether the tip retracts at the "true" surface in the force mapping technique, it was decided that in this study, the tip reaches the sample and doesn't stop on the hydration layer above it. In fact, the threshold of the frequency shift was set higher than previous FM-AFM studies on alkanethiol SAMs.^{148,149} Hence, the values that were higher than 1 kHz in the frequency shift curve were cut off. The force curves (Fig. 4.7 (c) and (d)) and water molecule distributions (explained afterwards, Fig. 4.7 (e) and (f)) are displayed in the range where the frequency shift doesn't exceed 1 kHz.

A remarkable difference was recognized between the hydration structures of the $(\sqrt{3} \times \sqrt{3})R30^\circ$ structure and the $c(4 \times 2)$ superlattice structure. The

4.5 Hydration Structure of the alkanethiol SAM

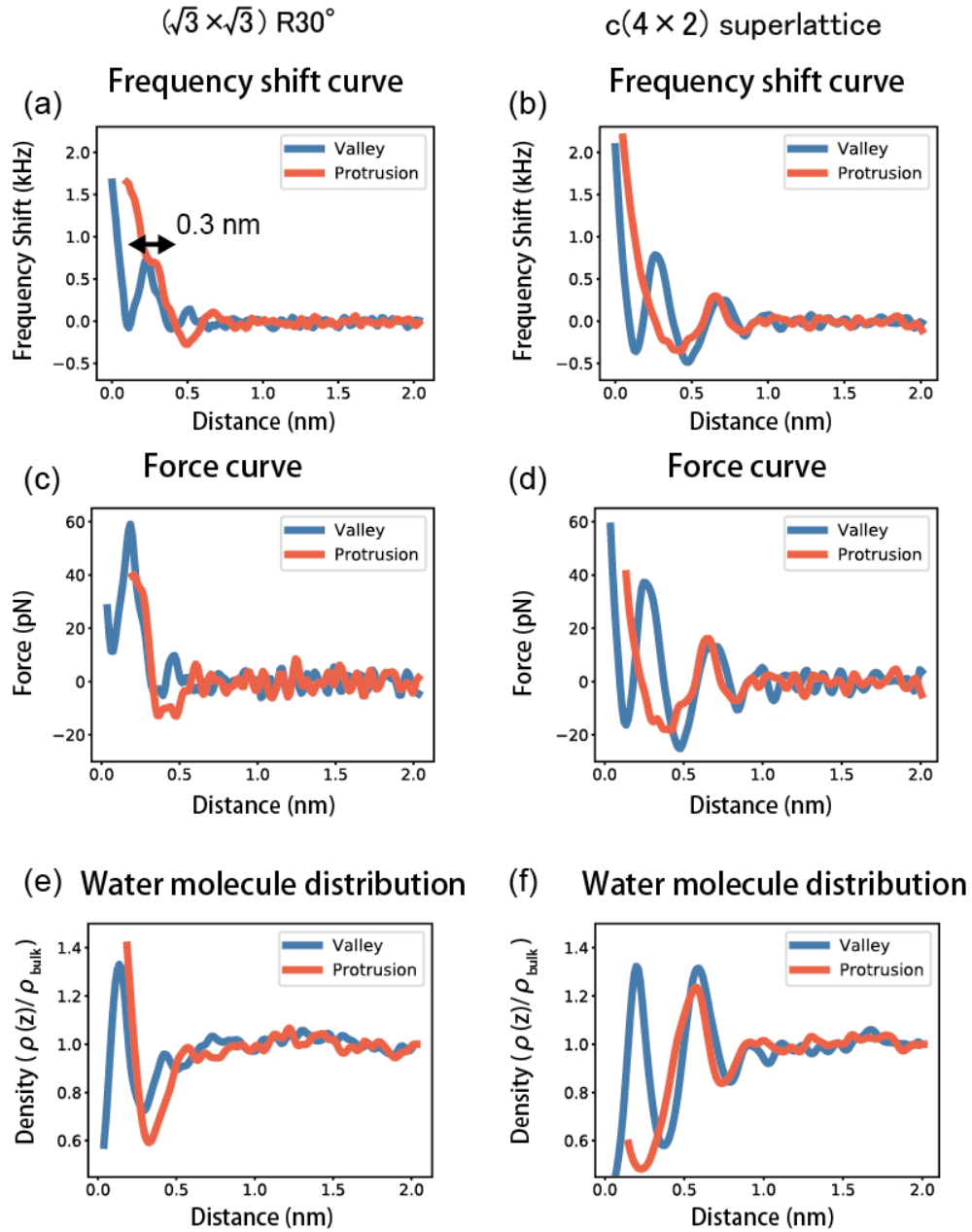


Figure 4.7: (a), (b) Frequency shift versus distance curves extracted from Fig. 4.6(a) and (b), respectively. Each point was averaged from three different points depicted by the arrows. (c), (d) are force versus distance curves converted from (a) and (b), respectively, using the Sader method.⁷⁰ (e), (f) Local water molecule density obtained using equation 4.2 calculated from (c) and (d), respectively.

4. HYDRATION STRUCTURE MEASUREMENTS ON DIFFERENT SURFACE MOLECULAR ARRANGEMENTS OF HYDROXY TERMINATED SAMS

biggest difference was the distance between the dark spots found over the protrusions (depicted in blue arrows) was 0.5 in Fig. 4.6 (a) and 1.0 nm in Fig. 4.6 (b). 1.0 nm doesn't match with the distance of the nearest neighbors in the $c(4 \times 2)$ superlattice structure. The distance actually corresponds to the distance between the molecules with the same height when the scan was in the $[1 \bar{2} 1]$ direction of the $c(4 \times 2)$ superlattice structure. Based on these results, it is possible to describe a consistent explanation of how the topography of the surface affects the hydration structure. In the $(\sqrt{3} \times \sqrt{3})R30^\circ$ structure, all of the molecules are on the same plane and the distance between the molecules are 0.5 nm. This is longer than the diameter of a single water molecule which is 0.28 nm and the water molecules have enough space to position itself between the thiol molecules. In the $c(4 \times 2)$ superlattice structure, the distance between the nearest neighbors are still 0.5 nm, but hydroxyl groups are not on the same plane and have a height difference around 50 pm as mentioned above. In this case, the space over the lower thiol molecules suit better for the water molecules and are positioned over the lower hydroxyl groups in the $c(4 \times 2)$ superlattice structure. Therefore, the periodicity and the amplitude of the corrugation alters the hydration structure and is strong evidence that the topography is a huge factor of the hydration structure. This is quite surprising since the height difference in the $c(4 \times 2)$ superlattice structure measured in this study was around 50 pm, which is only about 15% of the size of a single water molecule. The effect of the topography to the hydration structure also explains well why the hydration structure of ζ phase $c(4 \times 2)$ superlattice structure alters with the ϵ phase $c(4 \times 2)$ superlattice structure previously reported.

Some papers have already reported the 2D frequency shift images of OH-terminated alkanethiol SAMs. Hiasa *et al.*, investigated the hydration structure of C11OH and C6OH SAMs using FM-AFM.^{148,149} The C11OH SAM showed a $(\sqrt{3} \times \sqrt{3})R30^\circ$ structure and the frequency shift oscillation was found over the valleys of the frequency shift map, which is consistent with this study. However, the C6OH SAM showed a $c(4 \times 2)$ superlattice structure and the oscillation appeared on the protrusion which disagrees with this study. It is hard to say what caused these differences, but maybe the chain length or phase of the two SAMs are the reasons. The molecular structure of the C11OH SAM in this study

4.5 Hydration Structure of the alkanethiol SAM

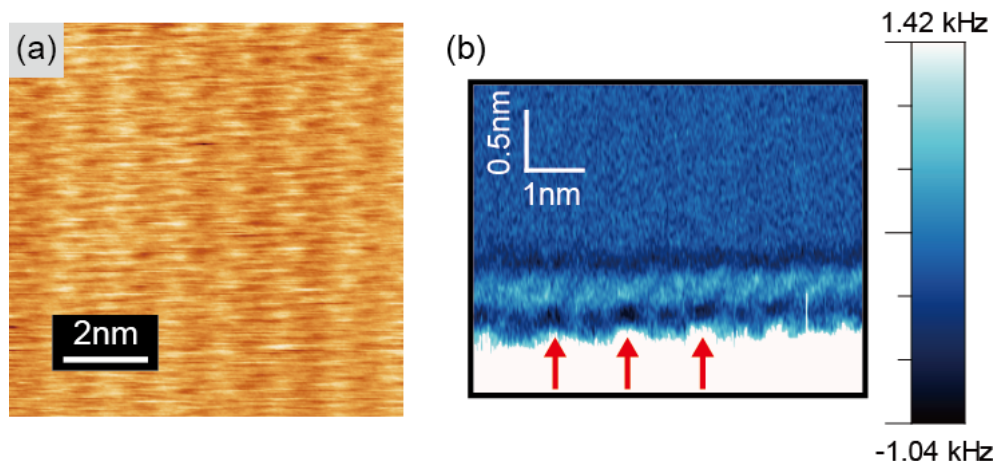


Figure 4.8: (a) Molecular-scale topographic image and (b) 2D frequency shift map of the $c(4 \times 2)$ superlattice structure formed on a C6OH SAM. The red arrows depicts the protrusions where the frequency shift oscillation was found.

closely resembles the ζ -phase while the molecular structure of the C6OH SAM in the previous investigation suggested an ϵ -phase-like structure. The effect of the molecular arrangements on the hydration structure as already mentioned also explains why the hydration structures of the ζ -phase $c(4 \times 2)$ superlattice structure were different from that of the previously reported ϵ -phase $c(4 \times 2)$ superlattice structure. Figs. 4.8(a), (b) depict the topographic image and 2D frequency shift map taken over a C6OH SAM, respectively. Although the phase of the SAM were not able to be defined, the 2D frequency shift map depicts that the frequency shift oscillation appears on the protrusions, which agrees with the previous study.¹⁴⁹⁾

4.5.2 Details of Calculating the Local Water Molecule Distribution from Force Versus Distance Curves

As mentioned in section 2.4, the interpretation of 2D frequency shift maps is still a difficult problem. Assuming the STA is one approach where the tip is assumed to be hydrated and a water molecule is positioned in front of the tip apex^{126,127)} (see also section 3.6) In the STA, the force versus distance curves and the local

4. HYDRATION STRUCTURE MEASUREMENTS ON DIFFERENT SURFACE MOLECULAR ARRANGEMENTS OF HYDROXY TERMINATED SAMS

water molecule distribution are related as expressed in eq. 3.2.^{126,127)}

$$f(z) = \frac{k_B T}{\rho(z)} \frac{d\rho(z)}{dz} \quad (4.1)$$

Where z is the distance between the tip and the sample, $f(z)$ is the force acting on the tip, $\rho(z)$ is the local water molecule distribution, k_B is the Boltzmann constant and T is the temperature of the system. By integrating and taking the exponential function of both sides, $\rho(z)$ can be obtained by the following equation.

$$\rho(z) = \exp\left(\frac{\int f(z) dz}{k_B T}\right) \quad (4.2)$$

Empirically, force versus distance curves obtained by FM-AFM are known to monotonically increase when approaching the surface other than oscillation forces,^{75,76)} which act as the background. Hence, the force versus distance curves were fitted using the following formula.⁷⁶⁾

$$f(z) = 2\pi R \left\{ A_o \cos\left[\frac{2\pi(z + \varphi)}{\sigma_o}\right] \exp\left(-\frac{z}{\lambda_o}\right) + A_m \exp\left(-\frac{z}{\lambda_m}\right) \right\} \quad (4.3)$$

Where R is the tip radius, A_o and A_m are the magnitudes of the oscillation and monotonic repulsion forces, φ is the phase shift adjusting the start point of the circular function, σ_o is the distance between the oscillations, λ_o and λ_m are the decay lengths of the oscillation and monotonic repulsion forces. The monotonic increase was defined as the short range background and subtracted it from the force converted from the Sader method.⁷⁵⁾ Then, recording to eq. 4.2, the force versus distance curves were integrated by applying the trapezoidal rule and took the exponential function to obtain the local water molecule distribution.

From here, the water molecule distribution conversion process of the frequency shift versus distance curves extracted from the $(\sqrt{3} \times \sqrt{3})R30^\circ$ structure is demonstrated. Fig. 4.9 (a) and (b) show the force versus distance curve and the fitting curve using eq. 4.3 taken over the valley and protrusion, respectively. The fitting agreed fairly well with the experimental curve and shows eq. 4.3 is a good formula to describe hydration forces. The arrows in the figure are the peaks due to hydration forces.

The monotonic repulsion force was assumed as a background force other than hydration forces, where the same assumptions have been done in previous

4.5 Hydration Structure of the alkanethiol SAM

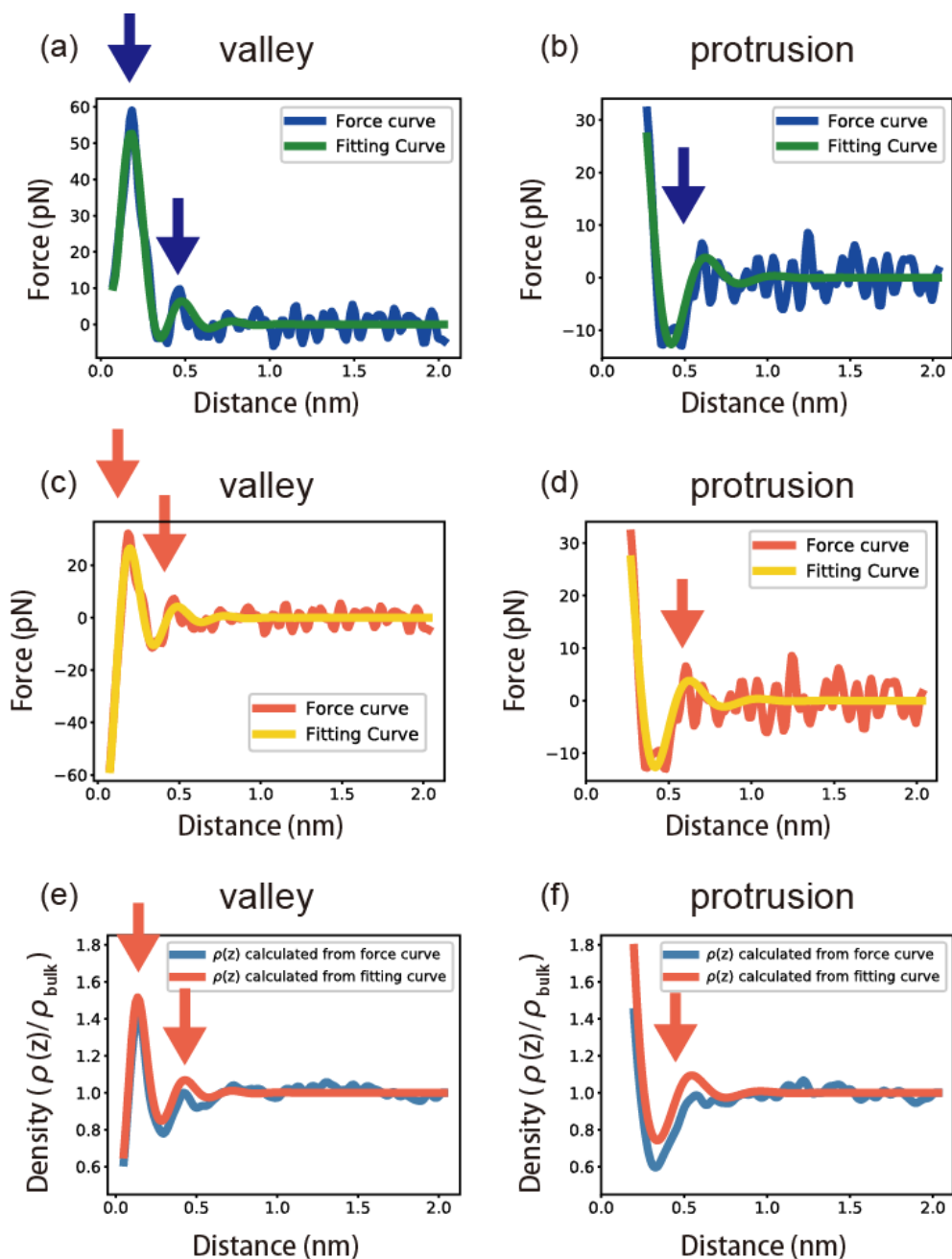


Figure 4.9: The blue curves in (a) and (b) show the force versus distance curve converted from the frequency shift versus distance curves displayed in Fig. 4.7 (a). The green curves in (a) and (b) depicts the fitting curve of eq. 4.3. (c) and (d) show the monotonic component subtracted from the force versus distance curve and the fitting curve of eq. 4.3.

4. HYDRATION STRUCTURE MEASUREMENTS ON DIFFERENT SURFACE MOLECULAR ARRANGEMENTS OF HYDROXY TERMINATED SAMS

reports.⁷⁵⁾ Figs. 4.9 (c) and (d) show the force versus distance curve subtracting the monotonic repulsion force and the oscillation component of the fitting curve. Two oscillation peaks in the force versus distance curve can be seen which are represented by the arrows.

Then, the force curves were integrated by the trapezoidal rule following eq. 4.2. Fig. 4.9 (e) and (f) show the local water molecule distribution obtained by the integration process. On the valley, although the second peak is small in the local water molecule distribution, it can be confirmed in Fig. 4.9 (a)-(d), so the second peak should be due to hydration forces and is hence not due to noise. The shoulder indicated by the dashed arrow in Fig. 4.9 (b) is converted to a large peak in Fig. 4.9 (d) which overestimates the local water molecule distribution.

The fitting parameters used in fitting eq. 4.3 are showed on Tab. 4.1. From Table 4.1 it is clear that the magnitude of the monotonic component is larger and the decay length is shorter on the protrusions of both structures than on valleys. The problem in this fitting method is that when the oscillation force doesn't occur near the surface and only a monotonic increase appears, the fitting formula can't distinguish a monotonic increase and a strong oscillation. This happened on protrusions in this study since the water molecules absorb on valleys than on protrusions. Therefore, the monotonic increase in local water molecule distribution over protrusions are inevitable in this study.

Finally, the calculated local water molecule distributions were compared the results obtained from MD simulations. Fig. 4.10 shows the local water molecule distribution calculated by the force curve and obtained from ref ¹¹²⁾. Since the MD simulation was conducted on a $(\sqrt{3} \times \sqrt{3})R30^\circ$ structure and was converted to 1-dimension, the force versus distance curve was averaged over the valley and protrusion and calculated the local water molecule distribution using eq. 4.2. The two curves matched well and shows that the STA is a good assumption to obtain local water molecule distributions, experimentally. Fig. 4.11 presents the schematic image of the hydration structure formed on the $(\sqrt{3} \times \sqrt{3})R30^\circ$ structure and on the $c(4 \times 2)$ superlattice structure. This study demonstrates that the force mapping technique is a powerful method to achieve information of hydration structures on hydrophilic substrates.

4.5 Hydration Structure of the alkanethiol SAM

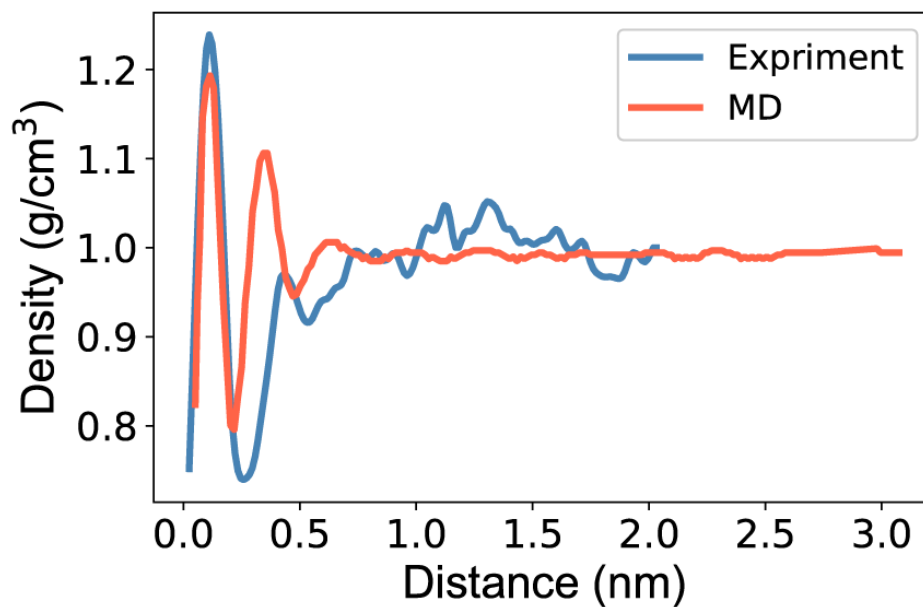


Figure 4.10: Local water molecule distribution calculated from experimental force versus distance curves and obtained from MD simulations.¹¹²⁾

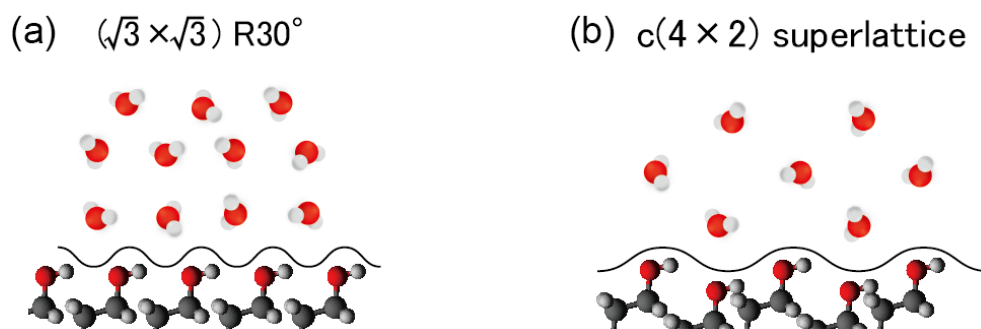


Figure 4.11: Schematic illustration of the hydration structure formed on (a) $(\sqrt{3} \times \sqrt{3}) R30^\circ$ structure and (b) $c(4 \times 2)$ superlattice structure, respectively.

4. HYDRATION STRUCTURE MEASUREMENTS ON DIFFERENT SURFACE MOLECULAR ARRANGEMENTS OF HYDROXY TERMINATED SAMS

Table 4.1: Fitting parameters of the force versus distance curves

	A_o (pN)	λ_o (Å)	φ (Å)	σ_o (Å)	A_m (pN)	λ_m (Å)
$(\sqrt{3} \times \sqrt{3})R30^\circ$ valley	73	1.9	0.90	3.0	100	1.3
$(\sqrt{3} \times \sqrt{3})R30^\circ$ protrusion	110	2.0	2.0	4.3	1000	0.43
$c(4 \times 2)$ valley	59	4.3	0.78	3.7	110	0.95
$c(4 \times 2)$ protrusion	55	3.3	5.1	5.9	240	0.44

4.5.3 Benefits of the Local Water Molecule Distribution Calculation

Fig. 4.7 (e) and (f) show the local water molecule distribution following the procedures mentioned above. As been expected from the frequency shift versus distance curves, the local water molecule distribution differed over the protrusions and valleys for both structures where the peak was positioned near the surface on the valley than on the protrusion for both molecular structures. In both structures, a peak in the local water molecule distribution appeared at the minimum value of an oscillation in the frequency shift versus distance curve. Although further investigation is required, this may mean that water molecules are positioned at the dark spots in the 2D and 3D frequency shift images. This has a huge impact on interpreting frequency shift images, where it's almost impossible to see the position of the water molecules experimentally. This is significant when measuring hydration structures of biomolecules, where the cost is too expensive to conduct MD simulations on biomolecules. The STA reinforces the FM-AFM as a more powerful tool to investigate hydration structures on complicated biomolecules.

4.6 Hydration Structure Measurements at the Vicinity of an Etch Pit on C16OH SAMs

$c(4 \times 2)$ superlattice δ -phase

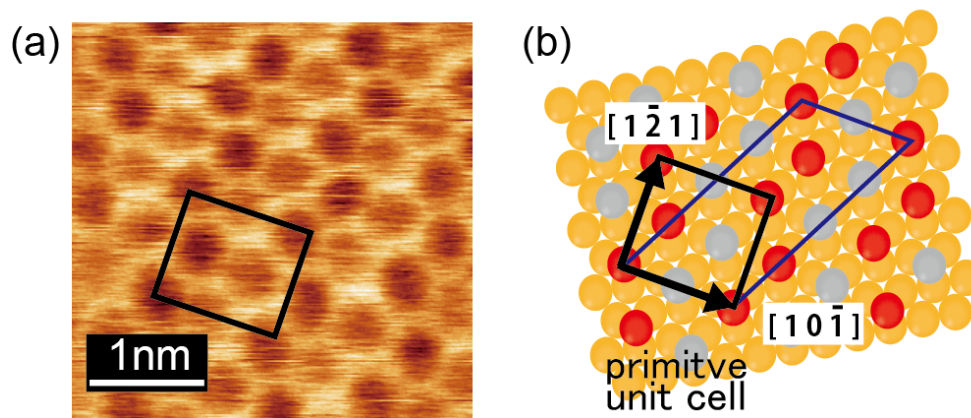


Figure 4.12: (a) Typical narrow view topographic image of the C16OH SAM. The black rectangle depicts the primitive unit cell of the $c(4 \times 2)$ superlattice structure. (b) Schematic model of the δ - phase of the $c(4 \times 2)$ superlattice structure. The red and gray spheres present the low and high C16OH molecules, respectively.

4.6 Hydration Structure Measurements at the Vicinity of an Etch Pit on C16OH SAMs

The hydration structure at the vicinity of etch pits on a C16OH SAM were measured by the force mapping technique. Fig. 4.12 presents the narrow view image of the C16OH SAM. The topographic image showed a "zig-zag" pattern which resembles the δ - phase of the $c(4 \times 2)$ superlattice structure. The molecular structure in the C6OH SAM, C11OH SAM and C16OH SAM all formed the $c(4 \times 2)$ superlattice structure. This is apart from methyl terminated alkanethiol SAMs where the $(\sqrt{3} \times \sqrt{3})R30^\circ$ structure is more dominant in long chain alkanethiol SAMs such as C16 SAMS. Thus, these results shows that the interaction between the functional groups alters the overall surface arrangements of the alkanethiol SAM.

Fig. 4.13(a) displays a topographic image of obtained over a C16OH SAM. The hexagonal low region found in the left hand side in Fig. 4.13(a) was 0.25 nm low than the global plane and is an etch pit. Fig. 4.13(b) shows a 2D frequency shift map achieved over the boundary of the etch pit. A dot like pattern was

4. HYDRATION STRUCTURE MEASUREMENTS ON DIFFERENT SURFACE MOLECULAR ARRANGEMENTS OF HYDROXY TERMINATED SAMS

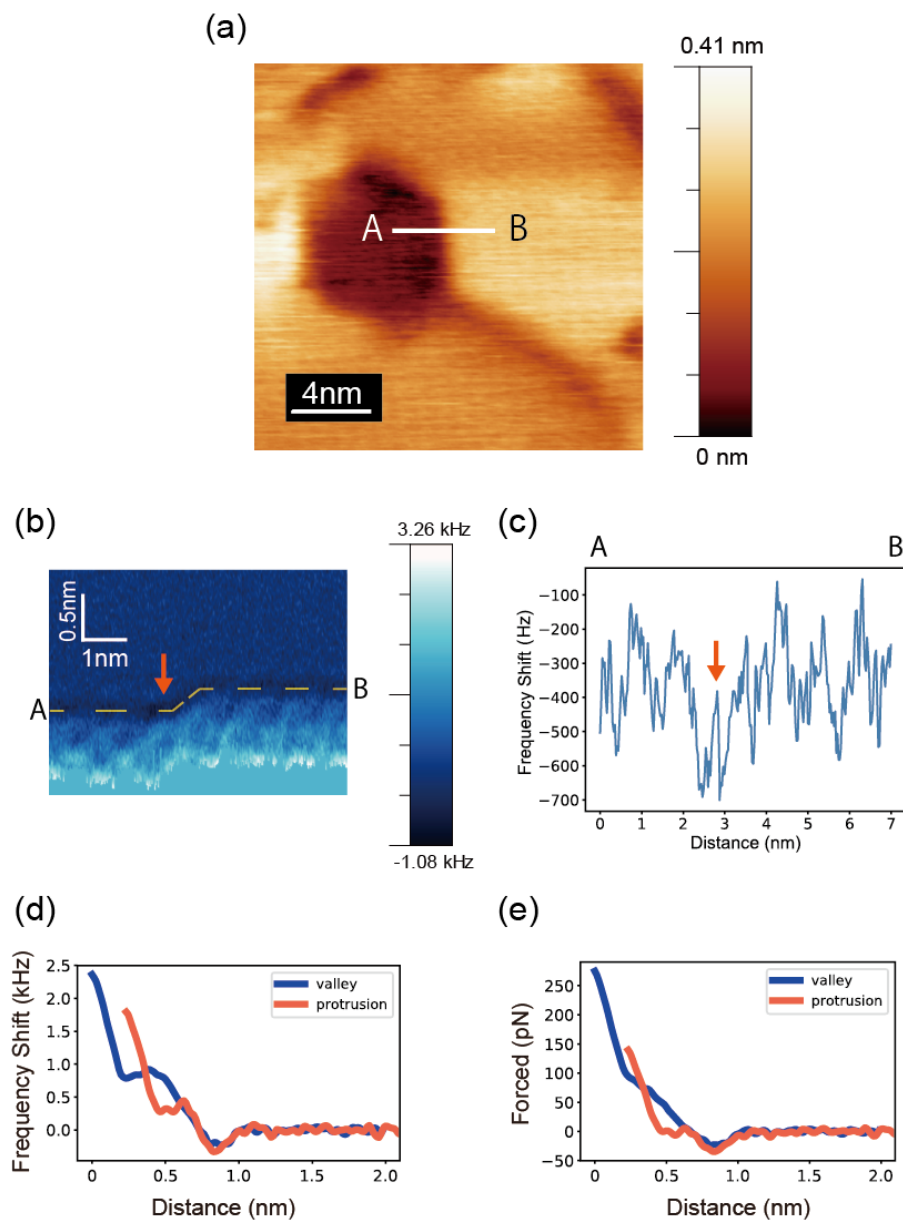


Figure 4.13: (a) Topographic image of an etch pit on a C16OH SAM. (b) 2D frequency shift map measured crossing the boundary of the etch pit. (c) Profile of the frequency shift depicted in the orange broken line in (b). (d) Frequency shift curves extracted from (b). (e) Force versus distance curves converted from (d) using the Sader method.⁷⁰⁾ The blue and red lines in (d) and (e) depict the curves obtained over the valleys and protrusions of the C16OH SAM.

4.6 Hydration Structure Measurements at the Vicinity of an Etch Pit on C16OH SAMs

observed which was similar to the hydration structure measured on C6OH and C11OH SAMs, indicating an inhomogeneous distribution of water molecules in the in-plane direction. Also a dark area was found about 0.6 nm above the surface. Fig. 4.13(c) presents a profile which is depicted with the polygonal broken line in Fig. 4.13(b). A dip in the frequency shift was found at the position pointed out with the orange arrow. This position corresponds to the boundary of the etch pit which is also depicted an orange arrow in Fig. 4.13(b). In the discussion about converting frequency shift versus distance curves to water molecule distributions in section 4.5.2, the low frequency shifts corresponded to peaks in the water molecule distribution. If the same interpretation stands, then the water molecule distribution is higher near the boundary of an etch pit. Fig. 4.13(d) displays the frequency shift versus distance curve measured over the protrusions and valleys of the C16OH SAM and Fig. 4.13(e) shows the force versus distance curve converted from Fig. 4.13(d), using the Sader method.⁷⁰⁾

Looking at the force versus distance curve, the short range forces deviated from an exponential function. Also, a dip in the force versus distance curve occurred around 0.8 nm from the limit point, which was not observed in Figs. 4.7(c) and (d). Thus, it was concluded that forces apart from hydration forces acted on the tip in short ranges. Although the origin for this phenomenon is unclear, one reason may be due to the deformation of the SAM when the tip approaches the surface. Due to a stronger interaction force between the water molecules (argued in the following paragraph), the water molecules are more strongly bind to the alkanethiol SAMs than in C11OH SAMs and the alkanethiol SAMs tilt angle increases as the tip approaches the surface. Fig. 4.14 presents a schematic illustration of the force mapping method on C16OH SAMs. The deformation process acts linear in the force versus distance curve which is explains the derivation from the exponential curve in short ranges.

To discuss about the stronger interaction between water molecules and C16OH SAMs than C11OH SAMs, the argument is focused on the sulfur/gold interface. At the sulfur/gold interface, a charge transfer occurs from the gold surface to the sulfur atom and induces an electric dipole at the gold/sulfur interface.⁸⁸⁾ The electric dipole alters the work potential of the SAM which has been previously measured by KPFM measurements. These publications report that the amount

4. HYDRATION STRUCTURE MEASUREMENTS ON DIFFERENT SURFACE MOLECULAR ARRANGEMENTS OF HYDROXY TERMINATED SAMs

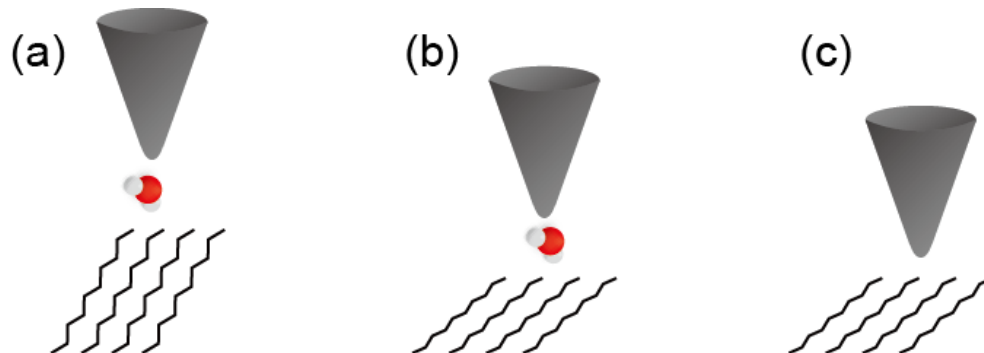


Figure 4.14: Schematic illustration of phenomenon happening at a C16OH SAM when the force mapping technique is applied. (a) The tip approaches the water molecules in the hydration layer of the C16OH SAM. (b) Since the interaction energy between the water molecules and C16OH SAMs are stronger than C11OH SAMs, the C16OH SAM deforms when the tip continues approaching the surface. (c) When the tip approaches for some distance, the water molecule is excluded from the space between the tip and C16OH SAM and the tip contacts the surface of the SAM.

of charge transfer depends on the chain length of the alkanethiol molecule. Ichii et al. reported that a single (CH_2) unit alters the surface potential by 9 mV per unit by FM-KPFM¹⁶¹⁾ while Lü et al. reported a 14 mV change by AM-KPFM.¹⁶²⁾ Thus, it can be assumed that the surface potential difference between a C11OH SAM and a C16OH SAM is around 50 mV. Generally, the surface potential is the net value of the dipole moment of each molecule and can be written in the following relationship.¹⁶³⁾

$$\Phi = \frac{N\mu}{\varepsilon_0\varepsilon} \quad (4.4)$$

Where Φ is the surface potential, N is the number density of the alkanethiol molecules, ε_0 is the permittivity of vacuum and ε is the relative permittivity of the alkanethiol SAM. When $\varepsilon = 2.7$,¹⁶⁴⁾ a 50 mV difference in the surface potential induces a dipole moment of $0.07D$. The maximum interaction energy between two electric dipoles can be written in the following expression.⁵¹⁾

$$\omega(r) = -\frac{2u_1u_2}{4\pi\varepsilon_0\varepsilon r^3} \quad (4.5)$$

Where $\omega(r)$ is the interaction energy, u_1 and u_2 are the dipole moment of two objects and r is the distance between the two objects. When the interaction

energy is calculated by eq. 4.5, then the interaction energy is $\omega(r) = 0.8[kT] = 2[kJ/mol]$. Notice that the $r = 0.2[nm]$ and $\varepsilon = 1$, and the interaction energy between the alkanethiol molecule and the nearest water molecule is calculated. (The same assumption has been made in ref. 51) It is unclear whether this energy difference is enough to alter the behavior of the water molecules when the tip approaches the surface, but it should enhance the interaction force between water molecules and the C16OH molecules.

4.7 Summary

Hydration structures of C11OH SAMs were measured using the force mapping technique of FM-AFM in 0.1 M KCl solution. The 2D frequency shift images between different molecule structures were imaged in this study, namely the $(\sqrt{3} \times \sqrt{3})R30^\circ$ structure and the $c(4 \times 2)$ superlattice structure. The 2D frequency shift images showed unambiguous differences in the hydration structures, where the lateral periodicity of the dark dot patterns were different in the two structures. The frequency shift versus distance curves were first converted to force versus distance curves using the Sader method and then converted to local water molecule distributions assuming the STA. The results show that the water molecule distribution depends on the topography of the surface, where the lateral periodicity of the water molecules corresponds to the lateral periodicity of the surface. The results prove that the surface topography has a huge impact on the entire hydration structure.

5

Development of Electrochemical AFM Applied to Hydration Structure Measurements

5.1 Introduction

A major topic about the solid/liquid interface is the relationship between the EDL and hydration structure. The two concepts derive from different fields; the existence of the EDL can be calculated by the PB equation which treats the solution as a continuum medium, while hydration (and solvation) structures are based on the fact that the size of the solution molecules aren't negligible and the geometric aspects of the molecules should be considered. So actually, these two ideas are based on completely different fields and the relationship hasn't been clearly elucidated. The relationship between the surface charge (potential) and hydration structure remains an open question and is demanded to be solved from many research fields.

As discussed in section 3.5.2, the first attempt to alter the surface charge in this study was to measure the hydration structure of a COOH functionalized SAM. This didn't work because the halogen anions somehow corrupted the images by adsorbing on the COOH surface. Therefore, the next approach was to dynamically control the surface potential by developing an electrochemical AFM

5.2 Instrumentation of the EC-AFM

(EC-AFM). A famous phenomenon due to the voltage impression on the solid-liquid interface is electrowetting. When an electric potential is applied between a water droplet and a metal electrode, the contact angle (CA) of the droplet changes depending on the potential applied.¹⁶⁵⁾ The phenomenon is an effective technique to control wetting in applications such as microfluidic systems,¹⁶⁶⁾ microlenses¹⁶⁷⁾ and reflective displays.¹⁶⁸⁾ Although the phenomenon can be well explained by electromagnetics, the interface structure at the electrode/liquid interface still remains a mystery. Another topic including the hydration structure and surface charge is the salting out effect of proteins and colloids.^{169–171)} First reported from F. Hofmeister back in the 19th century, the amount of the electrolyte needed to precipitate a protein varies between ions. The Hofmeister series ranks the salting out ability of these ions and is known that the series has a strong correlation with the entropic hydration energy of the ion. Now it's widely accepted that the Hofmeister series appears in almost every physical property of aqueous solutions, such as viscosity, pH and activity coefficients.¹⁶⁹⁾ Although the strong correlation between the hydration energy and the Hofmeister series is clear, scientists still can't theoretically explain the mechanism. Just simply utilizing electromagnetics is insufficient because the valence of the ion is only considered and can't explain the different behaviors of the electrolyte with the same valence.¹⁶⁹⁾

In this chapter, an EC-AFM was developed and applied to the force mapping technique. First the instrumentation of the EC-AFM will be discussed where the cantilever and sample holder were redesigned. After the operation of the new instrumentation was confirmed, the hydration structure of HOPG was measured by using the EC-AFM and the influence of the different surface potentials applied were examined.

5.2 Instrumentation of the EC-AFM

A simple method to apply electric potential in solution is to introduce two electrodes and apply electric potential from an external power source. In this system the voltage drops at the two electrode/electrolyte interfaces and the resistance of the solution. This means that it's impossible to measure the voltage drop

5. DEVELOPMENT OF ELECTROCHEMICAL AFM APPLIED TO HYDRATION STRUCTURE MEASUREMENTS

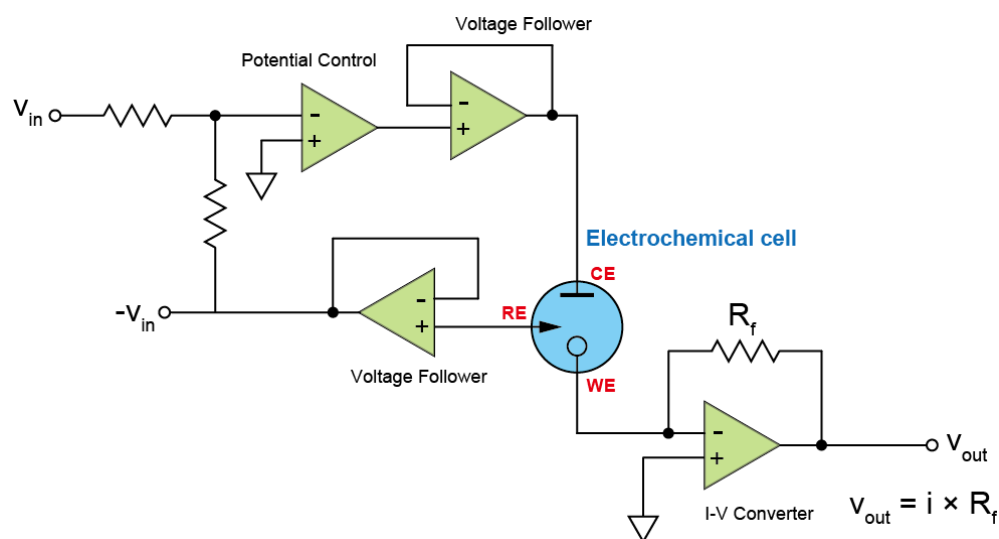


Figure 5.1: A schematic illustration of the electrical circuit of a typical potentiostat. v_{in} is the input voltage

occurring at the individual electrodes. To circumvent this problem, a three electrode system is usually employed to the instrument. The three electrodes are the working electrode, counter electrode and reference electrode, and is controlled with a potentiostat. Fig. 5.1 illustrates a simplified electrical circuit of the three electrodes controlled with a potentiostat. The principle idea of the potentiostat is to control the potential of the reference electrode against the working electrode. The working electrode is connected to a I-V converter and therefore, the working electrode is virtually short to the ground state. The reference electrode is controlled to be maintained at $-v_{in}$, where v_{in} is the input voltage. Hence, the potential difference between the reference electrode and the working electrode is $0 - (-v_{in}) = v_{in}$ and the input voltage is correctly applied between the two electrodes. The counter electrode and reference electrode are both connected to a voltage follower, but they are inserted in the opposite direction. Voltage followers have a high input impedance and a low output impedance, so the two voltage followers are adjusting the impedance of the electrodes. The high impedance of the reference electrode avoids electrons to flow in. On the other hand, the counter electrode has a low impedance. Hence, the electrons flow into the counter electrode and ideally, no voltage drop occurs at the reference electrode.

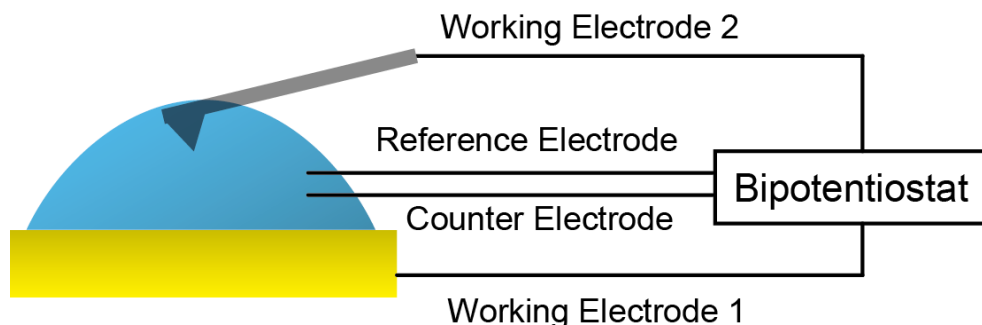


Figure 5.2: Schematic illustration of the EC-AFM utilized in this study. The potential of the sample and cantilever were controlled as working electrodes by a bipotentiostat. Two platinum wires were inserted into the cell and acted as a counter electrode and pseudo reference electrode.

Fig. 5.2 illustrates the concept of the EC cell combined with a three electrode system. The potential of the sample and cantilever were chosen as the working electrodes and were controlled with a bipotentiostat. Platinum wires were used as a counter electrode and a pseudo reference electrode because they are chemically stable. From here, the details of the redesigned instrument will be explained.

5.2.1 Sample Holder

Figs. 5.3 and 5.4 display the design drawing of the top and bottom component of the sample holder. The two components were made of polychlorotrifluoroethylene (PCTFE) which is chemically stable. The substrate is enclosed by the two components and is fixed by tightening a M1.2 polyether ether ketone (PEEK) screw. An O-ring made by fluoropolymer was inserted between the counterbore of the top component (depicted as A in Fig. 5.3) and substrate to prevent the liquid from leaking. The sample holder was designed to measure electrochemical properties of gold films evaporated on mica substrates, which means the electric contact can't be taken with the backside of the sample and must be taken from the top of the surface. To do so, a 0.2 mm thick platinum plate was glued to a dent part (depicted as B in Fig. 5.3). The platinum plate made contact with the surface of the substrate, so the potential of the sample was controlled by clipping a wire to the platinum plate. The center of the hole in top component was shifted

5. DEVELOPMENT OF ELECTROCHEMICAL AFM APPLIED TO HYDRATION STRUCTURE MEASUREMENTS

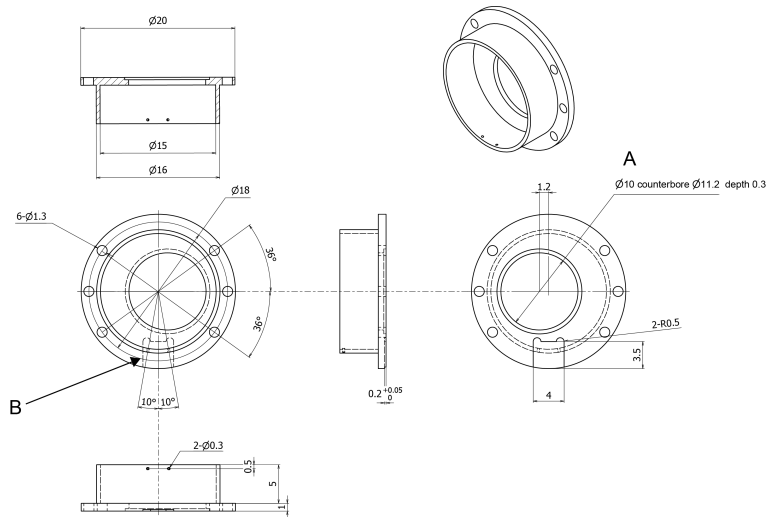


Figure 5.3: A design drawing of the top component of the sample holder utilized in the EC-AFM.

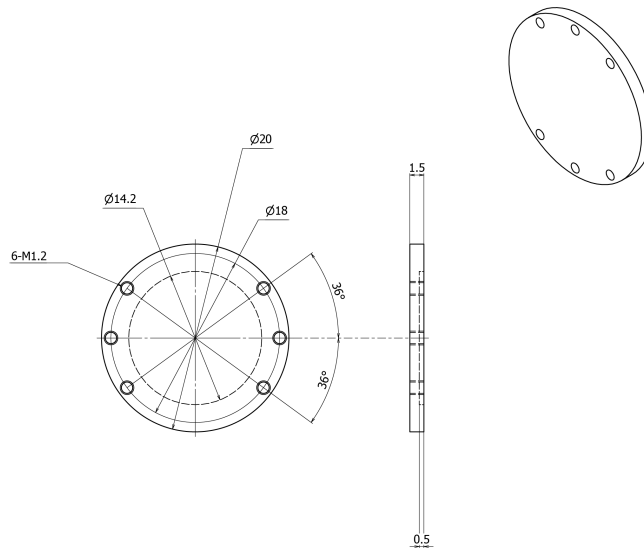


Figure 5.4: A design drawing of the bottom component of the sample holder utilized in the EC-AFM.

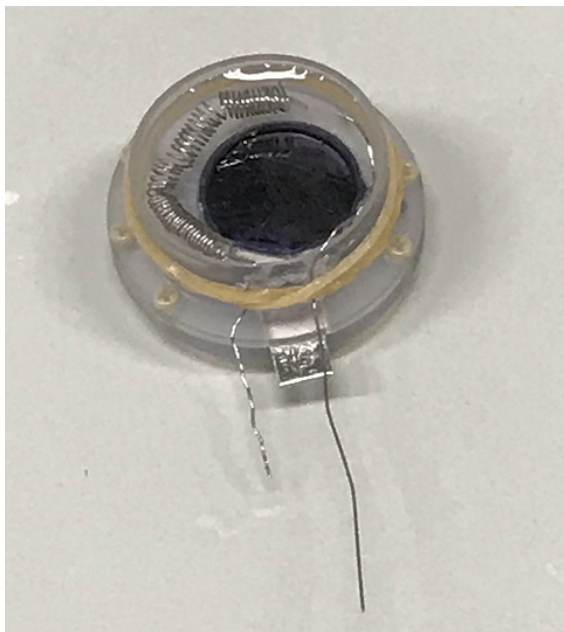


Figure 5.5: A photograph of the sample holder utilized in this study. Platinum wires were used as a counter electrode and a pseudo reference electrode. Both wires were fixed with an elastic band outside the sample holder.

1.2 mm to the side to take alignment with the cantilever holder.

A requirement in an electrochemical setup is to make sure the area of the counter electrode is bigger than the area of the working electrode, to ensure the current is not limited by the area of the counter electrode. This is a difficult task in EC-AFM measurements because the actual space to introduce such large areas are inadequate in most AFMs. The region exposed to the solution can be described as a 10 mm diameter circle and the area is 78.5 mm^2 . The counter electrode was made by winding up 250 mm of a 0.2 diameter platinum wire into a coil, which was about 157 mm^2 , nearly double the area of the working electrode. A platinum wire was also used as a pseudo reference electrode. The wires were taken out from the cell and fixed with an elastic band outside the cell. Fig. 5.5 shows a photograph of the sample holder holding a HOPG substrate and fixed with PEEK screws.

5. DEVELOPMENT OF ELECTROCHEMICAL AFM APPLIED TO HYDRATION STRUCTURE MEASUREMENTS

5.2.2 Cantilever Holder

Figs. 5.6 and 5.7 present the design drawing of the cantilever holder and the outside metal frame, respectively. The cantilever holder was made of quartz while the metal frame was made of stainless steel. The cantilever was set on tilted plane of the bottom of the cantilever holder (depicted as A in Fig. 5.6) and was fixed with a U-shaped metal plate. The cantilever was tilted for 12° against the horizontal plane which insures the path of the detection laser. The metal plate was plated with gold to take electrical contact with the external bipotentiostat and to ensure chemical stability. The cantilever holder was fixed to the metal frame with M2 PEEK screws through three holes on the top of the cantilever holder (depicted as B in Fig. 5.6). The conventional cantilever holder was fixed to the metal frame with an adhesive agent which prevented conducting

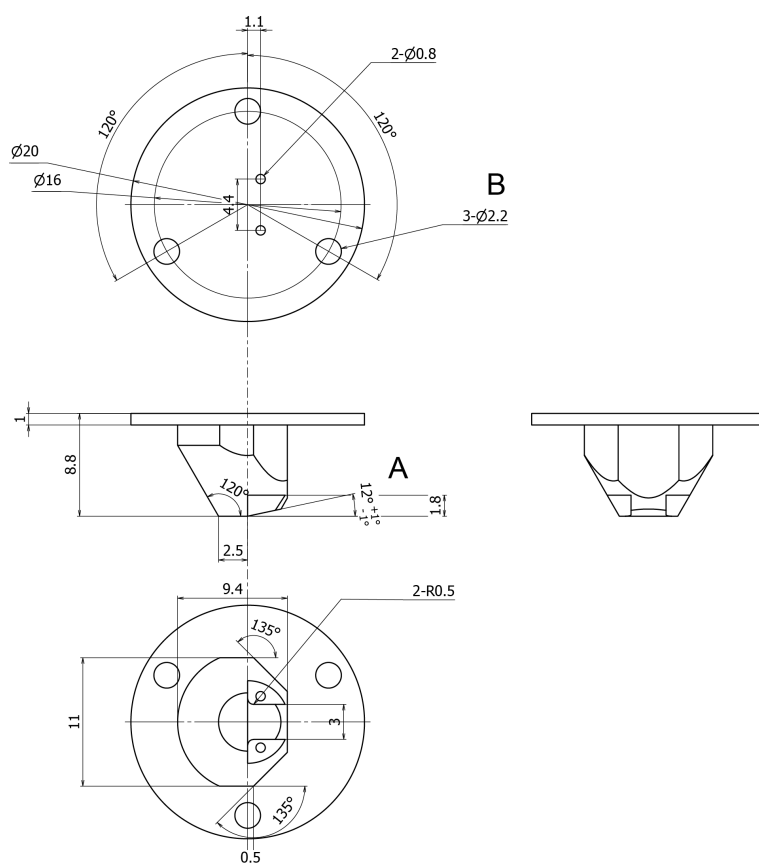


Figure 5.6: A design drawing of the cantilever holder utilized in the EC-AFM.

5.2 Instrumentation of the EC-AFM

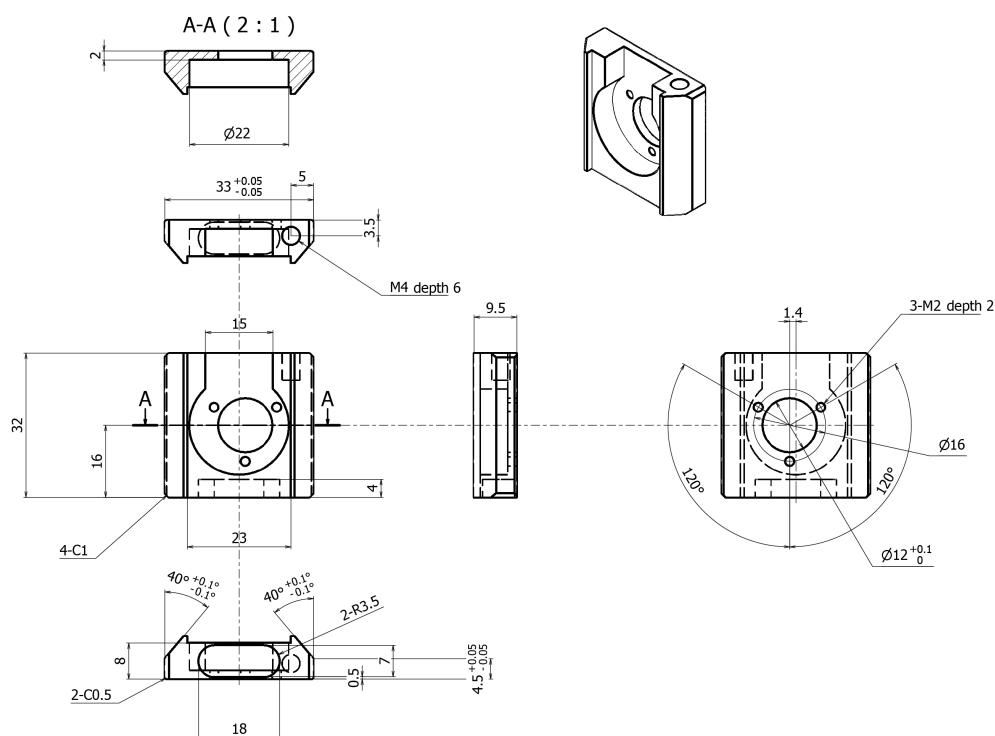


Figure 5.7: A design drawing of the metal frame of the cantilever holder utilized in the EC-AFM.

UV/ozone cleaning on the cantilever holder. Eliminating glue from the cantilever holder was an important step in cleaning the cantilever holder and enabled to measure the 0.3 nm oscillation on hydrophobic SAMs as mentioned in chapter 3. Applying UV/ozone cleaning on the adhesive agent used cantilever holder decomposed the adhesive agent and resulted in enormous drift during imaging.

5.2.3 Operation Procedure of the EC-AFM

Fig. 5.8 displays a schematic picture of the cantilever holder and sample holder constructed for the EC-AFM. Before each experiment, the platinum wires were sonicated in MilliQ water for 15 minutes and then cleaned by applying DC between the two electrodes. The DC bias was applied for three minutes and then the polarity was inverted and another three minutes of DC bias was applied. This was continued for two sets and made the potential of the pseudo reference electrode stable. The cantilever holder was cleaned in UV/ozone cleaning for 20

5. DEVELOPMENT OF ELECTROCHEMICAL AFM APPLIED TO HYDRATION STRUCTURE MEASUREMENTS

minutes before each experiment. The sample holder was constructed according to Fig. 5.8 and was operated with the AFM apparatus used in chapter 3 and 4. The potential of the sample and cantilever were controlled with a bipotentiostat. (BAS Electrochemical Analyzer, 704C) A Cr/Pt covered cantilever was used with a typical resonance frequency and spring constant of 120 kHz and 17 N/m, respectively, in aqueous conditions. The potential of the pseudo reference electrode was corrected against the Ag/AgCl reference electrode, and the potential difference was measured at each experiment. Before applying the EC-AFM on hydration structure measurements, an operation test was conducted to check the ability of AFM imaging and electrochemical measurements while using the EC cell.

5.3 Operation Tests of the EC-AFM

5.3.1 AFM Imaging

To check the AFM imaging ability of the EC-AFM cell, binary phase separated SAMs and mica substrates were chosen. The binary phase separated SAM was composed of 3-mercaptopropionic acid (C2COOH) and 1-decanethiol (C10) molecules and were fabricated in same method as in chapter 3. Fig. 5.9 presents the topographic image of the binary phase separated SAM and the mica substrate. The "sea-island" structure was observed which resembles the binary phase separated SAM composed of C6OH and C11OH SAMs fabricated in section 3.6. On the other hand, the narrow view image of the mica substrate showed a hexagonal pattern with a period of 0.51 nm, which matches the distance between the center of the honeycombs on mica. Therefore, it was confirmed that atomic-resolution imaging with the EC-cell was achieved.

5.3.2 Cyclic Voltammetry

To check the ability of measuring electrochemical properties using the EC cell, a cyclic voltammetry (CV) was conducted. In cyclic voltammetry, the potential of the working electrode is swept and the current inflowing into the working

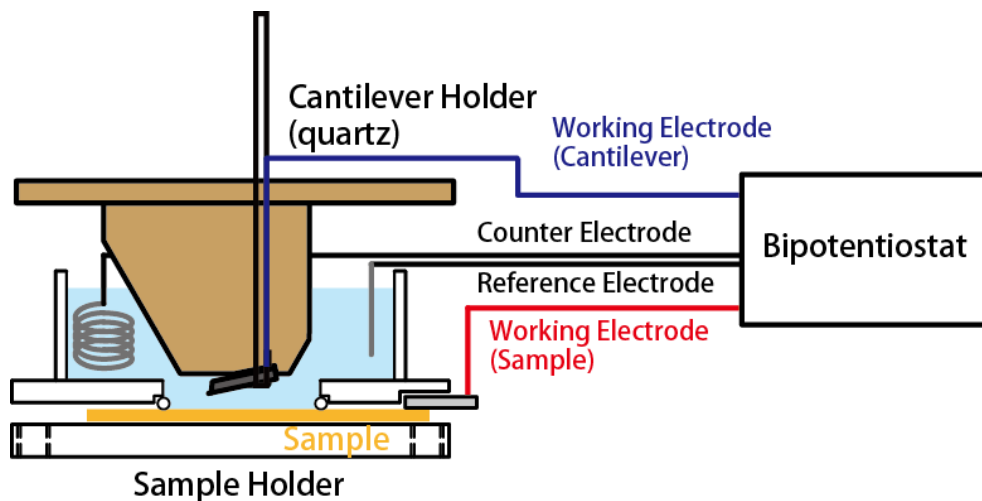


Figure 5.8: A design drawing of the EC cell utilized in this study. The sample holder was constructed with the components presented in Figs. 5.3 and 5.4 and the cantilever holder was constructed with components displayed in Figs. 5.6 and 5.7, respectively.

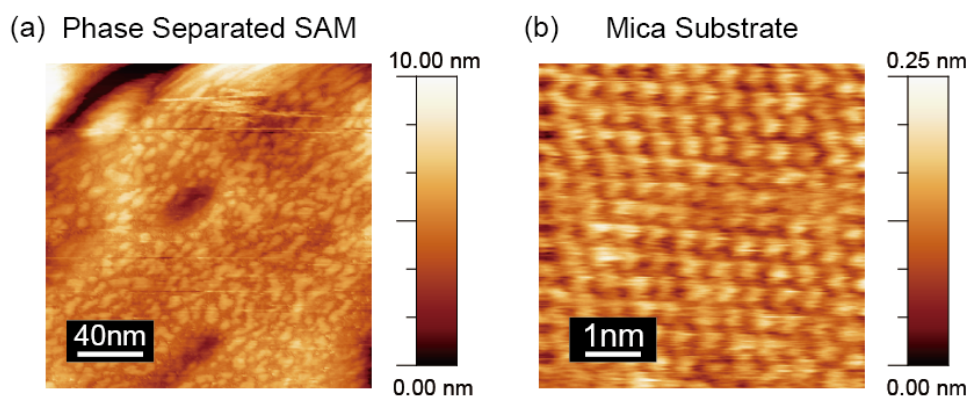


Figure 5.9: (a) Wide view topographic image of a binary phase separated SAM. The phase separated SAM was composed of C2COOH and C10 molecules. (b) Narrow view topographic image of a mica substrate. An atomic-resolution image of the mica surface was obtained.

5. DEVELOPMENT OF ELECTROCHEMICAL AFM APPLIED TO HYDRATION STRUCTURE MEASUREMENTS

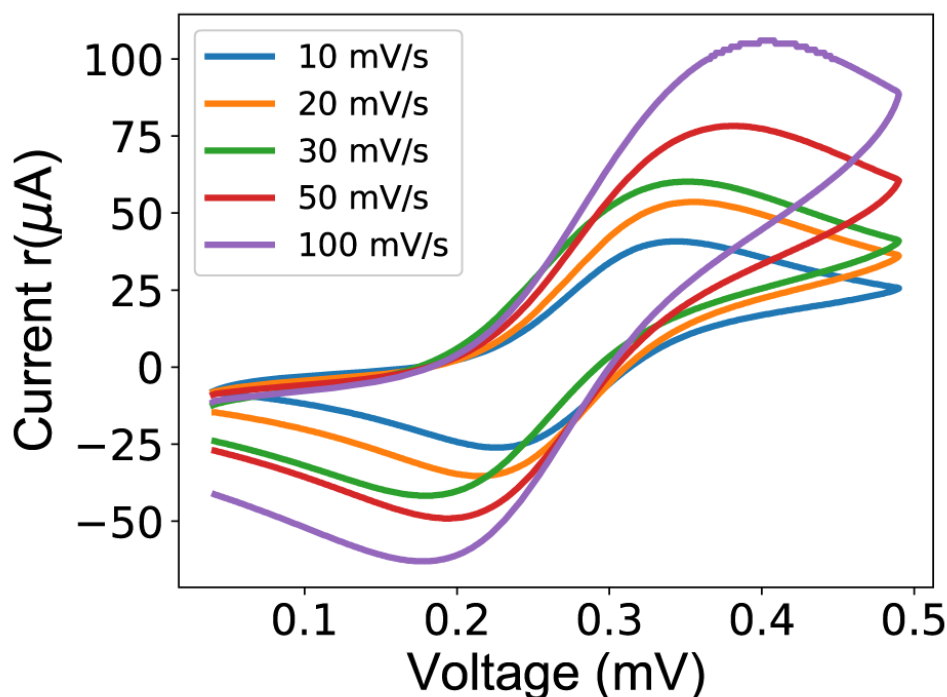


Figure 5.10: Cyclic voltammogram of potassium ferrocyanide on HOPG substrates. The concentration of the solution was 1 M KCl + 1 mM $K_4[Fe(CN)_6]$. The potential was corrected against an Ag/AgCl reference electrode.

electrode is recorded. Cyclic voltammetry is a simple and popular method to investigate the oxidation-reduction potential of a desired sample. To ensure the electrochemical control is possible with the EC-cell, the redox-oxidation property of potassium ferrocyanide ($K_4[Fe(CN)_6]$) on a HOPG substrate was measured.

Fig. 5.10 displays the cyclic voltammogram of potassium ferrocyanide on HOPG substrates. The potential was corrected against the Ag/AgCl reference electrode, where the potential difference between the 1 mM $K_4[Fe(CN)_6]$ was added to a 1 M KCl solution which was utilized as the electrolyte. It is clear that increasing the scanning rate of the voltage sweep showed an increment in the current. These features are consistent with proceeding studies¹⁷²⁾ Thus, it was confirmed that electrochemical measurements such as CV are possible using the EC cell.

5.4 Hydration Structure Measurements Applying the Developed EC-AFM

5.4.1 Physical Property of Graphene

The developed EC-AFM was applied to measure the hydration structure of HOPG substrates. Fig. 5.11 presents the surface structure of graphene. Graphene possess a honeycomb structure with an interatomic distance of 142 pm and the distance between the center of the honeycombs are 246 pm.¹⁷³⁾ It also has several unique properties such as high electron mobility,¹⁷⁴⁾ lubrication¹⁷⁵⁾ and electrochemical stability,¹⁷⁶⁾ and is now applied to a wide variety of research fields. Along side its high potential in applications, graphene is also a typical hydrophobic substrate often used in AFM measurements. This is because of its atomic scale flatness and the simplicity to prepare a pristine surface, which are both crucial in AFM measurements. Only a few reports have been made on force mapping measurements combined with electrochemical control. Utsunomiya et al., reported the hydration structure depends on the surface potential of graphene, where the hydration structure was formed in cathodic potentials and the oscillations vanish in anodic potentials.¹⁷⁷⁾ Thus, HOPG was chosen as the substrate to compare the results with previous reports. The possibility of 2D frequency shift mapping were also investigated.

5.4.2 Force Mapping Measurements on HOPG

The developed EC-AFM was combined with the force mapping technique to measure the hydration structure of the solid-liquid interface. Most of the reports utilizing EC-AFMs and EC-STMs focus on the topographic changes induced by potential control.^{178–180)} The potential control during force versus distance curve measurements target on long range electrostatic forces and only few have measured the changes in molecular scale, such as water^{177,181)} or ionic liquids.¹⁸²⁾ As far as the authors knowledge, there is only one report measuring 2D interface structure in ionic liquids with electrochemical control¹⁸²⁾ and no reports have been published on hydration structure measurements. This is the main goal in

5. DEVELOPMENT OF ELECTROCHEMICAL AFM APPLIED TO HYDRATION STRUCTURE MEASUREMENTS

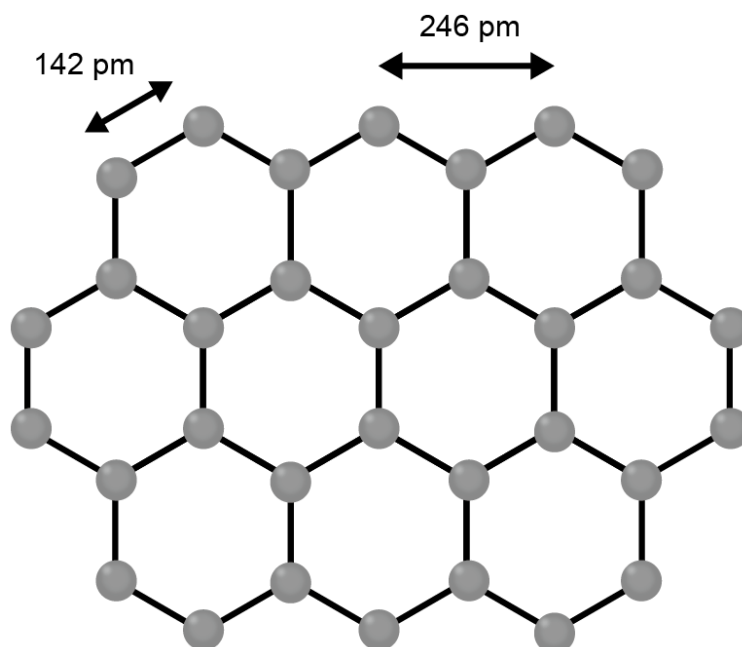


Figure 5.11: Cartoon illustrating the top view structure of graphene. The gray spheres depict the carbon atoms and the black lines present the chemical bonds.

this section and if achieved, should extend the application of FM-AFM and force mapping techniques to electrochemical fields such as batteries and electrochemical synthesis.

First, the influence of applying potential to an oscillating cantilever was investigated. Fig. 5.12(a) shows the potential applied to a platinum coated cantilever and Fig. 5.12(b) displays the deflection signal during the potential application. The deflection changed for about 1 nm when the potential altered from -0.1V to +0.1V and from +0.1 V to -0.1V. This is due to the interface energy change induced from the alteration in the surface potential. When the surface potential at the solid-liquid interface varies, the electrostatic energy density preserved at the EDL also changes and the changed portion decreases or increases the interface energy at the solid-liquid interface. This phenomenon is the reason why electrowetting occurs, because the alteration of the solid-liquid interface energy causes the contact angle to vary. At a cantilever, the variation in the interface energy induces surface stress and results the cantilever to bend.¹⁴⁴⁾ This phenomenon has been reported to occur on cantilevers with the back-side gold

5.4 Hydration Structure Measurements Applying the Developed EC-AFM

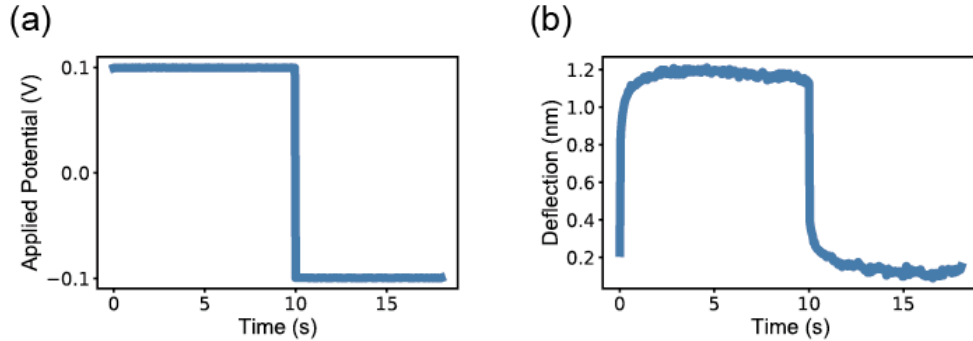


Figure 5.12: (a) The potential applied to an oscillating platinum coated cantilever in 0.1 M HClO₄ solution. (b) The deflection signal of the cantilever when the voltage pulse was applied.

coated where the alteration in the surface stress should be large. In a Pt coated cantilever, the surface stress induced on the top and bottom side of the cantilever should be equal, and no deflection should occur. However, even if the material is the same, the properties of both coating can vary such as the surface roughness or the crystal orientation and can cause a difference of the surface stress.

Figs. 5.13 present a 2D frequency shift map taken over a HOPG substrate in 0.1 M HClO₄ solution. The potential of the cantilever was controlled at +0.82 V while the surface potential of the HOPG substrate was controlled at +0.92 V in Fig. 5.13(a) and +0.32 V in Fig. 5.13(b). It should be noted that Figs. 5.13(a) and (b) were consecutively measured and measure the same position on the substrate. There were virtually no patterns in Fig. 5.13(a) while line patterns were partially observed in Fig. 5.13(b) which suggests the existence of a hydration structure. Fig. 5.13(c) and (d) display the frequency shift versus distance curve extracted from Fig. 5.13(a) and (b), respectively. When +0.32 V was applied on the HOPG surface, oscillations were observed with a period of 0.36 nm which confirms the existence of a hydration structure.

The impact of the surface potential on the hydration structure was also measured in a single image. Fig. 5.14 shows a 2D frequency shift image obtained while the surface potential was altered from +0.32 V to +0.92 V. The surface potential are depicted in the red and green arrows in Fig. 5.14(a). When the potential was altered, the apparent position of the surface instantaneously moved.

5. DEVELOPMENT OF ELECTROCHEMICAL AFM APPLIED TO HYDRATION STRUCTURE MEASUREMENTS

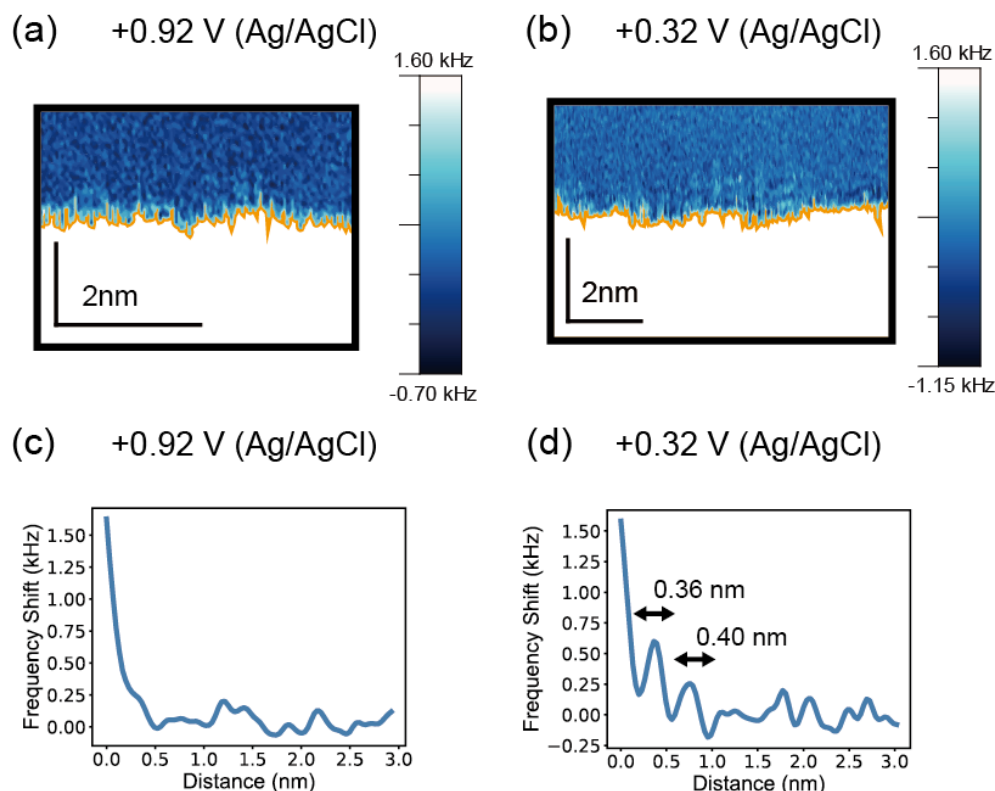


Figure 5.13: (a), (b) 2D frequency shift map obtained over a HOPG substrate in 0.1 M KClO_4 solution. The potential was controlled at +0.92 V and +0.32 V against (a) and (b), respectively. The yellow line depicts the surface of the HOPG substrate. (c), (d) Frequency shift versus distance curves extracted from (a) and (b), respectively.

This is due to the variation in the interface energy between the top and bottom plane of the cantilever which induces deflection. The same phenomenon was observed in Fig. 5.12. Fig. 5.14(b) and (c) present the frequency shift versus distance curve extracted from Fig. 5.14(a). The surface potential was +0.32 V in Fig. 5.14(b) and +0.92 V in Fig. 5.14(c), respectively. As in Fig. 5.13, a 0.30 nm period oscillation was measured when the surface potential was +0.32 V and vanished when the potential was changed to +0.92 V. From these results it can be concluded that hydration structures form at +0.32 V and disappear at +0.92 V. It's hard to define whether this is due to the difference in the electrostatic interaction between the surface and ClO_4^- anions, or the reconstruction of the

5.4 Hydration Structure Measurements Applying the Developed EC-AFM

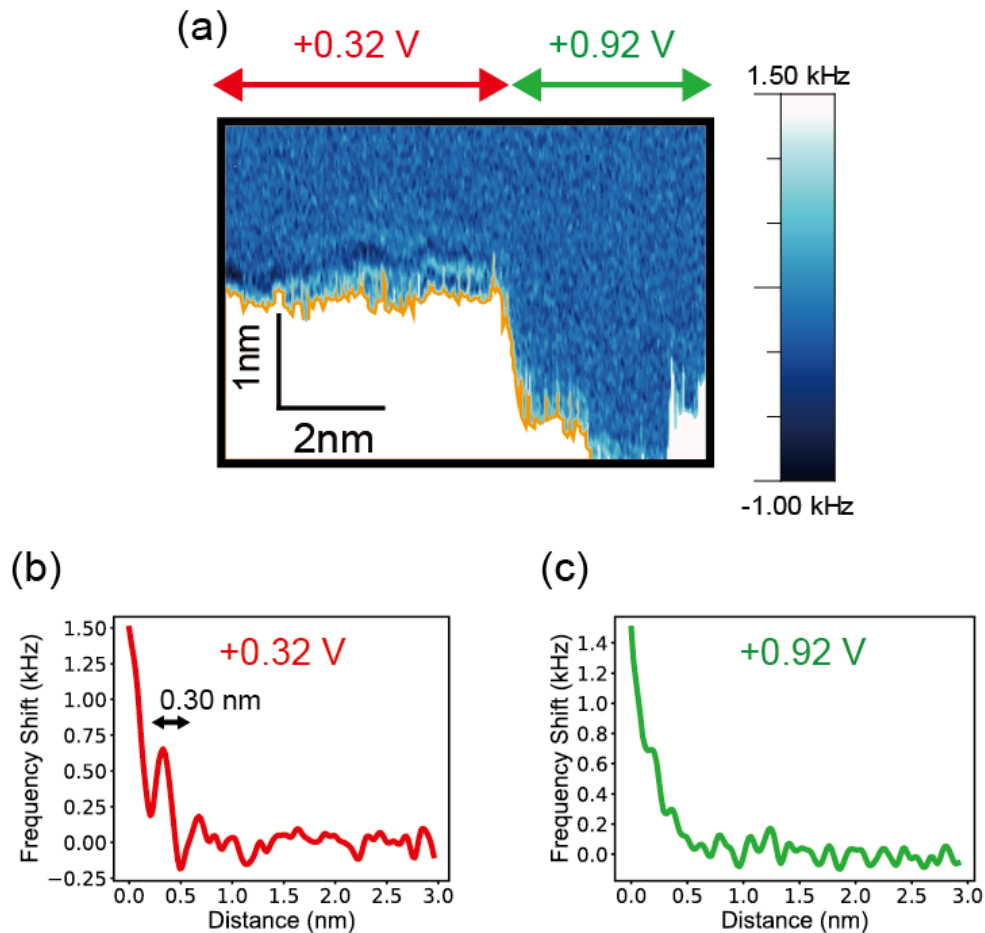


Figure 5.14: (a) 2D frequency shift map measured over a HOPG substrate in 0.1 M KClO_4 solution. The red and green arrows depict the potential of the substrate while the 2D frequency shift map was achieved. (b) and (c) are frequency shift versus distance curves extracted from (a). The potential of the substrate was +0.32 V and +0.92 V in (b) and (c), respectively.

EDL. Utsunomiya et al., measured the 1D frequency shift versus distance curve on HOPG in perchloric acid on HOPG with a EC-FM-AFM. They found that hydration structure were enhanced in cathodic potentials when the solution was perchloric acid and concluded that the results are due to the reconstruction of the EDL.¹⁷⁷) Ions are known to form a hydration structure as found in the solid-liquid interface. When the interaction between the ion and water molecule are

5. DEVELOPMENT OF ELECTROCHEMICAL AFM APPLIED TO HYDRATION STRUCTURE MEASUREMENTS

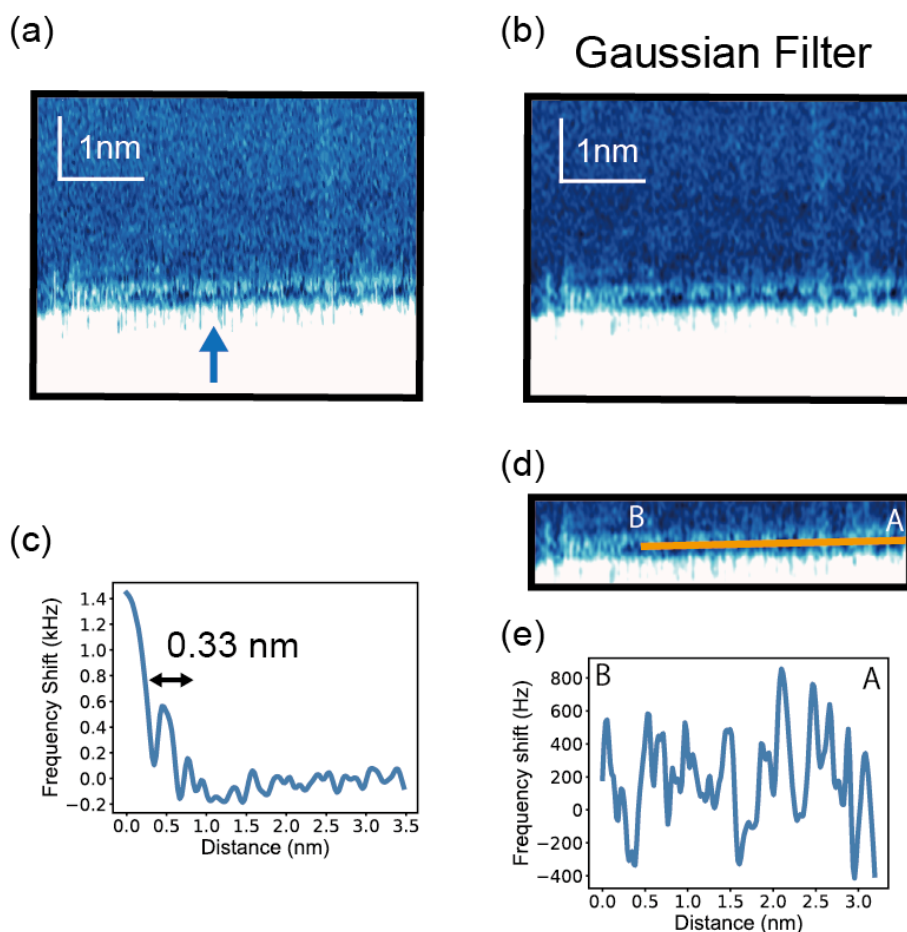


Figure 5.15: (a) 2D frequency shift map achieved over an HOPG substrate in 0.1 M HClO_4 solution. (b) Gaussian filter applied to (a) to emphasize the inhomogeneous pattern in the hydration structure. (c) Frequency shift versus distance curve extracted from (a). The curve was extracted at the position depicted in the blue arrow in (a). (d) displays a magnified view at the vicinity of the HOPG surface. (e) shows a profile of the frequency shift depicted by the orange line in (d).

stronger than the interaction between water molecules themselves, the ion forms a hydration shell and are called kosmotropic ions. On the other hand, when the interaction between the ion and water molecule is weak, the finite size of the ion disrupts the surrounding hydrogen bond network and are called chaotropic ions. These kosmotropic and chaotropic ions are known to be attractive with hydrophilic and hydrophobic materials, respectively.¹⁸³⁾ ClO_4^- anions are chaotropic

5.4 Hydration Structure Measurements Applying the Developed EC-AFM

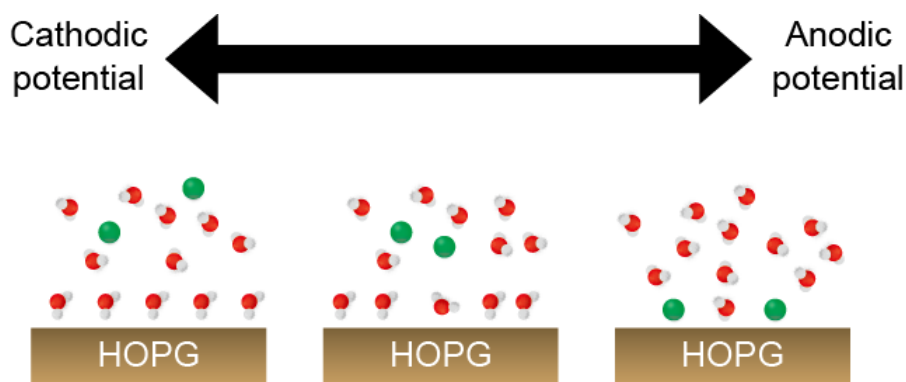


Figure 5.16: Schematic illustration of the hydration structure formed on a HOPG substrate in 0.1 M HClO_4 solution. The red molecule depicts a water molecule while green spheres depict a perchloric anion.

and are known to break the hydrogen bond networks. Therefore, the higher potentials have a stronger interaction with the ClO_4^- anions which break the intrinsic HOPG hydration structure. It seems that the same scenario can also be applied to this study.

The EC-AFM also demonstrated that the in-plane pattern of the hydration structure can be measured in this apparatus. Fig. 5.15(a) displays the 2D frequency shift map obtained on an HOPG substrate in 0.1 M HClO_4 solution. The data set was achieved in a different data set of Fig. 5.13 and Fig. 5.14. The potential of the tip and substrate were both fixed at +0.26 V. To the best of the authors' knowledge, this is the first study to report the 2D frequency shift map in aqueous conditions with electrochemical control. An inhomogeneous in-plane pattern was found showing a dot-like pattern. Fig. 5.15(b) presents a Gaussian filter applied to Fig. 5.15(a), in order to emphasize the inhomogeneous pattern. Fig. 5.15(c) displays the frequency shift versus distance curve extracted from Fig. 5.15(b) depicted by the blue arrow. A 0.33 nm period oscillation was found which is consistent with the earlier results and ensures that hydration structures form at cathodic potentials. Fig. 5.15(e) displays the profile of the frequency shift depicted in the orange line in Fig. 5.15(d). Peaks and dips were found in Fig. 5.15(e) which proves the in-plane patterns weren't homogeneous. The period of the dips were about 0.25 nm and matches well with the distance between the

5. DEVELOPMENT OF ELECTROCHEMICAL AFM APPLIED TO HYDRATION STRUCTURE MEASUREMENTS

honeycomb center of the HOPG surface, which is 0.26 nm. Therefore, it can be concluded that the in-plane local water molecule distribution is inhomogeneous and is related with the HOPG surface.

Fig. 5.16 illustrates the relationship between the hydration structure and the potential of the HOPG substrate. Previous reports on force mapping measurements on HOPG substrates report a homogeneous line pattern,^{82,84)} which is clearly different from the results obtained here in cathodic potentials. Thus, it can be concluded that the inhomogeneous pattern is due to the potential control of the EC-AFM. This also shows that ClO_4^- anion isn't the only factor that alters the hydration structure, since it doesn't explain why water molecules to more strongly interact with the surface. Hence, the hydration structure of HOPG is influenced by the entropic hydration property of the ions and the interaction between the water molecules and surface. From Fig. 5.15, it was demonstrated that the combining an electrochemical setup with the force mapping technique, it is possible to measure the local 2D hydration structure at different surface potentials which should expand the application of EC-AFM to other research fields.

5.5 Summary

In this chapter, an EC-AFM was developed by designing a sample holder and cantilever holder which is capable of introducing a three electrode system. The designed components were built together and two operation tests were conducted. Atomic-resolution images of mica substrates were obtained which ensured the ability to obtain topographic images in atomic resolution. The electrical conditions were checked by measuring the CV of $\text{K}_4[\text{Fe}(\text{CN})_6]$ which matched well with proceeding results. When the EC-AFM was applied to hydration structure measurements on HOPG substrates, it was found that cathodic potentials form hydration structures while anodic potentials disrupt the hydration structure. Also, by achieving a 2D frequency shift map, it was found that inhomogeneous hydration structures form on HOPG in cathodic potentials. This is the first report to measure 2D frequency shift maps in electrochemical control and demonstrates that combining 2D force mapping techniques with electrochemical

5.5 Summary

control is a powerful method and can be applied electrochemical applications such as batteries.

6

Conclusions and Future Work

6.1 Conclusions

In this thesis, hydration structures were measured by the 2D force mapping technique of FM-AFM. The following conclusions were made from this study.

1. The hydration structures of hydrophilic and hydrophobic alkanethiol SAMs were compared by measuring 2D frequency shift maps on OH terminated and CH₃ terminated SAMs, respectively. The OH terminated SAMs showed dot like patterns which depict the water molecules are locally strained on the SAM surface, while CH₃ terminated SAMs showed line patterns which mean the water molecules are not localized. The tip effect was considered by measuring the 2D frequency shift map on a binary phase separated SAM composed of C6OH and C16 molecules. The 2D frequency shift map displayed the same patterns as the single phase SAMs and it was concluded that these results are not due to the tip effect. Also, peculiar feature were obtained on hydrophobic SAMs and were suggested to be due to hydrocarbon contamination, since the frequency of the feature appearing decreased when a thorough cleaning process was conducted.
2. The hydration structures of C11OH SAMs with different molecular structures, namely, the $(\sqrt{3} \times \sqrt{3})R30^\circ$ structure and the $c(4 \times 2)$ superlattice structure were compared to elucidate the influence of atomic corrugation

on local hydration structures. Both structures showed a dot pattern, but the in-plane periodicity was 0.5 nm for the $(\sqrt{3} \times \sqrt{3})R30^\circ$ structure and 1.0 nm for the $c(4 \times 2)$ superlattice structure. This matches with the intermolecular distance of the $(\sqrt{3} \times \sqrt{3})R30^\circ$ structure and the length of the primitive unit cell of $c(4 \times 2)$ superlattice structure. This result suggests that the overall hydration structure is effected by atomic corrugation with an amplitude of less than 50 pm which is about 15% of a single water molecule. Therefore, even small atomic corrugations can alter the hydration structure and should be considered when analyzing hydration structures. Also water molecule distributions were obtained by converting force versus distance curves with the STA, which matched well with proceeding reports.

3. An EC-AFM was developed and was used to measure the hydration structure change due to the application of electric potential. The sample holder and cantilever holder were redesigned to introduce a three electrode system to the apparatus. The operation of the EC-AFM was checked by imaging the mica surface with atomic resolution and by measuring the CV of $K_4[Fe(CN)_6]$ on a HOPG substrate. After the operation tests, the EC-AFM was applied to HOPG substrate in 0.1 M $HClO_4$ solution to investigate the effect of electrical potential on hydration structures. 0.3 nm period oscillations were found when anodic potential was applied to the HOPG substrate which matches with the size of a single water molecule, while these oscillations vanished when anodic potential was applied. These results match with previous studies on the same system. Also, a 2D frequency shift map in cathodic potentials showed that the water molecules form a inhomogeneous pattern when cathodic potentials are applied to the substrate. As far as the authors knowledge, this is the first study to observe 2D hydration structures with electrochemical potential, and demonstrates that combining EC-AFM with 2D force mapping techniques is a powerful method to obtain solid/liquid interface structures in electrochemical systems.

Thus, the factors that impact the hydration structure were elucidated in this thesis.

6. CONCLUSIONS AND FUTURE WORK

6.2 Future Work

In this section, the author will make some suggestions for future work on hydration structure measurements.

Making a Robust EC-AFM

As shown in chapter 5, an EC-AFM cell was developed and combined with the force mapping technique to demonstrate the in-plane hydration structure can be measured in different potentials. However, successfully achieving a 2D frequency shift map under potential control is still tough and further development is necessary. The biggest problem is fixing the platinum wires in the EC cell. This is now obtained by using an elastic band, but most times the wires easily move around making contact with the substrate or cantilever. This decreases the possibility of measuring the local hydration structure and should be solved to achieve a robust EC-AFM cell.

Investigating the Interface Structure During Chemical Reactions

In chapter 5, it was demonstrated that the EC-AFM developed in this study can study the 2D hydration structure with electrochemical control. This is an effective technique to investigate the interface structure in electrochemical applications and should be utilized to measure the interface structure during chemical reactions, which should aid research in batteries and electrosynthesis. Especially, the properties of a lithium ion battery is related with the interface structure of the electrode/electrolyte solution interface. Achieving information about the real space interface structure with EC-AFM should accelerate the development of lithium ion batteries which is an important task in solving today's energy problems.

Appendix A

Synthesis of Gold Nanoparticles by a Vacuum Evaporation Method

A.1 Introduction

Metal nanoparticles are known to show novel properties compared to bulk states. The quantum size effect, high ratio of surface atoms, modulation of electronic states, etc. contribute to unique phenomena and properties such as surface plasmon resonance (SPR),⁴⁾ catalyst effects⁵⁾ and even ferromagnetism.^{6,184)} In particular, gold nanoparticles are attracting much attention for applications such as bio-imaging,^{185,186)} drug-delivery,^{185,187)} environmental catalysis^{4,188)} and high-density data storage media.^{6,184)} In 2006, Torimoto et al. developed a novel method to synthesize nanoparticles by the sputter deposition of gold onto ionic liquids (ILs).¹⁸⁹⁾ This is a simple and also "clean" method to synthesize nanoparticles, where the IL functions as a stabilizer as well as a solvent. This method excludes the usage of reducing agents and stabilizers, which are indispensable in conventional "wet" chemical methods¹⁹⁰⁾ which cause unintentional chemical reactions^{191,192)} or ill their useful properties such as their catalytic effects.¹⁹³⁾ For these purposes, much research has been conducted on "dry" synthesis methods for example, sputter deposition,^{189,191,194–198)} vacuum evaporation (VE)^{193,199,200)} and laser ablation.^{192,201)}

A. SYNTHESIS OF GOLD NANOPARTICLES BY A VACUUM EVAPORATION METHOD

Recently, the sputter deposition method has been applied to other non-volatile liquids such as vegetable oils (composed of fatty acids)^{202,203}) and polyethylene glycol²⁰⁴) to obtain nanoparticles. These liquids are not only bio and environmentally friendly but they are also cost effective compared to ILs, so they should be a promising candidate in industrial uses. In sputter deposition methods, however, the plasma or sputtered atoms could cause decomposition of the solvent.¹⁹⁸) In a preliminary experiment, gold was sputtered to an IL (1-butyl-3-methylimidazolium hexafluorophosphate : BMIM-PF6) which synthesized nanoparticles but also an unusual smell occurred from the apparatus, which implies the decomposition of the IL. Indeed, the sputter deposition method can be applied to various metals for nanoparticle synthesis,^{205,206}) which should be a huge advantage in means of application, including high-melting point metals, which are impossible to evaporate in VE methods. However, the plasma itself can affect the growth scheme. To prevent such events, Richter conducted VE on ILs and synthesized nanoparticles.^{193,198}) They carried out the VE inside a rotating glass flask where the IL was applied on the flask, but the mechanical disturbance induced by rotation should have an influence on the growth mechanism. Other reports demonstrated that VE methods also induce some kind of mechanical disturbance to the solvent,²⁰⁰) which motivated us to conduct the VE on "static" solvents, where only few reports have been made.²⁰⁷)

In this chapter, the author investigated the VE on "static" ricinoleic acid and oleic acid, which are unsaturated fatty acids (UFAs). Carboxyl acids act as surfactants and have been used as stabilizers of nanoparticles.²⁰⁸⁻²¹⁰) To take full advantage of the VE method, i.e. to avoid mechanical disturbance to the sample, a down deposition VE apparatus was developed. As a result, black aggregates were obtained just after deposition and found that nanoparticle formation occurs while the aggregates shrink and disappear. The phenomenon was examined by transmission electron microscopy (TEM), small-angle X-ray scattering (SAXS) and UV-Vis measurements and found a consistent result that the nanoparticles transferred from an aggregate to individual dispersed nanoparticles. It was also elucidated that the phenomenon was triggered by the exposure of oxygen, instead of progress of time in a vacuum and the oxidation of the gold atoms was negligible as confirmed by X-ray photoelectron spectroscopy (XPS). A growth mechanism is

proposed which does not contradict with these unusual results and VE methods should be a promising candidate for applications.

A.2 Experimental

Gold nanoparticles were synthesized by the VE method on UFAs. Fig. A.1(a) shows the VE experimental apparatus used in this paper. Ricinoleic acid (purity 88.8%) and oleic acid (purity 71.6%) were purchased from Wako Pure Chemical Industries and were used as received. Fig. 1(b) and (c) shows the structural formula of ricinoleic and oleic acids, respectively. 1.0 ml of each solvent was transferred to a Petri dish (diameter 36 mm) using a micropipette and the dishes were placed 10 cm below the filament and vacuumed in the apparatus. Au wires with a diameter of 0.5 mm (purity 99.99%) were purchased from Nilaco Corporation as the deposition source, and were hooked on a filament made from a W wire with a diameter of 0.8 mm (purity 99.99%, also purchased from Nilaco Corporation). The filament was heated by applying electrical current from an external power source. The deposition was conducted under a vacuum of 6×10^{-6} Torr to prevent excessive evaporation. The deposition rate was controlled to 1.0 Å/s and a total of 187 Å was deposited, both were monitored by an ULVAC CRTM-1000 quartz resonator. The concentration of the gold atoms of the sample was 0.03 wt%. After the deposition, the samples were taken out from the apparatus and were kept in atmospheric air until the solvent obtained a homogeneous color (typically several days for ricinoleic acid and one day for oleic acid) and were then transferred to a snap vial. The nanoparticles were stable in both solvents for more than months. TEM images were taken by a JEOL JEM-2200FS apparatus operating at an accelerating voltage of 200 kV. Gold nanoparticles were observed by casting the solvent on a copper grid covered with amorphous carbon and were then washed by casting isopropanol on the grid and dried. The sample was cast on the grid for 810 minutes in order to obtain a clear image with enough particles to derive a size distribution. The washing and drying sequence was repeated several times to obtain a clear TEM image. Size distributions were analyzed using a free software ImageJ,¹⁵³⁾ counting more than at least 900 particles for one plot. Several TEM images taken from different parts of the grid were used to obtain the

A. SYNTHESIS OF GOLD NANOPARTICLES BY A VACUUM EVAPORATION METHOD

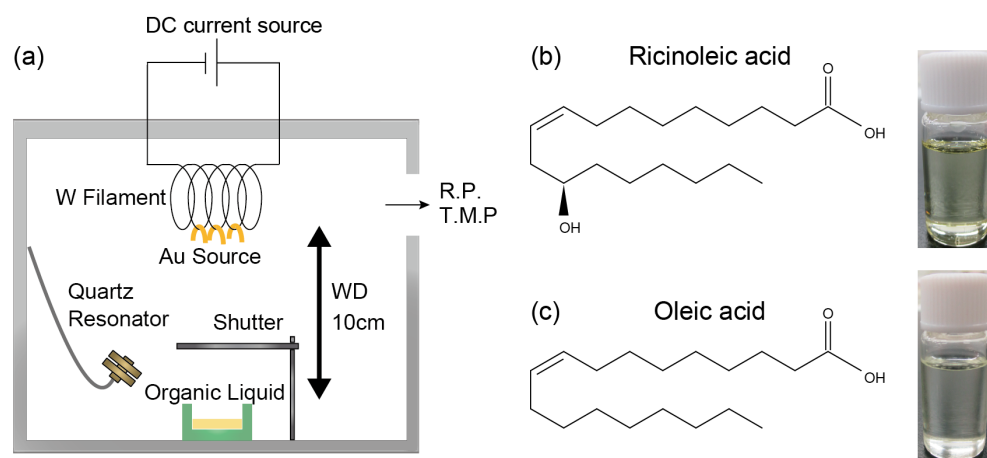


Figure A.1: (a) A schematic illustration of the experimental apparatus and (b), (c) structural formulas with photographs of ricinoleic and oleic acids. Both UFAs are transparent and ricinoleic acid has a light yellow color while oleic acid is colorless.

size distribution. SAXS measurements were taken using a RIGAKU Nanoviewer apparatus. The X-ray wavelengths were $\lambda = 1.54 \text{ \AA}$. The camera length was set to 1300 mm and the range of the measurement taken place was $0.14 < q < 3.2 \text{ nm}^{-1}$, where $q = \frac{4\pi \sin(\theta)}{\lambda}$, q is the scattering vector and 2θ is the scattering angle. Samples were measured in a handmade holder, using a 0.5 mm thick copper plate with a "U" shape cut off. Polyether Imide films (MITSUBISHI PLASTIC Superio UT Ftype) were glued on both surfaces of the copper plates to hold the sample. The holders were dried for at least a day in order to make sure the glue does not react with the sample. SAXS analysis was performed as previously reported from Hatakeyama et al.²¹¹⁾ Scattering profiles were obtained by the free software Fit2D.²¹²⁾ Experimental data were fitted using a RIGAKU Nano-Solver software. The SAXS measurements were conducted on the samples used for TEM observation and were demonstrated after the last TEM observations were carried out.

UV-Vis absorbance spectra were obtained using a Shimadzu UV-2600 spectrophotometer. The samples were measured in a glass cell with an optical length of 10 mm in a transmission mode using ricinoleic or oleic acid as a reference.

XPS measurements were conducted by a Shimadzu Kratos AXIS-ULTRA

DLD apparatus equipped with an Al K source. Samples were prepared by functionalizing Si substrates with 3-mercaptopropyltrimethoxysilane (MPTMS, purchased from Shin-Etsu Chemical Co., Ltd.). The substrates were immersed in a hot 5 mM toluene solution of MPTMS for 40 minutes. Then, the substrates were immersed in the solvents containing nanoparticles for several days to immobilize the nanoparticles on the substrate. Finally, the substrates were washed with 2-propanol and dried with N₂ flow. The spectra were calibrated by the C 1s peak (284.6 eV). The peak area of the Au 4f_{7/2} and 4f_{5/2} were fixed to 4 : 3.

A.3 Results and Discussion

Fig. A.2 shows a photograph of the fatty acids taken 5 minutes after VE deposition and when the samples have a homogeneous color. The behavior of the sample just after the deposition was different among the two solvents. In ricinoleic acid, black aggregates can be seen inside and on the surface of the solvent. The number of aggregates increased up to one hour after deposition and then started to dissolve into the solvent, showing a dark red color at the same time. The change in the color of the solvent is due to the SPR of nanoparticles indicating the emergence of nanoparticles in the range of 2100 nm were formed while the aggregates dissolved into the solvent. The aggregates continued to dissolve with time and turned into a homogeneous red or purple color after one week of deposition. In oleic acid, black aggregates formed on the surface of the solvent as in ricinoleic acid. Also, the solvent partially presented a brown color indicating nanoparticle formation has already occurred. As in ricinoleic acid, the aggregates shrunk with time and disappeared after one day of deposition. The samples are stable for more than months in atmospheric air and were resistant to water, a huge advantage compared to nanoparticles synthesized in ILs.²¹³⁾ Further details on the property with the progress of time are shown in Fig. A.3.

From visual observation, nanoparticles seem to form aggregates which then dissolved into the solvent. This is quite a surprising phenomenon since nanoparticles usually aggregate to lower the total surface energy. The phenomenon was investigated in more detail by taking TEM images by a function of time. Figs.

A. SYNTHESIS OF GOLD NANOPARTICLES BY A VACUUM EVAPORATION METHOD

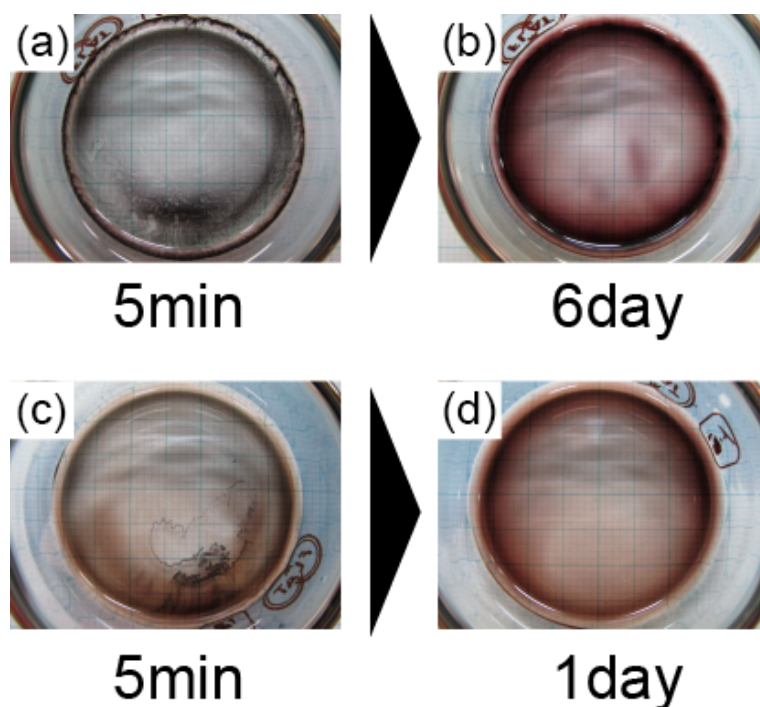


Figure A.2: Time-dependent photographs of UFAs. The photographs were taken (a) 5 minutes and (b) 1 week after deposition in ricinoleic acid and (c) 5 minutes and (d) 1 day after deposition in oleic acid. At 5 minutes after deposition, black aggregates were observed on the surface and inside the solvent in ricinoleic acid, while most of the aggregates seemed on the surface in oleic acid. At 1 week after deposition, both UFAs presented a homogeneous color. All photographs of the samples were taken on a cross-section paper.

A.4 and A.5 present the TEM images taken after the deposition and size distributions derived from the images of ricinoleic and oleic acids, respectively. The time represents when the TEM grid was fabricated after the deposition. It was assumed that the gold nanoparticles held on the amorphous carbon of the TEM grid are restricted from further growth (especially the growth of large aggregates). Some points should be noticed in the TEM observation. First, the growth of the nanoparticles during TEM observation can't be denied. Also, TEM observations only investigate a small part of the entire sample, so consistent results are needed from other measurements (SAXS and UV-Vis). Nevertheless, it is still a powerful method to directly observe the size and shape of the nanoparticles. In ricinoleic

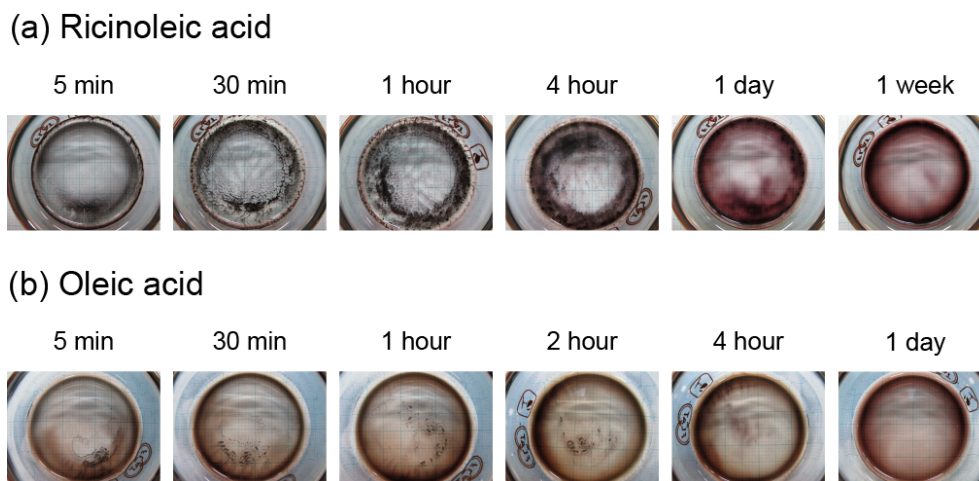


Figure A.3: Photographs of the sample after deposition as a function of time of (a) ricinoleic acid and (b) oleic acid. In ricinoleic acid, black aggregates continuously emerge until 1 hour. After 4 hours, the aggregates start to blur and the solvent slowly turns dark red indicating the formation of nanoparticles. It takes about a week to obtain a homogenous dark red color for the whole solvent. In oleic acid, black aggregates are formed on the surface and the solvent partially turns brown. The aggregates shrink with time and can't be confirmed 4 hours after deposition. After 1 day, a homogenous color is obtained and the color changed from brown to a slight red-brown color.

acid, aggregates in the size of several microns were observed 30 minutes after deposition. The aggregates were composed of spherical particles in the size of several nanometers and were partially coalesced, which are shown in Fig. A.4(b). It wasn't possible to obtain a size distribution for the 30-minute sample from the TEM images, since only a few number of particles were observed from the aggregate. However, the size scale of the particles composed of the aggregate agrees with the mean size estimated from TEM and SAXS measurements for 1-week samples (shown afterwards). This implies that nanoparticles are formed and growth completed within 30 minutes after deposition. This is a remarkable difference from gold nanoparticles synthesized by sputter deposition on ILs, where nanoparticle formation occurred for several hours to days.¹⁹⁵⁾ For the 4 hours and 1 week samples shown in Fig. 3(c) and (d), the aggregates became smaller and the nanoparticles became more dispersed. This behavior is consistent with

A. SYNTHESIS OF GOLD NANOPARTICLES BY A VACUUM EVAPORATION METHOD

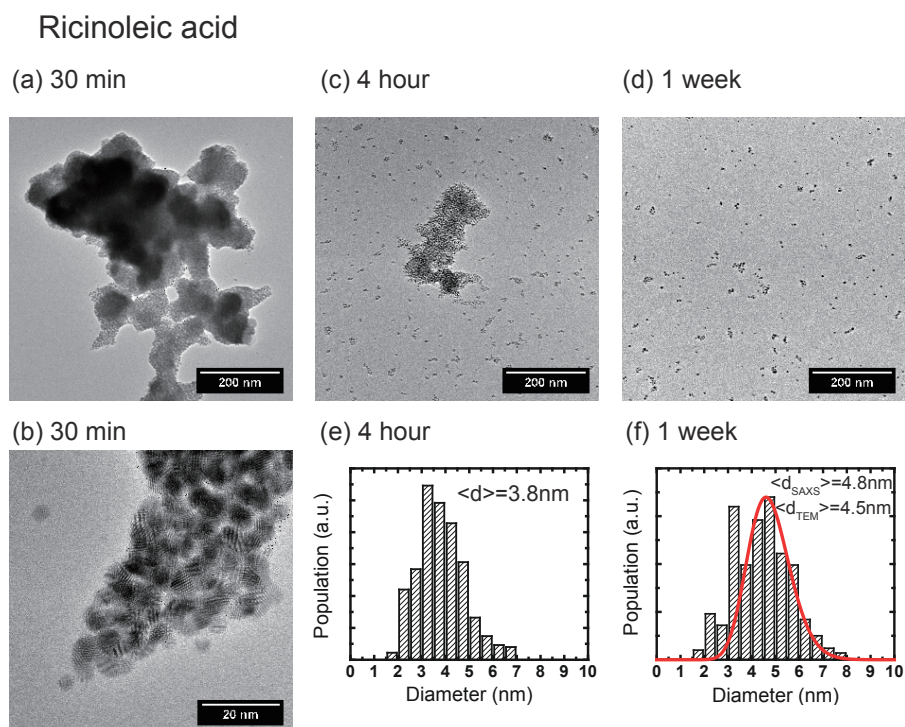


Figure A.4: TEM images of the gold nanoparticles formed in ricinoleic acid. The photographs (a), (c) and (e) are typical TEM images taken 30 minutes, 4 hours and 1 week after deposition, respectively. The magnification was set to 30 k times. The photograph (b) shows a 300 k time magnification TEM image of the same aggregate (a). Aggregates in the size of several microns were observed and the aggregates were composed of nanoparticles in the size of several nanometers. The graphs (e) and (f) display the size distribution derived from (c) and (d). Size distributions could not be obtained from (a) since individual nanoparticles were scarce. The red line shown in (f) stands for the size distribution obtained from SAXS measurements.

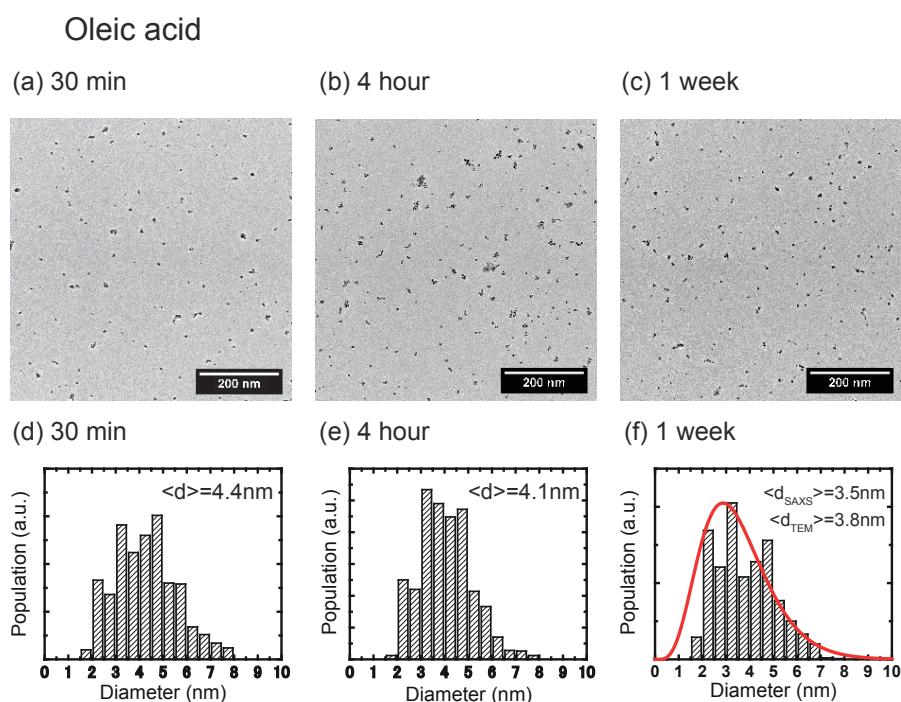


Figure A.5: TEM images of the gold nanoparticles formed in oleic acid. The photographs (a), (c) and (e) are typical TEM images taken 30 minutes, 4 hours and 1 week after deposition, respectively. The magnification was set to 30 k times. Huge aggregates in the size of several microns were not observed as in ricinoleic acid and the nanoparticles were mostly dispersed in all TEM images. The graphs (d), (e) and (f) display the size distribution derived from (a), (b) and (c), respectively. The red line shown in Fig. 3(f) stands for the size distribution obtained from SAXS measurements.

A. SYNTHESIS OF GOLD NANOPARTICLES BY A VACUUM EVAPORATION METHOD

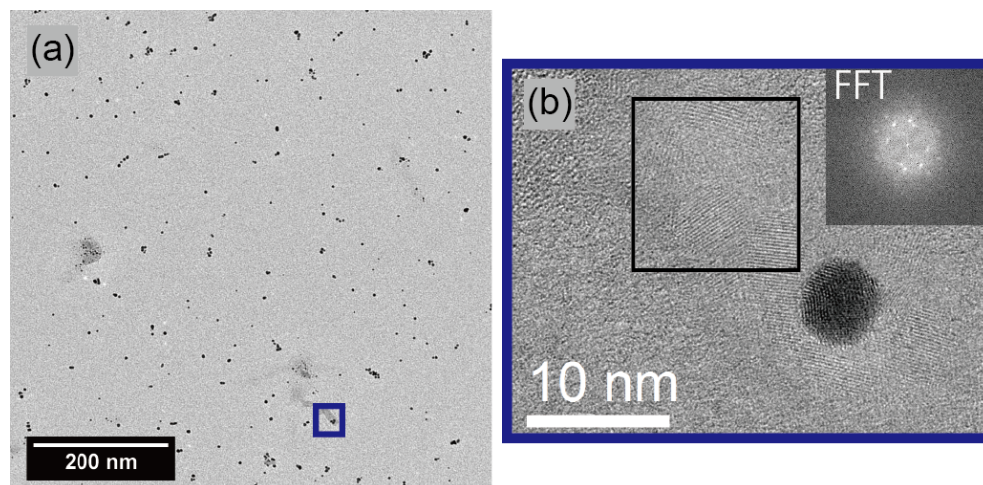


Figure A.6: TEM images of oleic acid. The magnification of the original TEM images were (a) 30k and (b) 300k. TEM images (a) and (b) were taken 10 minutes after deposition. In the TEM image (a), the nanoparticles were well dispersed and a contrast darker than the background can be recognized around some nanoparticles inside the blue square. (b) is the magnified view of the blue square shown in (a). Nanoparticles are observed and striped patterns can be seen around them. The inset in (b) stands for the fast Fourier transform (FFT) of the black square. Diffraction points can be seen from the FFT and therefore, the striped patterns are crystalline films, probably about a few monolayers. These films have also been observed in ricinoleic acid and should be residues of the aggregates formed on the surface of the solvent.

the visual observation where the aggregates looked blur and where a dark red color appeared. The average particle size was 3.8 nm after 4 hours and 4.5 nm after 1 week. The size distribution derived from Fig. 3(f) matched well with the SAXS measurements plotted as a red line in the same graph. On the other hand, in oleic acids, nanoparticles were mostly dispersed throughout the growth stage and only a few number of aggregates were found from the TEM images. The size distribution estimated from TEM images showed the mean size slightly decreased with time. However, the size distributions of nanoparticles in oleic acids are wider than those in ricinoleic acids. This indicates that nanoparticles in oleic acid, at least, hardly grew up after they were formed shortly after air exposure. The sized distributions obtained from Fig. 4(f) agree with the SAXS measurements.

In oleic acid, aggregates surrounded with a contrast different from the background were found (Fig. A.6). In higher magnifications, lattice planes could be observed and were confirmed by the diffraction patterns in the fast Fourier transformation. Since the lattice planes are transparent as the surrounding background, the lattice planes should indicate thin films of gold with only a few atomic layers. Thus, considering that small nanoparticles are found near the lattice planes, the thin films are residues of the aggregates formed on the surface of the solvent, just after deposition. This result suggests that the black aggregates visually observed on the surface of the solvent are actually thin films. The thin films were first formed on the surface of the solvent, then diffused into the solvent and turned into nanoparticles. These lattice planes were also observed in ricinoleic acid, which agree with the visual appearance of aggregates on the surface of ricinoleic acid, so that some of the gold atoms formed crystalline films although most of them diffused into the solvent. As mentioned before, it is crucial to gain a consistent result from other methods because TEM observations only obtain a micro view of the sample. Thus, UV-Vis measurements were carried out on the samples after deposition as a function of time.

Fig. 5 shows the UV-Vis spectra of both solvents as a function of time. In ricinoleic acid, a broad peak around 600 nm can be observed 30 minutes after deposition. Dispersed gold nanoparticles are known to show a characteristic SPR peak at around 520 nm.⁴⁾ The peak shift to longer wavelengths (red shift) and broadening of the peak are characteristic features of aggregation.¹⁹⁹⁾ After 1 day, the peak shifts back to around 520 nm and then shows a more pronounced peak corresponding to the continuous formation of nanoparticles. The spectra resemble those of dispersed gold nanoparticles and agree well with the TEM images showing that the aggregates shrink in time and the nanoparticles become dispersed. In oleic acid, on the other hand, the sample did not show a clear SPR peak 30 minutes after deposition. This supports the results of visual observation that revealed thin film formation in oleic acid. The SPR peak appears 4 hours after deposition and does not show a significant change after 1 day of deposition. This means that the thin films diffuse into the solvent and change into nanoparticles, and the phenomenon is mainly finished within 1 day. Again the spectra agree well

A. SYNTHESIS OF GOLD NANOPARTICLES BY A VACUUM EVAPORATION METHOD

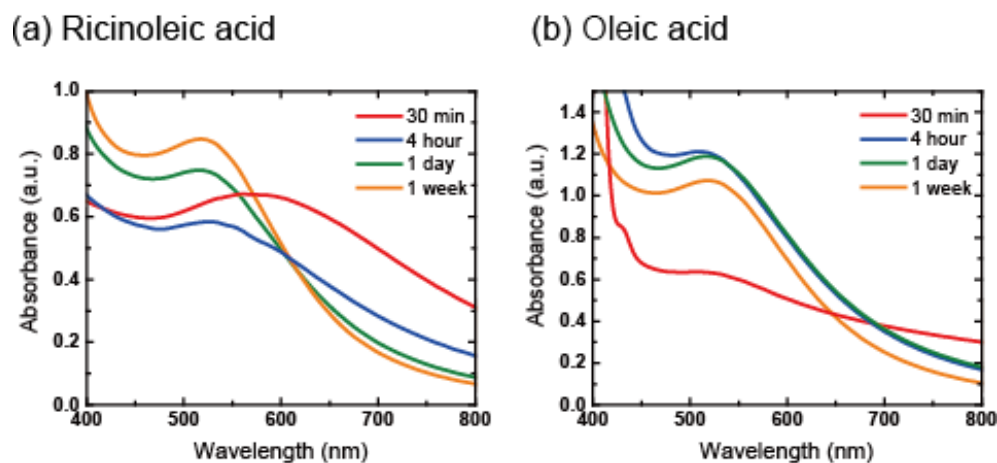


Figure A.7: Absorption spectra of both solvents as a function of time for (a) ricinoleic acid and (b) oleic acid. In ricinoleic acid, a broad peak at around 600 nm was observed and then shifted to at around 520 nm after 4 hours of deposition. This reflects the transfer from an aggregate to individual nanoparticles. In oleic acid, a clear peak cannot be confirmed 30 minutes after deposition. A peak around 520 nm was observed after 4 hours of deposition, reflecting the transfer from thin films to nanoparticles.

with the TEM observations. Hence, the microscopic view of the growth scheme can be applied to the whole sample.

Evidence of a growth phase on the surface questions us whether the deposition rate has an impact on the growth scheme. According to the classical nucleation theory, the gold atoms deposited on the surface migrate around and collide with each other, forming an embryo. While most of the embryos fall apart due to their unstableness, some of them continue to grow and form a nucleus. So, the deposition rate should have a critical impact since it should enhance the frequency of collisions and formation of the nucleus. Fig. A.8 shows the size distribution obtained by SAXS measurements where the VE was carried out on several deposition rates. Against the earlier hypothesis, a clear correlation with the size distribution and the deposition rate wasn't found. The mean size was around 4 nm in both solvents. A clear correlation was not observed between the size distribution and the deposition rate, so instead of the kinetic energy of the evaporated gold atoms, the interaction between the solvent and gold nanoparticles plays a

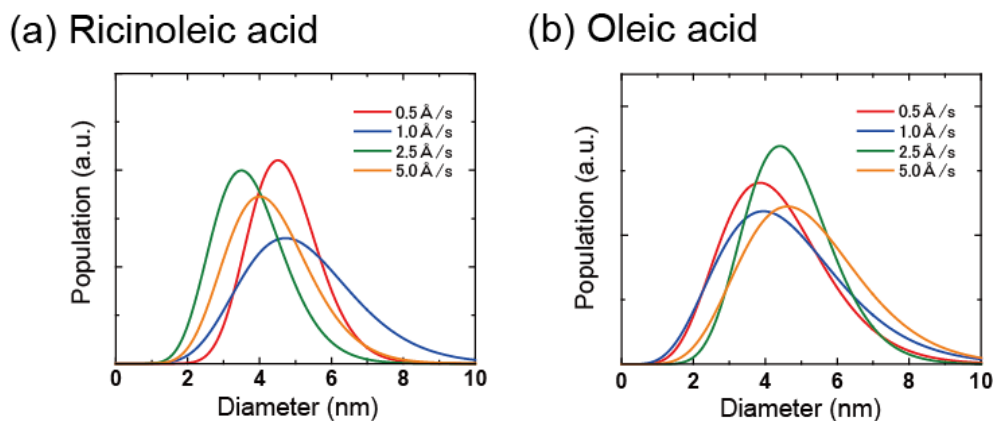


Figure A.8: Size distribution of gold nanoparticles synthesized in (a) ricinoleic and (b) oleic acid, obtained by SAXS measurements. Deposition rates were changed from 0.5 Å/s to 5.0 Å/s. Clear correlations between the deposition rate and size distribution could not be recognized.

decisive role in the formation of gold nanoparticles.

The difference between aggregation and thin film formation are consistent with earlier reports. Wender et al. sputtered silver onto vegetable oils like castor and canola oil.²⁰²⁾ The synthesis of nanoparticle was observed in castor oil while thin film formation occurred in canola oil when the accelerating voltage was low. They concluded that the composition of the fatty acid decided the behavior of the growth scheme: castor oil is mainly composed of ricinoleic acid (87%), which possesses hydroxyl groups while canola oil is composed of oleic and linoleic acid (oleic acid 48%, linoleic acid 32%) where there are no additional function groups. They suggested that the hydroxyl groups strongly interact with the gold atoms limiting their migration, resulting in the formation of nanoparticles while there were no such strong interactions in canola oil compositions and atoms diffused on the oil surface to form thin films. A recent report also pointed out the strong interaction between gold atoms and hydroxyl group functionalized ILs.¹⁹⁷⁾ ILs with hydroxyl groups confined the gold atoms on the surface of the IL and nanoparticle formation occurred on the surface. Although the two reports show different results where the nanoparticles are formed, they both suggest the strong interaction between hydroxyl groups and sputtered atoms. The results show the same trend and actually verifies Wenders report. Further research on

A. SYNTHESIS OF GOLD NANOPARTICLES BY A VACUUM EVAPORATION METHOD

the structure of the vacuum/liquid interface needs to be conducted in order to elucidate the difference of the growth scheme in ricinoleic and oleic acids.

It was also found that exposing the sample to air triggers the dispersion or formation of the nanoparticles in the UFAs as shown in Fig. A.9. This phenomenon was confirmed by keeping the sample in a vacuum (under 0.05 Torr) for a day and then exposed to the atmosphere. Black aggregates remained in both solvents and the color change occurred after the sample was exposed to air, indicating that progress of time did not trigger the phenomenon. Therefore, control experiments were conducted to identify the cause. After the VE, the apparatus was (1) kept in vacuum (under 0.05 Torr), (b) vented with N₂ gas, or (c) vented with a mixed gas of O₂ + He (O₂ :He = 7 : 3) and kept for a day. When the apparatus was kept in vacuum or vented with N₂ gas, black aggregates remained and no color change was observed in both solvents. When venting with O₂ mixed gas, however, the aggregates disappeared and the color change was appreciated, showing that oxygen triggers the dispersion of nanoparticles. The oxidation of gold nanoparticles will be discussed in the following XPS analysis.

The XPS spectra for Au 4f, S 2p and O 1s are shown in Figs. A.10, A.11 and A.12, respectively. The XPS spectra of Au 4f for the gold nanoparticles showed 2 peaks around 84.0 eV and 87.7 eV, which represent Au 4f_{7/2} and Au 4f_{5/2} peaks in bulk gold.^{214,215)} Additional peaks of the spectra with a positive shift of 0.8 eV from the bulk gold peaks were found, which should be assigned to the Au-S bond, induced by the mercapto group in the MPTMS. When gold nanoparticles are oxidized, the surface turns into Au₂O₃ where the Au 4f shows a positive shift of about 1.8 eV.²¹⁵⁾ It also should be mentioned that prior XPS research on gold nanoparticles immobilized by thiol monolayers showed small positive 1.7 eV shift peaks, which they concluded to partial charging in the sample.²¹⁶⁾ Thus, it can't be decided from the spectra whether the peaks arise from oxidized gold atoms or charging. However, even if it is assumed that the peak arises from oxidation, it is less than 5% of the overall Au signal. Thus, it was concluded that the oxidation of gold nanoparticles are negligible and can't be the major factor inducing the change from aggregate to nanoparticle or thin film to nanoparticle.

The S 2p spectra show 3 peaks. The broad peak around 168 eV arises from the oxidation of sulfur.²¹⁷⁾ The peak appears in self assembled monolayers (SAMs)

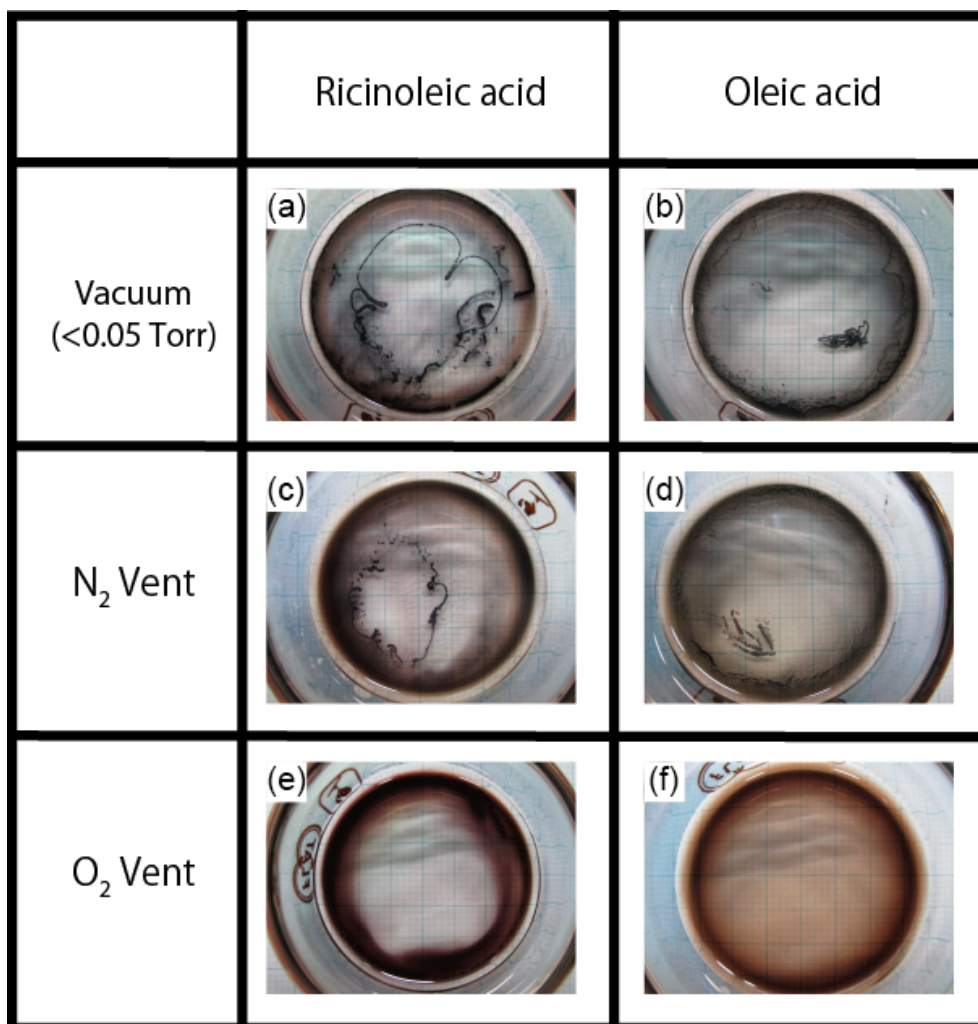


Figure A.9: Visual observations of the influence of gas or vacuum exposure to the samples. Control experiments were conducted as follows. After the deposition, each solvent was aged under 3 different atmosphere for a day: (a), (b) vacuum under 0.05 Torr, (c), (d) 1 atm nitrogen gas for and (e), (f) 1 atm oxygen gas mixed with helium (O₂ : He = 7:3). The samples were taken out the next day. The vacuum was never broken during the experiment until the samples were taken out. Black aggregates remained when left in vacuum and vented with nitrogen for both solvents. However, the aggregates disappeared when the apparatus was vented with the oxygen mixed gas. Considering helium is an inert gas, the oxygen should have triggered the phenomenon.

A. SYNTHESIS OF GOLD NANOPARTICLES BY A VACUUM EVAPORATION METHOD

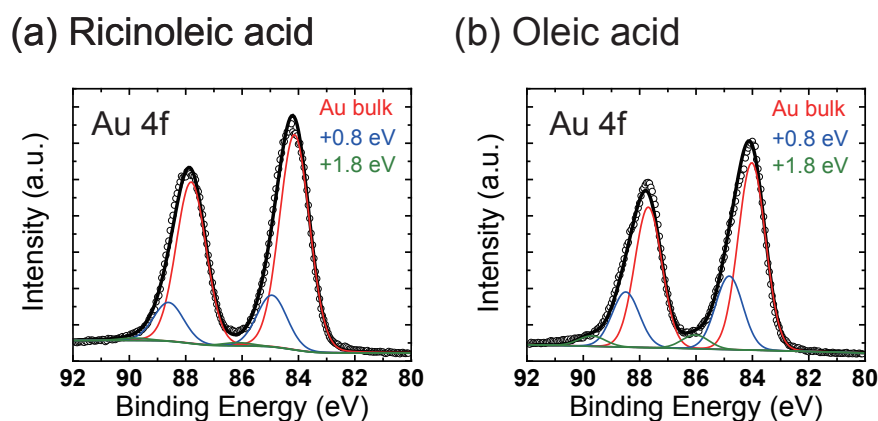


Figure A.10: XPS spectra of Au 4f measured from gold nanoparticles synthesized in (a) ricinoleic acid and (b) oleic acid. The red and blue peaks are assigned for bulk gold and Au-S bonds, respectively. The green peak occurs from partially charged particles or oxidized gold atoms.

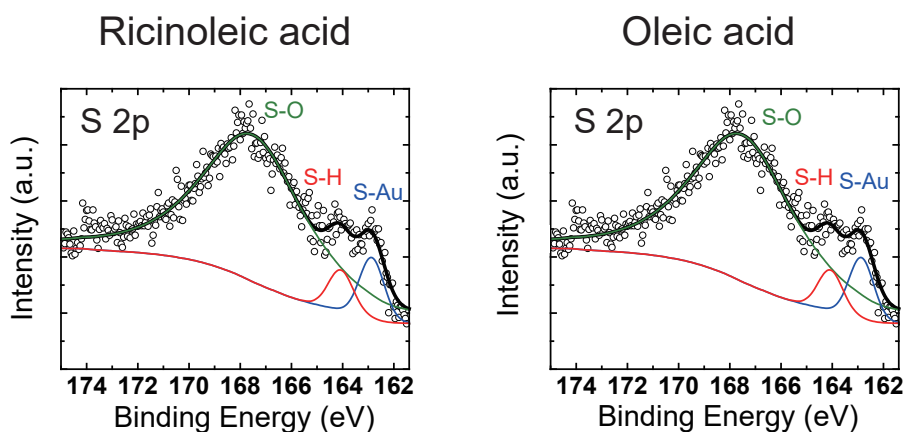


Figure A.11: XPS spectra of S 2p measured from gold nanoparticles synthesized in (a) ricinoleic acid and (b) oleic acid. The green, red and blue peaks arise from oxidized sulfur, reduced sulfur and Au-S bonds, respectively.

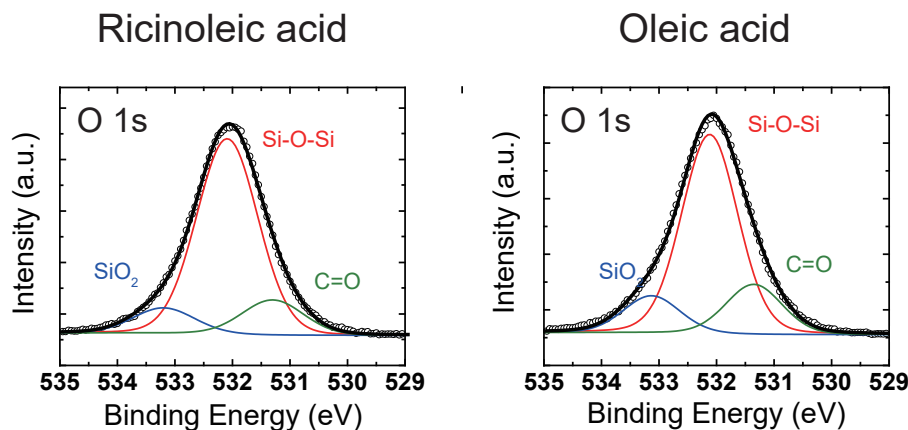


Figure A.12: XPS spectra of O 1s measured from gold nanoparticles synthesized in (a) ricinoleic acid and (b) oleic acid. The red, blue and green peaks arise from Si-O-Si bonds, SiO₂ and COOH, respectively.

as in this experiment, where the SAMs are exposed to the air. 2 peaks at 164.0 eV and 162.8 eV are also recognized. The 164.0 eV peak represents from reduced sulfur (S-H bond) and the 162.8 eV peak arises from the Au-S bond,⁶ which is consistent with the Au 4f spectra. The peak values differ from prior research because the S 2p signals are poor.

The O 1s signals also show 3 peaks. The main peak around 532 eV represents the siloxane bond formed between the MPTMS and the silicon substrate.²¹⁸⁾ This was evidenced since the same peak was found in MPTMS monolayers without immobilizing gold nanoparticles. The 533.2 eV peak represents the naturally oxidized SiO₂ surface⁸ and the 531.3 eV peak represents the carboxyl group of the UFAs.²¹⁹⁾ Also, the O 1s peak in Au₂O₃ has a peak around 530 eV,²²⁰⁾ which is out of the range in this spectra. Therefore, there is no evidence of oxidation in the O 1s spectra.

Thus, it was concluded that the oxidation of the gold nanoparticles were negligible from the XPS analysis. UFAs are known to be unstable and easily get oxidized. Hence, the oxidization of the UFAs should have triggered the phenomenon.

Finally, the reason why the aggregates formed in the solvent disperse after

A. SYNTHESIS OF GOLD NANOPARTICLES BY A VACUUM EVAPORATION METHOD

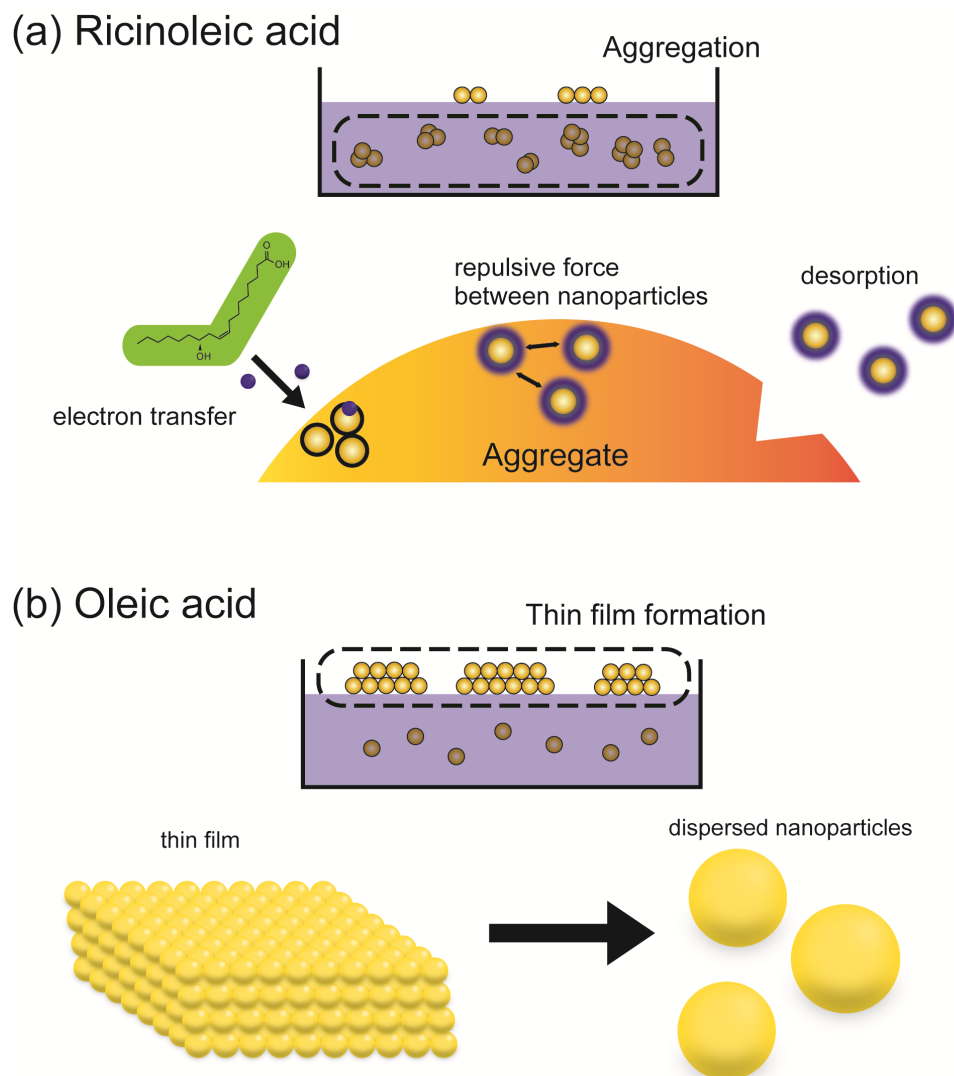


Figure A.13: Schematic illustration of the behavior of the aggregates in (a) ricinoleic acid and (b) oleic acid. The navy blue spheres represent electrons. (a) and (b) were mainly observed in ricinoleic acid and oleic acid, respectively. (a) UFA molecules get oxidized and electrons were transferred to the surface of the aggregate. The nanoparticles positioned on the surface get negatively charged and repulsive forces arise between them. Further electron transfer causes desorption of the nanoparticles from the aggregate. (b) Crystalline thin films form on the UFA after deposition. The films become stimulated by the electrons induced by the oxidation of the UFA and diffuse into the solvent changing into nanoparticles.

A.3 Results and Discussion

oxygen exposure will be discussed. Although aggregates in the size of microns were mostly observed in ricinoleic acid and lattice planes in oleic acid, counter-examples were also found. A schematic illustration of the phenomenon is shown in Fig. 7. The stability of colloids is usually described by the DLVO theory, taking into account the attractive van der Waals force and the repulsive force between the surface potentials of the colloids.^{221,222)} Therefore, the transition from an aggregate to a disperse state should be due to an increase in the surface potential of the nanoparticles. It is clear in this study that the samples are sensitive to oxygen, which triggers the phenomenon, letting us assume that the oxidation of the ricinoleic acid stimulates the transition. Gold nanoparticles are a well-known catalyst for oxidizing organic materials and they get redox when the reaction occurs. As a result, electrons are transferred from the ricinoleic acid to the gold nanoparticles.²²³⁾ Novo et al. reported the electron transfer from ascorbic acid to gold nanocrystals resulting from the oxidation of ascorbic acid.²²⁴⁾ The same phenomenon occurred in this experiment, where electrons transferred from the ricinoleic acid to the gold nanoparticles, resulting in an increase in the surface potential.²²⁵⁾ Nanoparticles positioned on the surface of the aggregates get charged and break away. Thus, the aggregates shrink and finally become individual particles or very small aggregates.

In oleic acid, thin films formed on the surface of the solvent and diffused inside (induced by the oxygen exposure) which transferred into nanoparticles. Also in this case, the surface structure again plays a role in this scheme. As mentioned before, the double bond of the UFAs is known to be unstable and easily oxidized. The oxidation of the double bond induced the diffusion of the thin films to diffuse inside the solvent. It is hard to say precisely what triggered the diffusion but the correlation can be seen by the fact that thin film formation was hardly seen when "old" oleic acids were used (about a year from the first time used), where more double bonds should be oxidized, prior to use. The thin films in the solvent should transfer into nanoparticles to decrease the total surface energy, which is higher in a 2D film than a sphere. Thus, the oxidation of the solvent induced the transfer from thin films to nanoparticles.

A. SYNTHESIS OF GOLD NANOPARTICLES BY A VACUUM EVAPORATION METHOD

A.4 Summary

Gold nanoparticles were synthesized by VE methods in ricinoleic acid and oleic acid. From TEM images, gold nanoparticles first formed aggregates in ricinoleic acid and then shrunk by time, forming individual nanoparticles. In oleic acid, the nanoparticles were in a dispersed state. Lattice planes were observed in both UFAs, which were residues of the thin films formed on the surface of the solvents, which is evidence of a growth stage on the surface in VE methods. UV-Vis spectra confirmed the behavior observed in TEM images. The difference of the behaviors of ricinoleic and oleic acids are consistent with prior research and suggests that the structure of the vacuum/liquid interface has a strong impact on the growth scheme. Oxygen triggers the phenomenon above by oxidizing the solvent and was confirmed by XPS measurements, which ruled out the possibility of the oxidation of surface gold atoms. The samples were resistive to water and were stable for more than months. Thus, the VE method should be a promising candidate for industrial applications.

References

- [1] R. P. Feynman, “There’s Plenty of Room at the Bottom”, *Eng. Sci.* (1960) **23** 22–36.
- [2] G. E. Moore, “Cramming more components onto integrated circuits”, *Electronics* (1965) **38**.
- [3] S. M. Sze and K. K. Ng, *Physics of Semiconductor Devices*, John Wiley & Sons, Ltd (2006).
- [4] S K Ghosh and T Pal, “Interparticle Coupling Effect on the Surface Plasmon Resonance of Gold Nanoparticles: From Theory to Applications”, *Chem. Rev.* (2007) **107** 4797–4862.
- [5] A. Corma and H. Garcia, “Supported gold nanoparticles as catalysts for organic reactions”, *Chem. Soc. Rev.* (2008) **37** 2096–2126.
- [6] Y. Yamamoto, T. Miura, M. Suzuki, N. Kawamura, H. Miyagawa, T. Nakamura, K. Kobayashi, T. Teranishi and H. Hori, “Direct observation of ferromagnetic spin polarization in gold nanoparticles”, *Phys. Rev. Lett.* (2004) **93** 116801.
- [7] A. E. Goode, A. E. Porter, M. M. Kłosowski, M. P. Ryan, S. Heutz, and D. W. McComb, “Analytical transmission electron microscopy at organic interfaces”, *Curr. Opin. Solid State Mater. Sci.* (2017) **21** 55–67.
- [8] M. L. Taheri, E. A. Stach, I. Arslan, P. A. Crozier, B. C. Kabijs, T. LaGrange, A. M. Minor, S. Takeda, M. Tanase, J. B. Wagner, and R. Sharma, “Current status and future directions for in situ transmission electron microscopy”, *Ultra-microscopy* (2016) **170** 86–95.
- [9] W. A. Hofer, A. S. Foster, and A. L. Shluger, “Theories of scanning probe microscopes at the atomic scale”, *Rev. Mod. Phys.* (2003) **75** 1287–1331.

REFERENCES

- [10] P. T. Lillehei and L. A. Bottomely, “Scanning probe microscopy”, *Anal. Chem.* (2000) **72** 189R–196R.
- [11] F. J. Giessibl, “Advances in atomic force microscopy”, *Rev. Mod. Phys.* (2003) **75** 949–983.
- [12] Y. F. Dufrêne, T. Ando, R. Garcia, D. Alsteens, D. Martinez-Martin, A. Engel, C. Gerber, and D. J. Müller, “Imaging modes of atomic force microscopy for application in molecular and cell biology”, *Nat. Nanotechnol.* (2017) **12** 295–307.
- [13] G. Binnig, H. Rohrer, C. H. Gerber, and E. Weibel, “Surface Studies by Scanning Tunneling Microscopy”, *Phys. Rev. Lett.* (1982) **49** 57–61.
- [14] G. Binnig and H. Rohrer, “Scanning Tunneling Microscopy from Birth to Adolescence”, *Rev. Mod. Phys.* (1987) **59** 615–629.
- [15] M. Nonnenmacher, M. P. O’Boyle, and H. K. Wickramasinghe, “Kelvin probe force microscopy”, *Appl. Phys. Lett.* (1991) **58** 2921–2923.
- [16] Y. Martin and H. K. Wickramasinghe, “Magnetic imaging by force microscopy” with 1000 Å resolution”, *Appl. Phys. Lett.* (1987) **50** 1455–1457.
- [17] S. V. Kalinin and D. A. Bonnell, “Scanning impedance microscopy of electroactive interfaces”, *Appl. Phys. Lett.* (2001) **78** 1306–1308.
- [18] A. Segmijller, “Characterization of Epitaxial Films By Grazing- Incidence X-Ray Diffraction”, *Thin Solid Films* (1987) **154** 33–42.
- [19] Y.-F. Liew and G.-C. Wang, “High resolution low energy electron diffraction characterization of reconstructed Au(001) surfaces”, *Surf. Sci.* (1990) **227** 190–196.
- [20] G. Binnig, H. Rohrer, Ch Gerber, and E. Weibel, “(7×7) Reconstruction on Si(111) Resolved in Real Space”, *Phys. Rev. Lett.* (1983) **50** 120–123.
- [21] T. Fukuma, K. Kobayashi, K. Matsushige, and H. Yamada, “True atomic resolution in liquid by frequency-modulation atomic force microscopy”, *Appl. Phys. Lett.* (2005) **87** 034101.
- [22] K. Voitchovsky, J. J. Kuna, S. A. Contera, E. Tosatti, and F. Stellacci, “Direct mapping of the solid-liquid adhesion energy with subnanometre resolution”, *Nat. Nanotechnol.* (2010) **5** 401–405.

REFERENCES

- [23] K. Kimura, S. Ido, N. Oyabu, K. Kobayashi, Y. Hirata, T. Imai, and H. Yamada, “Visualizing water molecule distribution by atomic force microscopy”, *J. Chem. Phys.* (2010) **132** 194705.
- [24] K. Kobayashi, N. Oyabu, K. Kimura, S. Ido, K. Suzuki, T. Imai, K. Tagami, M. Tsukada, and H. Yamada, “Visualization of hydration layers on muscovite mica in aqueous solution by frequency-modulation atomic force microscopy”, *J. Chem. Phys.* (2013) **138** 184704.
- [25] M. Gauthier, T. J. Carney, A. Grimaud, L. Giordano, N. Pour, H.-H. Chang, D. P. Fenning, S. F. Lux, O. Paschos, C. Bauer, F. Maglia, S. Lupart, P. Lamp, and Y. Shao-Horn, “Electrode/Electrolyte Interface in Li-Ion Batteries: Current Understanding and New Insights”, *J. Phys. Chem. Lett.* (2015) **6** 4653–4672.
- [26] F. Lin, Y. Liu, X. Yu, L. Cheng, A. Singer, O. G. Shpyrko, H. L. Xin, N. Tamura, C. Tian, T. C. Weng, X. Q. Yang, Y. S. Meng, D. Nordlund, W. Yang, and M. M. Doeff, “Synchrotron X-ray Analytical Techniques for Studying Materials Electrochemistry in Rechargeable Batteries”, *Chem. Rev.* (2017) **117** 13123–13186.
- [27] F. Tao and P. A. Crozier, “Atomic-Scale Observations of Catalyst Structures under Reaction Conditions and during Catalysis”, *Chem. Rev.* (2016) **116** 3487–3539.
- [28] B. Van Grinsven, K. Eersels, O. Akkermans, S. Ellermann, A. Kordek, M. Peeters, O. Deschaume, C. Bartic, H. Diliën, E. Steen Redeker, P. Wagner, and T. J. Cleij, “Label-Free Detection of *Escherichia coli* Based on Thermal Transport through Surface Imprinted Polymers”, *ACS Sens.* (2016) **1** 1140–1147.
- [29] A. Yamakata, E. Soeta, T. Ishiyama, M. Osawa, and A. Morita, “Real-time observation of the destruction of hydration shells under electrochemical force”, *J. Am. Chem. Soc.* (2013) **135** 15033–15039.
- [30] F. Mallamace, C. Corsaro, D. Mallamace, P. Baglioni, H. E. Stanley, and S. H. Chen, “A possible role of water in the protein folding process”, *J. Phys. Chem. B* (2011) **115** 14280–14294.
- [31] D. Laage, T. Elsaesser, and J. T. Hynes, “Water dynamics in the hydration shells of biomolecules”, *Chem. Rev.* (2017) **117** 10694–10725.

REFERENCES

- [32] P. G. Vekilov, “What determines the rate of growth of crystals from solution?”, *Cryst. Growth Des.* (2007) **7** 2796–2810.
- [33] U. Anand, J. Lu, D. Loh, Z. Aabdin, and U. Mirsaidov, “Hydration Layer-Mediated Pairwise Interaction of Nanoparticles”, *Nano Lett.* (2016) **16** 786–790.
- [34] A. Uysal, M. Chu, B. Stripe, A. Timalisina, S. Chattopadhyay, C. M. Schlepütz, T. J. Marks, and P. Dutta, “What x rays can tell us about the interfacial profile of water near hydrophobic surfaces”, *Phys. Rev. B* (2013) **88** 35–37.
- [35] M. Mezger, F. Sedlmeier, D. Horinek, H. Reichert, D. Pontoni, and H. Dosch, “On the origin of the hydrophobic water gap: An X-ray reflectivity and MD simulation study”, *J. Am. Chem. Soc.* (2010) **132** 6735–6741.
- [36] D. Schweddel, T. Hayashi, R. Dahint, A. Pertsin, M. Grunze, R. Steitz, and F. Schreiber, “Interaction of Water with self-assembled monolayers: Neutron reflectivity measurements of the water density in the interface region.”, *Langmuir* (2003) **19** 2284–2293.
- [37] S. Roy and D. K. Hore, “Simulated structure and nonlinear vibrational spectra of water next to hydrophobic and hydrophilic solid surfaces”, *J. Phys. Chem. C* (2012) **116** 22867–22877.
- [38] C. Howell, R. Maul, W. Wenzel, and P. Koelsch, “Interactions of hydrophobic and hydrophilic self-assembled monolayers with water as probed by sum-frequency-generation spectroscopy”, *Chem. Phys. Lett.* (2010) **494** 193–197.
- [39] E. Tyrode and J. F. D. Liljeblad, “Water structure next to ordered and disordered hydrophobic silane monolayers: A vibrational sum frequency spectroscopy study”, *J. Phys. Chem. C* (2013) **117** 1780–1790.
- [40] S. Singla, E. Anim-Danso, A. E. Islam, Y. Ngo, S. S. Kim, R. R. Naik, and A. Dhinojwala, “Insight on Structure of Water and Ice next to Graphene Using Surface-Sensitive Spectroscopy”, *ACS Nano* (2017) **11** 4899–4906.
- [41] J. N. Israelachvili and R. M. Pashley, “Molecular layering of water at surfaces and origin of repulsive hydration forces”, *Nature* (1983) **306** 249–250.
- [42] M. Kasuya, T. Sogawa, T. Masuda, T. Kamijo, K. Uosaki, and K. Kurihara, “Anion Adsorption on Gold Electrodes Studied by Electrochemical Surface Forces Measurement”, *J. Phys. Chem. C* (2016) **120** 15986–15992.

REFERENCES

- [43] T. Fukuma, Y. Ueda, S. Yoshioka, and H. Asakawa, “Atomic-Scale distribution of water molecules at the mica-Water interface visualized by three-Dimensional scanning force microscopy”, *Phys. Rev. Lett.* (2010) **104** 016101.
- [44] D. Martin-Jimenez, E. Chacon, P. Tarazona, and R. Garcia, “Atomically resolved three-dimensional structures of electrolyte aqueous solutions near a solid surface”, *Nat. Commun.* (2016) **7** 12164.
- [45] H. Söngen, M. Nalbach, H. Adam, and A. Kühnle, “Three-dimensional atomic force microscopy mapping at the solid-liquid interface with fast and flexible data acquisition”, *Rev. Sci. Instrum.* (2016) **87** 063704.
- [46] F. Ito, K. Kobayashi, P. Spijker, L. Zivanovic, K. Umeda, T. Nurmi, N. Holmberg, K. Laasonen, A. S. Foster, and H. Yamada, “Molecular resolution of the water interface at an alkali halide with terraces and steps”, *J. Phys. Chem. C* (2016) **120** 19714–19722.
- [47] T. Fukuma, M. J. Higgins, and S. P. Jarvis, “Direct imaging of individual intrinsic hydration layers on lipid bilayers at Ångstrom resolution”, *Biophys. J.* (2007) **92** 3603–3609.
- [48] H. Asakawa, S. Yoshioka, K. I. Nishimura, and T. Fukuma, “Spatial distribution of lipid headgroups and water molecules at membrane/water interfaces visualized by three-dimensional scanning force microscopy”, *ACS Nano* (2012) **6** 9013–9020.
- [49] E. T. Herruzo, H. Asakawa, T. Fukuma, and R. Garcia, “Three-dimensional quantitative force maps in liquid with 10 piconewton, angstrom and sub-minute resolutions”, *Nanoscale* (2013) **5** 2678–2685.
- [50] K. Kuchuk and U. Sivan, “Hydration Structure of a Single DNA Molecule Revealed by Frequency-Modulation Atomic Force Microscopy”, *Nano Lett.* (2018) **18** 2733–2737.
- [51] J. N. Israelachvili, *Solvation, Structural, and Hydration Forces*, Academic Press 3 edition (2011).
- [52] G. Binnig and C. F. Quate, “Atomic Force Microscope”, *Phys. Rev. Lett.* (1986) **56** 930–933.
- [53] F. Ohnesorge and G. Binnig, “Atomic Resolution of Silicon(111)7x7 by Atomic Force Microscopy Through Repulsive and Attractive Forces”, *Science* (1993) **260** 1451–1456.

REFERENCES

- [54] T. R. Albrecht and C. F. Quate, “Atomic resolution imaging of a nonconductor by atomic force microscopy”, *J. Appl. Phys.* (1987) **62** 2599–2602.
- [55] T. R. Albrecht, P. Grütter, D. Horne, and D. Rugar, “Frequency modulation detection using high-Q cantilevers for enhanced force microscope sensitivity”, *J. Appl. Phys.* (1991) **69** 668–673.
- [56] Y. Martin, C. C. Williams, and H. K. Wickramasinghe, “Atomic force microscope-force mapping and profiling on a sub 100-Å scale”, *J. Appl. Phys.* (1987) **61** 4723–4729.
- [57] M. Shibata, H. Yamashita, T. Uchihashi, H. Kandori, and T. Ando, “High-speed atomic force microscopy shows dynamic molecular processes in photoactivated bacteriorhodopsin”, *Nat. Nanotechnol.* (2010) **5** 208–212.
- [58] N. Kodera, D. Yamamoto, R. Ishikawa, and T. Ando, “Direct imaging of walking myosin V by high-speed atomic force microscopy”, *Nature* (2018) **468** 72–76.
- [59] A. Miyagi, C. Chipot, M. Rangl, and S. Scheuring, “High-speed atomic force microscopy shows that annexin V stabilizes membranes on the second timescale”, *Nat. Nanotechnol.* (2016) **11** 783–790.
- [60] N. Umeda, S. Ishizaki, and H. Uwai, “Scanning attractive force microscope using photothermal vibration”, *J. Vac. Sci. Technol.* (1991) **9** 1318.
- [61] D. Kiracofe, K. Kobayashi, A. Labuda, A. Raman, and H. Yamada, “High efficiency laser photothermal excitation of microcantilever vibrations in air and liquids”, *Rev. Sci. Instrum.* (2011) **82** 013702.
- [62] G. Meyer and N. M. Amer, “Novel optical approach to atomic force microscopy”, *Appl. Phys. Lett.* (1988) **53** 1045–1047.
- [63] L. Gross, F. Mohn, N. Moll, P. Liljeroth, and G. Meyer, “The Chemical Structure of a Molecule Resolved by Atomic Force Microscopy”, *Science* (2009) **325** 1110–1114.
- [64] B. Schuler, G. Meyer, D. Peña, O. C. Mullins, and L. Gross, “Unraveling the Molecular Structures of Asphaltenes by Atomic Force Microscopy”, *J. Am. Chem. Soc.* (2015) **137** 9870–9876.
- [65] A. Shiotari and Y. Sugimoto, “Ultrahigh-resolution imaging of water networks by atomic force microscopy”, *Nat. Commun.* (2017) **8** 14313.

REFERENCES

- [66] S. Kawai, S. Saito, S. Osumi, S. Yamaguchi, A. S. Foster, P. Spijker, and E. Meyer, “Atomically controlled substitutional boron-doping of graphene nanoribbons”, *Nat. Commun.* (2015) **6** 8098.
- [67] S. Zint, D. Ebeling, T. Schlöder, S. Ahles, D. Mollenhauer, H. A. Wegner, and A. Schirmeisen, “Imaging Successive Intermediate States of the On-Surface Ullmann Reaction on Cu(111): Role of the Metal Coordination”, *ACS Nano* (2017) **11** 4183–4190.
- [68] F. J. Giessibl, “Forces and frequency shifts in atomic-resolution dynamic-force microscopy”, *Phys. Rev. B* (1997) **56** 16010–16015.
- [69] F. J. Giessibl, “A direct method to calculate tip-sample forces from frequency shifts in frequency-modulation atomic force microscopy”, *Appl. Phys. Lett.* (2001) **78** 123.
- [70] J. E. Sader and S. P. Jarvis, “Accurate formulas for interaction force and energy in frequency modulation force spectroscopy”, *Appl. Phys. Lett.* (2004) **84** 1801–1803.
- [71] J. Welker, E. Illek, and F. J. Giessibl, “Analysis of force-deconvolution methods in frequency-modulation atomic force microscopy”, *Beilstein J. Nanotechnol.* (2012) **3** 238–248.
- [72] V. Adrian Parsegian, *Van der Waals Forces: A Handbook for Biologists, Chemists, Engineers, and Physicists*, Cambridge University Press (2005).
- [73] B. Derjaguin, “Untersuchungen über die reibung und adhäsion, iv”, *Kolloid-Zeitschrift* (1934) **69** 155–164.
- [74] I. Langmuir, “The role of attractive and repulsive forces in the formation of tactoids, thixotropic gels, protein crystals and coacervates”, *J. Chem. Phys.* (1938) **6** 873–896.
- [75] K. Miyazawa, N. Kobayashi, M. Watkins, A. L. Shluger, K. Amano, and T. Fukuma, “A relationship between three-dimensional surface hydration structures and force distribution measured by atomic force microscopy”, *Nanoscale* (2016) **8** 7334–7342.
- [76] J. I. Kilpatrick, S. H. Loh, and S. P. Jarvis, “Directly probing the effects of ions on hydration forces at interfaces”, *J. Am. Chem. Soc.* (2013) **135** 2628–2634.

REFERENCES

- [77] T. Fukuma, B. Reischl, N. Kobayashi, P. Spijker, F. F. Canova, K. Miyazawa, and A. S. Foster, “Mechanism of atomic force microscopy imaging of three-dimensional hydration structures at a solid-liquid interface”, *Phys. Rev. B* (2015) **92** 155412.
- [78] M. Watkins and A. L. Shluger, “Mechanism of contrast formation in atomic force microscopy in water”, *Phys. Rev. Lett.* (2010) **105** 196101.
- [79] M. Watkins, M. L. Berkowitz, and A. L. Shluger, “Role of water in atomic resolution AFM in solutions”, *Phys. Chem. Chem. Phys.* (2011) **13** 12584–12594.
- [80] C. Narayanan and C. L. Dias, “Hydrophobic interactions and hydrogen bonds in β -sheet formation”, *J. Chem. Phys.* (2013) **139** 115103.
- [81] C. N. Pace, H. Fu, K. L. Fryar, J. Landua, S. R. Trevino, B. A. Shirley, M. M. N. Hendricks, S. Iimura, K. Gajiwala, J. M. Scholtz, and G. R. Grimsley, “Contribution of hydrophobic interactions to protein stability”, *J. Mol. Biol.* (2011) **408** 514–528.
- [82] K. Suzuki, N. Oyabu, K. Kobayashi, K. Matsushige, and H. Yamada, “Atomic-resolution imaging of graphite-water interface by frequency modulation atomic force microscopy”, *Appl. Phys. Express* (2011) **4** 125102.
- [83] I. Schlesinger and U. Sivan, “New information on the hydrophobic interaction revealed by frequency modulation afm”, *Langmuir* (2017) **33** 2485–2496.
- [84] I. Schlesinger and U. Sivan, “Three-dimensional characterization of layers of condensed gas molecules forming universally on hydrophobic surfaces”, *J. Am. Chem. Soc.* (2018) **140** 10473–10481.
- [85] Q. Du, E. Freysz, and Y. R. Shen, “Surface Vibrational Spectroscopic Studies of Hydrogen Bonding and Hydrophobicity”, *Science* (1994) **264** 826–828.
- [86] Q. Ong, N. Nianias, and F. Stellacci, “A review of molecular phase separation in binary self-assembled monolayers of thiols on gold surfaces”, *EPL (Europhysics Letters)* (2017) **119** 66001.
- [87] G. E. Poirier, “Characterization of Organosulfur Molecular Monolayers on Au(111) using Scanning Tunneling Microscopy.”, *Chem. Rev.* (1997) **97** 1117–1128.

REFERENCES

- [88] B. deBoer, A. Hadipour, M.M. Mandoc, T. vanWoudenberg, and P.W.M. Blom, “Tuning of metal work functions with self-assembled monolayers”, *Adv. Mater.* (2005) **17** 621–625.
- [89] B. Bhushan and H. Liu, “Nanotribological properties and mechanisms of alkylthiol and biphenyl thiol self-assembled monolayers studied by afm”, *Phys. Rev. B* (2001) **63** 245412.
- [90] L. Iversen, O. Younes-Metzler, K. L. Martinez, and D. Stamou, “Chemically specific laserinduced patterning of alkanethiol sams: Characterization by sem and afm”, *Langmuir* (2009) **25** 12819–12824.
- [91] P. Fenter, A. Eberhardt, K. S. Liang, and P. Eisenberger, “Epitaxy and chain-length dependent strain in self-assembled monolayers”, *J. Chem. Phys.* (1997) **106** 1600–1608.
- [92] P. Han, A. R. Kurland, A. N. Giordano, S. U. Nanayakkara, M. M. Blake, C. M. Pochas, and P. S. Weiss, “Heads and tails: Simultaneous exposed and buried interface imaging of monolayers”, *ACS Nano* (2009) **3** 3115–3121.
- [93] D. Anselmetti, A. Baratoff, H. J. Güntherodt, E. Delamarche, B. Michel, Ch Gerber, H. Kang, H. Wolf, and H. Ringsdorf, “Domain and molecular superlattice structure of dodecanethiol self-assembled on Au(111)”, *EPL (Europhysics Letters)* (1994) **27** 365–370.
- [94] D. L. Vanderhart, “Influence of molecular packing on solid-state ^{13}C chemical shifts: The n-alkanes”, *J. Magn. Reson.* (1981) **44** 117–125.
- [95] J.A. DeRose, T. Thundat, L.A. Nagahara, and S.M. Lindsay, “Gold grown epitaxially on mica: conditions for large area flat faces”, *Surf. Sci.* (1991) **256** 102 – 108.
- [96] D. Hobara, M. Ota, S. I. Imabayashi, K. Niki, and T. Kakiuchi, “Phase separation of binary self-assembled thiol monolayers composed of 1-hexadecanethiol and 3-mercaptopropionic acid on Au(111) studied by scanning tunneling microscopy and cyclic voltammetry”, *J. Electroanal. Chem.* (1998) **444** 113–119.
- [97] T. Kakiuchi, K. Sato, M. Iida, D. Hobara, S. I. Imabayashi, and K. Niki, “Phase separation of alkanethiol self-assembled monolayers during the replacement of adsorbed thiolates on Au(111) with thiols in solution”, *Langmuir* (2000) **16** 7238–7244.

REFERENCES

- [98] D. Hobara, S. I. Imabayashi, and T. Kakiuchi, “Preferential Adsorption of Horse Heart Cytochrome c on Nanometer-Scale Domains of a Phase-Separated Binary Self-Assembled Monolayer of 3-Mercaptopropionic Acid and 1-Hexadecanethiol on Au(111)”, *Nano Lett.* (2002) **2** 1021–1025.
- [99] G. E. Poirier, “Mechanism of Formation of Au Vacancy Islands in Alkanethiol Monolayers on Au(111)”, *Langmuir* (1997) **13** 2019–2026.
- [100] M. Matena, J. Björk, M. Wahl, T. L. Lee, J. Zegenhagen, L. H. Gade, T. A. Jung, M. Persson, and M. Stöhr, “On-surface synthesis of a two-dimensional porous coordination network: Unraveling adsorbate interactions”, *Phys. Rev. B* (2014) **90** 125408.
- [101] S. Kawai, A. S. Foster, T. Björkman, S. Nowakowska, J. Björk, F. F. Canova, L. H. Gade, T. A. Jung, and E. Meyer, “Van der Waals interactions and the limits of isolated atom models at interfaces”, *Nat. Commun.* (2016) **7** 11559.
- [102] M. Stöhr, M. Wahl, C. H. Galka, T. Riehm, T. A. Jung, and L. H. Gade, “Controlling molecular assembly in two dimensions: The concentration dependence of thermally induced 2D aggregation of molecules on a metal surface”, *Angew. Chem. Int. Ed.* (2005) **44** 7394–7398.
- [103] O. Voznyy and J. J. Dubowski, “c(4×2) Structures of alkanethiol monolayers on Au (111) compatible with the constraint of dense packing”, *Langmuir* (2009) **25** 7353–7358.
- [104] H. Grönbeck, H. Häkkinen, and R. L. Whetten, “Gold - Thiolate Complexes Form a Unique c(4×2) Structure on Au(111)”, *J. Phys. Chem. C* (2008) **112** 15940–15942.
- [105] N. Ishida, T. Inoue, M. Miyahara, and K. Higashitani, “Nano bubbles on a hydrophobic surface in water observed by tapping-mode atomic force microscopy”, *Langmuir* (2000) **16** 6377–6380.
- [106] S. M. Mendoza, I. Arfaoui, S. Zanarini, F. Paolucci, and P. Rudolf, “Improvements in the characterization of the crystalline structure of acid-terminated alkanethiol self-assembled monolayers on Au(111)”, *Langmuir* (2007) **23** 582–588.
- [107] E. Ito, K. Konno, J. Noh, K. Kanai, Y. Ouchi, K. Seki, and M. Hara, “Chain length dependence of adsorption structure of COOH-terminated alkanethiol SAMs on Au(111)”, *Appl. Surf. Sci.* (2005) **244** 584–587.

REFERENCES

- [108] W. C. Lin, S. H. Lee, M. Karakachian, B. Y. Yu, Y. Y. Chen, Y. C. Lin, C. H. Kuo, and J. J. Shyue, “Tuning the surface potential of gold substrates arbitrarily with self-assembled monolayers with mixed functional groups”, *Phys. Chem. Chem. Phys.* (2009) **11** 6199–6204.
- [109] Y. He, Y. Chang, J. C. Hower, J. Zheng, S. Chen, and S. Jiang, “Origin of repulsive force and structure/dynamics of interfacial water in OEG-protein interactions: a molecular simulation study.”, *Phys. Chem. Chem. Phys.* (2008) **10** 5539–5544.
- [110] W. Beckner, Y. He, and J. Pfendtner, “Chain Flexibility in Self-Assembled Monolayers Affects Protein Adsorption and Surface Hydration: A Molecular Dynamics Study”, *J. Phys. Chem. B* (2016) **120** 10423–10432.
- [111] P. Gilli, L. Pretto, V. Bertolasi, and G. Gilli, “Predicting Hydrogen-Bond strengths from Acid-Base molecular properties. the pKa slide rule: Toward the solution of a Long-Lasting problem”, *Acc. Chem. Res.* (2009) **42** 33–44.
- [112] R. Godawat, S. N. Jamadagni, and S. Garde, “Characterizing hydrophobicity of interfaces by using cavity formation, solute binding, and water correlations.”, *Proc. Natl. Acad. Sci. USA* (2009) **106** 15119–15124.
- [113] M. Maccarini, R. Steitz, M. Himmelhaus, J. Fick, S. Tatur, M. Wolff, M. Grunze, J. Janeček, and R. R. Netz, “Density depletion at solid-liquid interfaces: A neutron reflectivity study”, *Langmuir* (2007) **23** 598–608.
- [114] A. Labuda, K. Kobayashi, D. Kiracofe, K. Suzuki, P. H. Grütter, and H. Yamada, “Comparison of photothermal and piezoacoustic excitation methods for frequency and phase modulation atomic force microscopy in liquid environments”, *AIP Adv.* (2011) **1** 022136.
- [115] H. Peng, G. R. Birkett, and A. V. Nguyen, “Origin of interfacial nanoscopic gaseous domains and formation of dense gas layer at hydrophobic solidwater interface”, *Langmuir* (2013) **29** 15266–15274.
- [116] A. Kozbial, X. Gong, H. Liu, and L. Li, “Understanding the intrinsic water wettability of graphite”, *Langmuir* (2015) **31** 8429–8435.
- [117] Y. H. Lu, C. W. Yang, and I. S. Hwang, “Atomic force microscopy study of nitrogen molecule self-assembly at the HOPG-water interface”, *Appl. Surf. Sci.* (2014) **304** 56–64.

REFERENCES

- [118] P. Gallagher, Y. Li, K. Watanabe, T. Taniguchi, T. F. Heinz, and D. Goldhaber-Gordon, “Optical Imaging and Spectroscopic Characterization of Self-Assembled Environmental Adsorbates on Graphene”, *Nano Lett.* (2018) **18** 2603–2608.
- [119] D. S. Wastl, F. Speck, E. Wutscher, M. Ostler, T. Seyller, and F. J. Giessibl, “Observation of 4 nm pitch stripe domains formed by exposing graphene to ambient air”, *ACS Nano* (2013) **7** 10032–10037.
- [120] T. Hiasa and H. Onishi, “Competitive adsorption on graphite investigated using frequency-modulation atomic force microscopy: Interfacial liquid structure controlled by the competition of adsorbed species”, *Langmuir* (2013) **29** 5801–5805.
- [121] K. Suzuki, K. Kobayashi, N. Oyabu, K. Matsushige, and H. Yamada, “Molecular-scale investigations of structures and surface charge distribution of surfactant aggregates by three-dimensional force mapping”, *J. Chem. Phys.* (2014) **140** 054704.
- [122] M. L. Gee, P. M. McGuiggan, J. N. Israelachvili, and A. M. Homola, “Liquid to solidlike transitions of molecularly thin films under shear”, *J. Chem. Phys.* (1990) **93** 1895–1906.
- [123] K. Kobayashi, T. Horiuchi, H. Yamada, and K. Matsushige, “STM studies on nanoscopic structures and electric characteristics of alkanethiol and alkanedithiol self-assembled monolayers”, *Thin Solid Films* (1998) **331** 210–215.
- [124] D. Hobara, T. Sasaki, S. I. Imabayashi, and T. Kakiuchi, “Surface structure of binary self-assembled monolayers formed by electrochemical selective replacement of adsorbed thiols”, *Langmuir* (1999) **15** 5073–5078.
- [125] P. Stock, T. Utzig, and M. Valtiner, “Direct and quantitative AFM measurements of the concentration and temperature dependence of the hydrophobic force law at nanoscopic contacts”, *J. Colloid Interface Sci.* (2015) **446** 244–251.
- [126] M. Watkins and B. Reischl, “A simple approximation for forces exerted on an AFM tip in liquid”, *J. Chem. Phys.* (2013) **138** 154703.
- [127] K. I. Amano, K. Suzuki, T. Fukuma, O. Takahashi, and H. Onishi, “The relationship between local liquid density and force applied on a tip of atomic force microscope: A theoretical analysis for simple liquids”, *J. Chem. Phys.* (2013) **139** 224710.

REFERENCES

- [128] K. Umeda, K. Kobayashi, T. Minato, and H. Yamada, “Atomic-scale 3d local hydration structures influenced by water-restricting dimensions”, *Langmuir* (2018) **34** 9114–9121.
- [129] C. E. D. Chidsey and D. N. Loiacono, “Chemical Functionality in Self-Assembled Monolayers: Structural and Electrochemical Properties”, *Langmuir* (1990) **6** 682–691.
- [130] L. Strong and G. M. Whitesides, “Structures of Self-Assembled Monolayer Films of Organosulfur Compounds Adsorbed on Gold Single Crystals: Electron Diffraction Studies”, *Langmuir* (1988) **4** 546–558.
- [131] M. D. Porter, T. B. Bright, D. L. Aliara, and C. E. D. Chidsey, “Spontaneously Organized Molecular Assemblies. 4. Structural Characterization of n-Alkyl Thiol Monolayers on Gold by Optical Ellipsometry, Infrared Spectroscopy, and Electrochemistry”, *J. Am. Chem. Soc.* (1987) **109** 3559–3568.
- [132] R. G. Nuzzo, E. M. Korenic, and L. H. Dubois, “Studies of the temperature-dependent phase behavior of long chain nalkyl thiol monolayers on gold”, *J. Chem. Phys.* (1990) **93** 767–773.
- [133] N. Camillone, C. E. D. Chidsey, G. Liu, and G. Scoles, “Superlattice structure at the surface of a monolayer of octadecanethiol selfassembled on au(111)”, *J. Chem. Phys.* (1993) **98** 3503–3511.
- [134] E. Delamarche, B. Michel, A. B. Hans, and C. Gerber, “Golden interfaces: The surface of selfassembled monolayers”, *Adv. Mater.* (1996) **8** 719–729.
- [135] T. Fukuma, T. Ichii, K. Kobayashi, H. Yamada, and K. Matsushige, “Molecular-scale noncontact atomic force microscopy contrasts in topography and energy dissipation on $c(4\times 2)$ superlattice structures of alkanethiol self-assembled monolayers”, *J. Appl. Phys.* (2004) **95** 1222–1226.
- [136] G. E. Poirier and M. J. Tarlov, “The $c(4\times 2)$ Superlattice of n-Alkanethiol Monolayers Self-Assembled on Au(111)”, *Langmuir* (1994) **10** 2853–2856.
- [137] B. Lüssem, L. Müller-Meskamp, S. Karthäuser, and R. Waser, “A new phase of the $c(4\times 2)$ superstructure of alkanethiols grown by vapor phase deposition on gold”, *Langmuir* (2005) **21** 5256–5258.

REFERENCES

- [138] F. Li, L. Tang, W. Zhou, and Q. Guo, “Relationship between the $c(4\times 2)$ and the $(\sqrt{3}\times\sqrt{3})R30^\circ$ phases in alkanethiol self-assembled monolayers on Au(111)”, *Phys. Chem. Chem. Phys.* (2011) **13** 11958–11964.
- [139] A. Chaudhuri, T. J. Lerotholi, D. C. Jackson, D. P. Woodruff, and Robert G. Jones, “(233) rect. phase of alkylthiolate self-assembled monolayers on Au(111): A symmetry-constrained structural solution”, *Phys. Rev. B* (2009) **79** 195439.
- [140] P Fenter, A Eberhardt, and P Eisenberger, “Self-Assembly of n-Alkyl Thiols as Disulfides on Au(111)”, *Science* (1994) **266** 1216–1218.
- [141] X. Torrelles, C. Vericat, M. E. Vela, M. H. Fonticelli, M. A. Daza Millone, R. Felici, T.-L. Lee, J. Zegenhagen, G. Muñoz, J. A. Martín-Gago, and R. C. Salvarezza, “Two-Site Adsorption Model for the $(\sqrt{3}\times\sqrt{3})R30^\circ$ Dodecanethiolate Lattice on Au(111) Surfaces”, *J. Phys. Chem. B* (2006) **110** 5586–5594.
- [142] M. Yu, N. Bovet, C. J. Satterley, S. Bengió, K. R. J. Lovelock, P. K. Milligan, R. G. Jones, D. P. Woodruff, and V. Dhanak, “True nature of an archetypal self-assembly system: Mobile Au-thiolate species on Au(111)”, *Phys. Rev. Lett.* (2006) **97** 166102.
- [143] Q. Guo and F. Li, “Self-assembled alkanethiol monolayers on gold surfaces: resolving the complex structure at the interface by stm”, *Phys. Chem. Chem. Phys.* (2014) **16** 19074–19090.
- [144] L. A. Bumm, J. J. Arnold, L. F. Charles, T. D. Dunbar, D. L. Allara, and P. S. Weiss, “Directed self-assembly to create molecular terraces with molecularly sharp boundaries in organic monolayers”, *J. Am. Chem. Soc.* (1999) **121** 8017–8021.
- [145] I. Horcas, R. Fernández, J. M. Gómez-Rodríguez, J. Colchero, J. Gómez-Herrero, and A. M. Baro, “Wsxm: A software for scanning probe microscopy and a tool for nanotechnology”, *Rev. Sci. Instrum.* (2007) **78** 013705.
- [146] Y. F. Liu, Y. C. Yang, and Y. L. Lee, “Assembly behavior and monolayer characteristics of OH-terminated alkanethiol on Au(111): In situ scanning tunneling microscopy and electrochemical studies”, *Nanotechnology* (2008) **19** 065609.
- [147] Y.-F. Liu and Y.-L. Lee, “Adsorption characteristics of OH-terminated alkanethiol and arenethiol on Au(111) surfaces”, *Nanoscale* (2012) **4** 2093–2100.

REFERENCES

- [148] T. Hiasa, K. Kimura, and H. Onishi, “Hydration of hydrophilic thiolate monolayers visualized by atomic force microscopy”, *Phys. Chem. Chem. Phys.* (2012) **14** 8419–8424.
- [149] T. Hiasa and H. Onishi, “Mercaptohexanol assembled on gold: FM-AFM imaging in water”, *Colloids Surf. A* (2014) **441** 149 – 154.
- [150] G. E. Poirier, E. D. Pylant, and J. M. White, “Crystalline structures of pristine and hydrated mercaptohexanol selfassembled monolayers on au(111)”, *J. Chem. Phys.* (1996) **104** 7325–7328.
- [151] R. Yamada, H. Wano, and K. Uosaki, “Effect of temperature on structure of the self-assembled monolayer of decanethiol on Au(111) surface”, *Langmuir* (2000) **16** 5523–5525.
- [152] L. R. Houk, S. R. Challa, B. Grayson, P. Fanson, and A. K. Datye, “The definition of ”critical radius” for a collection of nanoparticles undergoing Ostwald ripening”, *Langmuir* (2009) **25** 11225–11227.
- [153] M. D. Abramoff, P. J. Magalhaes and S. J. Ram, “Image processing with ImageJ” , *Biophotonics Int.* (2004) **11** 36–42.
- [154] P. Carro, E. Pensa, C. Vericat, and R. C. Salvarezza, “Hydrocarbon chain length induces surface structure transitions in alkanethiolate-gold adatom self-assembled monolayers on Au(111)”, *J. Phys. Chem. C* (2013) **117** 2160–2165.
- [155] P. Carro, X. Torrelles, and R. C. Salvarezza, “A novel model for the ($\sqrt{3} \times \sqrt{3}$)-R30° alkanethiolate – Au(111) phase based on alkanethiolateAu adatom complexes”, *Phys. Chem. Chem. Phys.* (2014) **16** 19017–19023.
- [156] X. Torrelles, E. Pensa, E. Cortés, R. Salvarezza, P. Carro, C. Hernández Guerrero, C. Ocal, E. Barrena, and S. Ferrer, “Solving the Long-Standing Controversy of Long-Chain Alkanethiols Surface Structure on Au(111)”, *J. Phys. Chem. C* (2018) **122** 3893–3902.
- [157] X. Torrelles, E. Barrena, C. Munuera, J. Rius, S. Ferrer, and C. Ocal, “New insights in the c(4×2) reconstruction of hexadecanethiol on Au(111) revealed by grazing incidence X-ray diffraction”, *Langmuir* (2004) **20** 9396–9402.
- [158] O. Voznyy, J. J. Dubowski, J. T. Yates, and P. Maksymovych, “The role of gold adatoms and stereochemistry in self-assembly of methylthiolate on Au(111)”, *J. Am. Chem. Soc.* (2009) **131** 12989–12993.

REFERENCES

- [159] P. Maksymovych, D. C. Sorescu, and J. T. Yates, “Gold-atom-mediated bonding in self-assembled short-chain alkanethiolate species on the Au(111) surface”, *Phys. Rev. Lett.* (2006) **97** 146103.
- [160] C. Vericat, M. E. Vela, G. A. Benitez, J. A. Martin Gago, X. Torrelles, and R. C. Salvarezza, “Surface characterization of sulfur and alkanethiol self-assembled monolayers on Au(111)”, *J. Phys. Condens. Matter* (2006) **18** R867–R900.
- [161] T. Ichii, T. Fukuma, K. Kobayashi, H. Yamada, and K. Matsushige, “Surface potential measurements of phase-separated alkanethiol self-assembled monolayers by non-contact atomic force microscopy”, *Nanotechnology* (2004) **15** S30–S33.
- [162] J. Lü, E. Delamarche, L. Eng, R. Bennewitz, E. Meyer, and H. J. Güntherodt, “Kelvin probe force microscopy on surfaces: investigation of the surface potential of self-assembled monolayers on gold”, *Langmuir* (1999) **15** 8184–8188.
- [163] S. D. Evans, E. Urankar, A. Ulman, and N. Ferris, “Self-Assembled Monolayers of Alkanethiols Containing a Polar Aromatic Group: Effects of the Dipole Position on Molecular Packing, Orientation, and Surface Wetting Properties”, *J. Am. Chem. Soc.* (1991) **113** 4121–4131.
- [164] M. A. Rampi, O. J. A. Schueller, and G. M. Whitesides, “Alkanethiol self-assembled monolayers as the dielectric of capacitors with nanoscale thickness”, *Appl. Phys. Lett.* (1998) **72** 1781–1783.
- [165] F. Mugele and J. C. Baret, “Electrowetting: From basics to applications”, *J. Phys. Condens. Matter* (2005) **17** R705–R774.
- [166] D. Huh, A. H. Tkaczyk, J. H. Bahng, Y. Chang, H. H. Wei, J. B. Grotberg, C. J. Kim, K. Kurabayashi, and S. Takayama, “Reversible Switching of High-Speed Air-Liquid Two-Phase Flows Using Electrowetting-Assisted Flow-Pattern Change”, *J. Am. Chem. Soc.* (2003) **125** 14678–14679.
- [167] B. Berge and J. Peseux, “Variable focal lens controlled by an external voltage: An application of electrowetting”, *Eur. Phys. J. E* (2000) **3** 159–163.
- [168] R. A. Hayes and B. J. Feenstra, “Video-speed electronic paper based on electrowetting”, *Nature* (2003) **425** 383–385.
- [169] P. Lo Nostro and B. W. Ninham, “Hofmeister phenomena: an update on ion specif”, *Chem. Rev.* (2012) **112** 2286–322.

REFERENCES

- [170] N. Schwierz, D. Horinek, U. Sivan, and R. R. Netz, “Reversed Hofmeister series The rule rather than the exception”, *Curr. Opin. Colloid Interface Sci.* (2016) **23** 10–18.
- [171] A. Salis and B. W. Ninham, “Models and mechanisms of Hofmeister effects in electrolyte solutions, and colloid and protein systems revisited”, *Chem. Soc. Rev.* (2014) **43** 7358–7377.
- [172] A. N. Patel, M. G. Collignon, M. A. O’Connell, W. O. Y. Hung, K. McKelvey, J. V. MacPherson, and P. R. Unwin, “A new view of electrochemistry at highly oriented pyrolytic graphite”, *J. Am. Chem. Soc.* (2012) **134** 20117–20130.
- [173] Boris J. Albers, Todd C. Schwendemann, Mehmet Z. Baykara, Nicolas Pilet, Marcus Liebmann, Eric I. Altman, and Udo D. Schwarz, “Three-dimensional imaging of short-range chemical forces with picometre resolution”, *Nat. Nanotechnol.* (2009) **4** 307–310.
- [174] P. Avouris, Z. Chen, and V. Perebeinos, “Carbon-based electronics”, *Nat. Nanotechnol.* (2007) **2** 605–615.
- [175] R. Raccichini, A. Varzi, S. Passerini, and B. Scrosati, “The role of graphene for electrochemical energy storage”, *Nat. Mater.* (2015) **14** 271–279.
- [176] D. Berman, A. Erdemir, and A. V. Sumant, “Graphene: A new emerging lubricant”, *Mater. Today* (2014) **17** 31–42.
- [177] T. Utsunomiya, Y. Yokota, T. Enoki, and K. Fukui, “Potential-dependent hydration structures at aqueous solution/graphite interfaces by electrochemical frequency modulation atomic force microscopy”, *Chem. Commun.* (2014) **50** 15537–15540.
- [178] S Manne, P K Hansma, J Massie, V B Elings, and A A Gewirth, “Atomic-Resolution Electrochemistry with the AFM: Copper Deposition on Gold,”, *Science* (1991) **251** 183–186.
- [179] S. L. Yau, C. M. Vitus, and B. C. Schardt, “In Situ Scanning Tunneling Microscopy of Adsorbates on Electrode Surfaces: Images of the $(\sqrt{3} \times \sqrt{3})R30^\circ$ -Iodine Adlattice on Platinum(111)”, *J. Am. Chem. Soc.* (1990) **112** 3677–3679.
- [180] U. Zhumaev, A. V. Rudnev, J. F. Li, A. Kuzume, T. H. Vu, and T. Wandlowski, “Electro-oxidation of Au(111) in contact with aqueous electrolytes: New insight from in situ vibration spectroscopy”, *Electrochim. Acta* (2013) **112** 853–863.

REFERENCES

- [181] T. Utsunomiya, S. Tatsumi, Y. Yokota, and K. Fukui, “Potential-dependent structures investigated at the perchloric acid solution/iodine modified Au(111) interface by electrochemical frequency-modulation atomic force microscopy”, *Phys. Chem. Chem. Phys.* (2015) **17** 12616–12622.
- [182] M. Negami, T. Ichii, K. Murase, and H. Sugimura, “Visualization of Ionic-Liquid/Solid Interfaces by Frequency Modulation Atomic Force Microscopy”, *ECS Transactions* (2012) **50** 349–355.
- [183] K. D. Collins, “Ions from the Hofmeister series and osmolytes: Effects on proteins in solution and in the crystallization process”, *Methods* (2004) **34** 300–311.
- [184] R. Gréget, G. L. Nealon, B. Vilen, P. Turek, C. Mény, F. Ott, A. Derory, E. Voirin, E. Rivière, A. Rogalev, F. Wilhelm, L. Joly, W. Knafo, G. Ballon, E. Terazzi, J. P. Kappler, B. Donnio, and J. L. Gallani, “Magnetic properties of gold nanoparticles: A room-temperature quantum effect”, *ChemPhysChem* (2012) **13** 3092–3097.
- [185] R. A. Sperling, P. R. Gil, F. Zhang, M. Zanell, and W. J. Park, “Biological applications of gold nanoparticles”, *Chem. Soc. Rev.* (2008) **37** 1909–1930.
- [186] S. Kumar, N. Harrison, R. Richards-Kortum and K. Sokolov, “Plasmonic nanosensors for imaging intracellular biomarkers in live cells”, *Nano Lett.* (2007) **7** 1338–1343.
- [187] B. Duncan, C. Kim, and V. M. Rotello, “Gold nanoparticle platforms as drug and biomacromolecule delivery systems”, *J. Control. Release* (2010) **148** 122–127.
- [188] M. Haruta, “When gold is not noble: Catalysis by nanoparticles”, *Chem. Rec.* (2003) **3** 75–87.
- [189] T. Torimoto, K. Okazaki, T. Kiyama, K. Hirahara, N. Tanaka and S. Kuwabata, “Sputter deposition onto ionic liquids: Simple and clean synthesis of highly dispersed ultrafine metal nanoparticles”, *Appl. Phys. Lett.* (2006) **89** 243117.
- [190] M. Brust, M. Walker, D. Bethell, D. J. Schiffrin and R. Whyman, “Synthesis of thiol-derivatised gold nanoparticles in a two-phase liquid-liquid system”, *J. Chem. Soc., Chem. Commun.* (1994) **0** 801–802.
- [191] S. C. Hamm, S. Basuray, S. Mukherjee, S. Sengupta, J. C. Mathai, G. A. Baker and S. Gangopadhyay, “Ionic conductivity enhancement of sputtered gold nanoparticle-in-ionic liquid electrolytes”, *J. Mater. Chem. A* (2014) **2** 792–803.

REFERENCES

- [192] M. S. Sibbald, G. Chumanov, and T. M. Cotton, “Reduction of Cytochrome c by Halide-Modified , Laser-Ablated Silver Colloids”, *J. Phys. Chem. C* (1996) **100** 4672–4678.
- [193] K. Richter, A. Birkner and A.-V. Mudring, “Stability and growth behavior of transition metal nanoparticles in ionic liquids prepared by thermal evaporation: how stable are they really?”, *Phys. Chem. Chem. Phys.* (2011) **13** 7136–7141.
- [194] H. Wender, P. Migowski, A. F. Feil, L. F. de Oliveira, M. H. G. Prechtel, R. Leal, G. Machado, S. R. Teixeira, and J. Dupont, “On the formation of anisotropic gold nanoparticles by sputtering onto a nitrile functionalised ionic liquid.”, *Phys. Chem. Chem. Phys.* (2011) **13** 13552–13557.
- [195] E. Vanecht, K. Binnemans, J. W. Seo, L. Stappers and J. Fransaer, “Growth of sputter-deposited gold nanoparticles in ionic liquids”, *Phys. Chem. Chem. Phys.* (2011) **13** 13565–13571.
- [196] Y. Hatakeyama, K. Onishi, and K. Nishikawa, “Effects of sputtering conditions on formation of gold nanoparticles in sputter deposition technique”, *RSC Adv.* (2011) **1** 1815–1821.
- [197] D. Sugioka, T. Kameyama, S. Kuwabata, and T. Torimoto, “Single-step preparation of two-dimensionally organized gold particles via ionic liquid/metal sputter deposition”, *Phys. Chem. Chem. Phys.* (2015) **17** 13150–13159.
- [198] K. Richter, A. Birkner and A.-V. Mudring, “Stabilizer-Free Metal Nanoparticles and Metal-Metal Oxide Nanocomposites with Long-Term Stability Prepared by Physical Vapor Deposition into Ionic Liquids”, *Angew. Chem. Int. Ed.* (2010) **49** 2431–2435.
- [199] V. S. Raghuwanshi, M. Ochmann, A. Hoell, F. Polzer and K. Rademann, “Deep eutectic solvents for the self-assembly of gold nanoparticles: A saxs, uv-vis, and tem investigation”, *Langmuir* (2014) **30** 6038–6046.
- [200] T. Ienaga, Y. Nakahara, and K. Kimura, “Synthesis and Characterization of Silver Nanoparticles by Vacuum Evaporation on Running Hydrocarbon Solution Containing Nonionic Surfactant in Cylindrical Glass Chamber”, *Chem. Lett.* (2014) **43** 1893–1895.

REFERENCES

- [201] J. Neddersen, G. Chumanov, and T. M. Cotton, “Laser ablation of metals: A new method for preparing SERS active colloids”, *Appl. Spectrosc.* (1993) **47** 1959–1964.
- [202] H. Wender, L. F. de Oliveira, A. F. Feil, E. Lissner, P. Migowski, M. R. Meneghetti, S. R. Teixeira and J. Dupont, “Synthesis of gold nanoparticles in a biocompatible fluid from sputtering deposition onto castor oil”, *Chem. Commun.* (2010) **46** 7019–7021.
- [203] H. Wender, R. V. Goncalves, A. F. Feil, P. Migowski, F. S. Poletto, A. R. Pohlmann, J. Dupont and S. R. Teixeira, “Sputtering onto liquids: From thin films to nanoparticles”, *J. Phys. Chem. C* (2011) **115** 16362–16367.
- [204] Y. Hatakeyama, T. Morita, S. Takahashi, K. Onishi and K. Nishikawa, “Synthesis of gold nanoparticles in liquid polyethylene glycol by sputter deposition and temperature effects on their size and shape”, *J. Phys. Chem. C* (2011) **115** 3279–3285.
- [205] S. Suzuki, T. Suzuki, Y. Tomita, M. Hirano, K. Okazaki, S. Kuwabata, and T. Torimoto, “Compositional control of AuPt nanoparticles synthesized in ionic liquids by the sputter deposition technique”, *CrystEngComm* (2012) **14** 4922–4926.
- [206] T. Suzuki, K. I. Okazaki, S. Suzuki, T. Shibayama, S. Kuwabata, and T. Torimoto, “Nanosize-controlled syntheses of indium metal particles and hollow indium oxide particles via the sputter deposition technique in ionic liquids”, *Chem. Mater.* (2010) **22** 5209–5215.
- [207] E. F. Borra, O. Seddiki, R. Angel, D. Eisenstein, P. Hickson, K. R. Seddon, and S. P. Worden, “Deposition of metal films on an ionic liquid as a basis for a lunar telescope”, *Nature* (2007) **447** 979–981.
- [208] E. C. Da Silva, M. G. A. Da Silva, S. M. P. Meneghetti, G. Machado, M. A. R. C. Alencar, J. M. Hickmann, and M. R. Meneghetti, “Synthesis of colloids based on gold nanoparticles dispersed in castor oil”, *J. Nanopart. Res.* (2008) **10** 201–208.
- [209] N. Wu, L. Fu, M. Su, M. Aslam, K. C. Wong, and V. P. Dravid, “Interaction of Fatty Acid Monolayers with Cobalt Nanoparticles”, *Nano Lett.* (2004) **4** 383–386.

REFERENCES

- [210] S. Gyergyek, D. Makovec, and M. Drofenik, “Colloidal stability of oleic- and ricinoleic-acid-coated magnetic nanoparticles in organic solvents”, *J. Colloid Interface Sci.* (2011) **354** 498–505.
- [211] Y. Hatakeyama, M. Okamoto T. Torimoto, S. Kuwabata and K. Nishikawa, “Small-Angle X-ray Scattering Study of Au Nanoparticles Dispersed in the Ionic Liquids 1-Alkyl-3-methylimidazolium Tetrafluoroborate”, *J. Phys. Chem. C* (2009) **113** 3917–3922.
- [212] A. P. Hammersley, S. O. Svensson, M. Hanfland, A. N. Fitch and D. Haüsermann, “Two-dimensional detector software: From real detector to idealised image or two-theta scan”, *High Pressure Res.* (1996) **14** 235–248.
- [213] E. Vanecht, K. Binnemans, S. Patskovsky, M. Meunier, J. W. Seo, L. Stappers and J. Fransaer, “Stability of sputter-deposited gold nanoparticles in imidazolium ionic liquids”, *Phys. Chem. Chem. Phys.* (2012) **14** 5662–5671.
- [214] M. Hirano, K. Enokida, K. Okazaki, S. Kuwabata, H. Yoshida and T. Torimoto, “Composition-dependent electrocatalytic activity of AuPd alloy nanoparticles prepared via simultaneous sputter deposition into an ionic liquid”, *Phys. Chem. Chem. Phys.* (2013) **15** 7286–7294.
- [215] L. K. Ono and B. R. Cuenya, “Formation and thermal stability of au₂o₃ on gold nanoparticles: Size and support effects”, *J. Phys. Chem. C* (2008) **112** 4676–4686.
- [216] Y. Joseph, I. Besnard, M. Rosenberger, B. Guse, H.-G. Nothofer, J. M. Wesels, U. Wild, A. Knop-Gericke, D. Su, R. Schlögl, A. Yasuda and T. Vossmeier, “Self-assembled gold nanoparticle/alkanedithiol films: Preparation, electron microscopy, xps-analysis, charge transport, and vapor-sensing properties”, *J. Phys. Chem. B* (2003) **107** 7406–7413.
- [217] J. Singh and J. E. Whitten, “Adsorption of 3-mercaptopropyltrimethoxysilane on silicon oxide surfaces and adsorbate interaction with thermally deposited gold”, *J. Phys. Chem. C* (2008) **112** 19088–19096.
- [218] L. Junyan, H. Ling, L. Weidong and L. Hongjie, “Synthesis and analysis of properties of a new core-shell silicon-containing fluoroacrylate latex”, *Polym. Int.* (2009) **58** 1283–1290.

REFERENCES

- [219] S.-Y. Lee and M. T. Harris, “Surface modification of magnetic nanoparticles capped by oleic acids: Characterization and colloidal stability in polar solvents”, *J. Colloid Interface Sci.* (2006) **293** 401–408.
- [220] D. C. Lim, I. Lopez-Salido, R. Dietsche, M. Bubeck and Y. D. Kim, “Electronic and chemical properties of supported Au nanoparticles”, *Chem. Phys.* (2006) **330** 441–448.
- [221] T. Laaksonen, P. Ahonen, C. Johans and K. Kontturi, “Stability and electrostatics of mercaptoundecanoic acid-capped gold nanoparticles with varying counterion size”, *ChemPhysChem* (2006) **7** 2143–2149.
- [222] B. Hu, X. Cao, and P. Zhang, “Dual control of interparticle forces in assembly of gold nanoparticles”, *ChemPlusChem* (2013) **78** 506–514.
- [223] M. D. Scanlon, P. Peljo, M. A. Mendez, E. Smirnov and H. H. Girault, “Charging and discharging at the nanoscale: Fermi level equilibration of metallic nanoparticles”, *Chem. Sci.* (2015) **6** 2705–2720.
- [224] C. Novo, A. M. Funston and P. Mulvaney, “Direct observation of chemical reactions on single gold nanocrystals using surface plasmon spectroscopy”, *Nat. Nanotechnol.* (2008) **3** 598–602.
- [225] T. Ung, M. Giersig, D. Dunstan and P. Mulvaney, “Spectroelectrochemistry of colloidal silver”, *Langmuir* (1997) **13** 1773–1782.

List of Research Achievements

Publications

1. Akito Fujita, Yusuke Matsumoto, Mitsuaki Takeuchi, Hiromichi Ryuto and G. H. Takaoka, "Growth behavior of gold nanoparticles synthesized in unsaturated fatty acids by vacuum evaporation methods" *Phys. Chem. Chem. Phys.*, **18** (2016) 5464.
2. Akito Fujita, Kei Kobayashi and Hirofumi Yamada, "Investigation of Local Hydration Structures of Alkanethiol Self-Assembled Monolayers with Different Molecular Structures by FM-AFM" *Langmuir* **34** (2018) 15189.
3. Akito Fujita, Kei Kobayashi and Hirofumi Yamada, "Investigation of the Local Hydration Structure on Hydrophobic Self-Assembled Monolayers by FM-AFM" Submitted.
4. Akito Fujita, Kei Kobayashi and Hirofumi Yamada, "Development of an Electrochemical AFM cell and Application on Force Mapping Techniques" To be submitted.

Presentations

1. Akito Fujita, Kei Kobayashi and Hirofumi Yamada, Molecular-scale investigations of hydration structures on self-assembled monolayers in aqueous solutions KJF International Conference on Organic Materials for electronics and photonics, PS-166, Fukuoka Japan, 2016/9 [Poster] **Best Student Poster Award**

2. Akito Fujita, Kei Kobayashi and Hirofumi Yamada, Molecular-Scale Investigations of Hydration Structures of Alkanethiol Self-Assembled Monolayers by FM-AFM, 29th International Microprocesses and Nanotechnology Conference, 10P-7-69, Kyoto Japan, 2016/11 [Poster]
3. Akito Fujita, Kei Kobayashi and Hirofumi Yamada, Molecular-Scale Investigations of Hydration Structures of Alkanethiol Self-Assembled Monolayers of Different Functional Groups by FM-AFM, the 19th International Scanning Probe Microscopy Conference, ThD-5, Kyoto Japan, 2017/5 [Oral]
4. Akito Fujita, Kei Kobayashi and Hirofumi Yamada, Investigation of Hydration Structures of Phase Separated Alkanethiol Self-Assembled Monolayers by FM-AFM, 20th International Conference on Non-Contact Atomic Force Microscopy, Suzhou, China 2017/9 [Oral]
5. Akito Fujita, Kei Kobayashi and Hirofumi Yamada, Molecular-Scale Investigations of Local Hydration Structures of Alkanethiol Self-Assembled Monolayers with Different Molecular Structures, 21st International Conference on Non-Contact Atomic Force Microscopy, Porvoo, Finland 2018/9 [Poster]

Acknowledgements

The author would like to express his gratitude to Professor Hirofumi Yamada, Department of Electronic Science and Engineering, Kyoto University for his continuous encouragement, patient guidance and valuable suggestions to accomplish this study.

The author would like to acknowledge Professor Shizuo Fujita, Photonics and Electronic Science and Engineering Center, and Hiroyuki Sugimura, Department of Materials Science and Engineering for their valuable comments and suggestions on this study.

The author would like to appreciate Associate Professor Kei Kobayashi, Department of Electronic Science and Engineering for fruitful discussions, technical support and thorough guidance throughout this study.

The author would like to show sincere thanks to Assistant Professor Toru Utsunomiya, Department of Materials Science and Engineering for advices on SAM fabrication and electrochemical measurements.

The author would like to appreciate Dr. Yoshiki Hirata, National Institute of Advanced Industrial Science and Technology, for discussions on electrochemical measurements and practical support on the development of the EC-AFM cell.

The author would like to show deep thanks to Researcher Dr. Hiroaki Kominami for technical and practical support on FM-AFM measurements. The author also thanks for the encouragement during the authors Ph.D. course.

The author would like to appreciate Assistant Professor Yuki Araki for discussions and advice on surface science and hydration structure measurements.

The author would like to show special thanks to Researcher Dr. Kuniko Kimura for fruitful discussions.

The author would like to appreciate Dr. G. H. Takaoka, Dr. Mitsuaki Takeuchi and Mr. Yusuke Matsumoto for guidance and practical support and fruitful discussions for the authors master course study.

The author would like to show sincere thanks to Ph.D. course student Satoshi Asada and Takeshi Nogi for their encouragement and friendship throughout the authors Ph.D. course.

The author would like to appreciate the members of the laboratory and special thanks go to Mr. Yuki Yamamoto, Mr. Kiyotaka Fukuzuka, Mr. Kouichi Innami, Ms. Kazuna Sugimoto, Mr. Teruyuki Tanaka, Mr. Tsutau Yokocho, Mr. Masahiro Takeshita, Mr. Hiroshi Tono, Mr. Naoto Fukazawa, Mr. Shogo Maeda, Mr. Chuyang Lyu, Mr. Taiyou Ono, Mr. Shouhei Kanazawa, Mr. Shougo Terada, Mr. Tomoyuki Yoshimura, Mr. Masayuki Miyamoto, Mr. Takahiro Yamashita, Mr. Shyunta Nosaka, Mr. Takahiro Hamda and Mr. Zipeng Cui. The author would also like to appreciate Mrs. Tomoko Hayashida for assistance on the authors daily work.

Finally, the author would like to express special thanks to his family for their continuous encouragement and support in accomplishing this work.